

# Effects of microstructure modification induced by laser interference patterning of thin films

**Dissertation**

zur Erlangung des Grades  
des Doktors der Ingenieurwissenschaften  
der Naturwissenschaftlich-Technischen Fakultät III  
Chemie, Pharmazie, Bio- und Werkstoffwissenschaften  
der Universität des Saarlandes.



**UNIVERSITÄT  
DES  
SAARLANDES**

von

RODOLPHE JULES ANDRÉ CATRIN

Saarbrücken

2012

Tag des Kolloquiums: 17.02.2012

Dekan: Prof. Dr. Wilhelm F. Maier, Universität des Saarlandes

Berichterstatter: Prof. Dr.-Ing. Frank Mücklich, Universität des Saarlandes

Prof. Dr. Ralf Busch, Universität des Saarlandes

Vorsitzende: Prof. Dr.-Ing. Markus Stommel, Universität des Saarlandes

Akad. Mitarbeiter: Dr.-Ing. Afrooz Barnoush, Universität des Saarlandes





À Nancy, l'amour de ma vie.

*"A laser is a solution seeking a problem"*

Theodore H. Maiman



# Acknowledgments

I would like to take this opportunity to sincerely acknowledge the help, advice and support of the following individuals and institutions. Before, I would like to thank **God** for the blessings and grace He has given me throughout my life, especially during this work. I would like to offer my gratitude to **Professor Frank Mücklich**, not only for the scientific supervision of my work, but for having given me the chance to develop my interest for high-level research, for having involved me in several international activities within the Amase and EEIGM programmes, but more importantly for having forged in me his diplomatic, relational and managing talents. For accepting the revision of this work, I would like to thank **Professor Ralf Busch**. Also, **Dr. David Horwat**, **Dr. Thomas Gries** and colleagues from the Institut Jean Lamour in Nancy (France), to whom I am very grateful for the friendly collaboration and the critical discussions and expertise within the work we accomplished together. Thanks also to all my colleagues from the Chair of Functional Materials since my arrival in Saarland in 2005, specially **Andrés Lasagni**, **Flavio Soldera**, **Nicolas Jeanvoine** and **Carsten Gachot** for their pertinent advice, discussions and all the great moments we had together. I would additionally thank **Nicolas Souza** for the english correction of this work and the illustrations provided in sections 2.3.2 and 3.2. My thank goes to the **Deutsche Forschungsgemeinschaft** and **Deutscher Akademischer Austausch Dienst** as well for the funding during my doctoral thesis. Last but not least I would like to heartily thank my **family** who gave me support during my whole academic formation and most importantly to my **precious wife** for her daily encouragement and unconditional love.





# Table of contents

<b>Acknowledgments</b>	<b>iii</b>
<b>Abstract</b>	<b>ix</b>
<b>Zusammenfassung</b>	<b>xi</b>
<b>Symbols and acronyms</b>	<b>xiii</b>
<b>1 Introduction</b>	<b>1</b>
1.1 State of the art . . . . .	1
1.2 Motivation . . . . .	4
<b>2 Using laser light for surface engineering</b>	<b>9</b>
2.1 Laser principle . . . . .	10
2.1.1 Amplification by stimulated emission of radiation . . .	10
2.1.2 Laser pumping and optical cavity . . . . .	12
2.2 Laser-matter interaction . . . . .	13
2.2.1 Wave propagation . . . . .	14
2.2.2 Energy absorption by metals . . . . .	15
2.2.3 Laser-induced crystallization . . . . .	17
2.3 Laser interference patterning . . . . .	21
2.3.1 Beam path . . . . .	21
2.3.2 Interference principle of laser light . . . . .	21
<b>3 Experimental approach</b>	<b>25</b>
3.1 Film preparation . . . . .	26

3.1.1	Electron beam evaporation . . . . .	26
3.1.2	Magnetron sputtering . . . . .	26
3.1.3	Chemical etching . . . . .	28
3.2	Laser interference arrangement . . . . .	28
3.3	Topographic and microstructural characterization . . . . .	31
3.3.1	White light interferometry . . . . .	31
3.3.2	Focused ion beam: dual beam workstation . . . . .	32
3.3.3	X-ray diffraction . . . . .	32
3.3.4	Transmission electron microscopy . . . . .	32
3.3.5	Electron backscattered diffraction . . . . .	32
3.4	Evaluation of material properties . . . . .	33
3.4.1	Hardness . . . . .	33
3.4.2	Electrical resistivity . . . . .	33
3.4.3	Friction coefficient . . . . .	34
<b>4</b>	<b>Local modifications of the morphology and the microstructure</b>	<b>35</b>
4.1	Introduction . . . . .	36
4.2	Results and discussion . . . . .	37
4.2.1	Microstructural design of advanced architectures . . . . .	37
4.2.2	Long-range ordered architectures of grain sizes and orientations . . . . .	44
4.2.3	Mechanical composite effect . . . . .	47
4.3	Summary . . . . .	49
<b>5</b>	<b>Selective wet chemical etching of laser interference patterned films</b>	<b>51</b>
5.1	Introduction . . . . .	52
5.2	Results and discussion . . . . .	52
5.2.1	As-irradiated morphologies before etching . . . . .	53
5.2.2	Effect of chemical etching . . . . .	55
5.2.3	FIB cross section in Ti/Pt . . . . .	56
5.2.4	Effect of relaxation before etching . . . . .	58

5.3	Summary . . . . .	59
<b>6</b>	<b>Laser-assisted chemical decomposition for electrical conductivity enhancement</b>	<b>61</b>
6.1	Introduction . . . . .	62
6.2	Results and discussion . . . . .	63
6.2.1	Thermodynamics of the Pd-Pt-O system . . . . .	63
6.2.2	Morphological and topographical evolutions . . . . .	64
6.2.3	Microstructural analysis . . . . .	66
6.2.4	Chemical composition analysis . . . . .	71
6.2.5	Evolution of the electrical resistivity . . . . .	72
6.3	Summary . . . . .	74
<b>7</b>	<b>Segregation and growth of nanoparticles for the reduction of the friction coefficient</b>	<b>77</b>
7.1	Introduction . . . . .	78
7.2	Results and discussion . . . . .	79
7.2.1	Thermodynamics of the Au-YSZ system . . . . .	79
7.2.2	Segregation and grain-growth of Au nanoparticles . . . . .	80
7.2.3	Dry lubrication effect . . . . .	82
7.3	Summary . . . . .	86
<b>8</b>	<b>Conclusions and outlook</b>	<b>87</b>
	<b>References</b>	<b>91</b>
	<b>List of figures</b>	<b>A</b>
	<b>List of tables</b>	<b>C</b>
	<b>Curriculum Vitae</b>	<b>E</b>



# Abstract

Manipulating a material's microstructure to obtain the desired property at the desired place is one of the most important challenges in Materials Science. Since physical and chemical properties of metals are strongly correlated to their microstructure, its precise tailoring is of the highest interest. Laser Interference Patterning has been developed to locally modify the microstructure as well as the mechanical, electrical, optical and tribological properties of materials with a periodic distribution. This technique is exploited here in order to study:

- i)** the design of advanced architectures via local melting and resolidification processes,
- ii)** the morphological, microstructural and thermal evolution of the obtained long-range ordered architectures,
- iii)** the enhancement of the film conductivity and the friction coefficient for technical applications.

The investigations were carried out on two relevant thin film systems: pure metallic films and thin films of nitride and oxide matrices with embedded metallic particles. Microstructural influences of the irradiation method within the fabricated periodic arrays were systematically investigated. Focus was kept on localized microstructure relocation, chemical decomposition or segregation of nanoparticles. Additionally, the physical (hardness, electrical resistivity, friction coefficient) and chemical (etching capacity) properties of the modified systems were thoroughly evaluated and compared with unstructured systems.



# Zusammenfassung

Physikalische und chemische Eigenschaften von Werkstoffen hängen stark von deren Mikrostruktur ab. Eine kontrollierte Veränderung des Gefügezustands ist daher bei der Entwicklung moderner Materialien von höchstem Interesse. Eine der größten Herausforderungen der Materialwissenschaft ist jedoch die Mikrostruktur von Materialien so zu manipulieren, dass man die richtige Eigenschaft an der richtigen Stelle erhält. Laser-Interferenz-Metallurgie wurde daher entwickelt, um die Mikrostruktur und daraus folgend auch die mechanischen, elektrischen, optischen und tribologischen Eigenschaften von Materialien in periodischen Abständen gezielt zu modifizieren. In dieser Arbeit wird diese Technik verwendet, um Folgendes zu untersuchen:

- i)** das Design von verbesserten Strukturen durch lokales Aufschmelzen und Wiederverstarren,
- ii)** die Morphologie, Mikrostruktur und thermische Entwicklung von den auf diese Weise hergestellten, ferngeordneten Strukturen,
- iii)** die Verbesserung der Leitfähigkeit und des Reibungskoeffizienten von Dünnschichten, um deren technische Anwendbarkeit zu verbessern.

Die Untersuchungen wurden an zwei relevanten Dünnschicht-Systemen durchgeführt: an Dünnschichten aus reinem Metall, sowie an Dünnschichten auf Nitrid- und Oxid-Basis, in welche Metallpartikel eingelagert sind. Die Einflüsse der Laser-Bestrahlung auf die Mikrostruktur in den periodisch strukturierten Oberflächen wurden systematisch untersucht. Dabei wurde Augenmerk auf die lokale mikrostrukturelle Neuverteilung, die chemische Zersetzung und die Segregation von Nanopartikeln gelegt. Zusätzlich wurden die physikalischen (Härte, elektrische Leitfähigkeit, Reibkoeffizient) und chemischen (Ätzbarkeit) Eigenschaften von den modifizierten Systemen genau untersucht und mit denen der unstrukturierten Systemen verglichen.





# Symbols and acronyms

## Symbols

$\alpha$	Absorption coefficient
$\alpha_i$	Angle of the i-beam respected to the interference plane (x,z)
$a^2$	Patterned area
$A_{abs}$	Coefficient of absorption
$\beta_i$	Angle of the i-beam respected to the interference plane (x,y)
$c$	Light celerity
$\Delta G_f$	Gibbs energy of formation
$E$	Pulse energy or Young modulus
<b>E</b>	Electric field
$E_1$	Energy from level 1
$E_{i0}$	Amplitude of the electric field of each i beam
$\epsilon_0$	Dielectric constant in vacuum
$E_p$	Quantum of energy
$F$	Laser fluence
$G$	Gibbs energy
$H$	Hardness
$h$	Planck's constant
$I$	Intensity distribution or Applied current

$I_0$	Intensity of an electromagnetic radiation
$I(z)$	Variation of transmitted energy in z direction
$k$	Wave number
$\lambda$	Wavelength of the propagating wave
$\mu$	Friction coefficient
$n_1$	Population density of atoms in the ground state
$n_2$	Population density of atoms in the excited level
$\nu$	Radiation frequency
$n$	Refractive index
$n^*$	Complex index
$\omega$	Angular frequency
$\omega_c$	Collision frequency
$\omega_p$	Plasma frequency
$P$	Structure period
$R$	Ratio of reflected-to-incident irradiance
$\rho$	Film resistivity
$R_{ku}$	Kurtosis
$R_q$	Root-mean-square (rms)
$R_{sk}$	Skewness
$R_{re}$	Coefficient of reflexion
$\sigma_0$	DC conductivity
$t$	Time
$\tau_c$	Time between two collisions
$\theta$	Angle between laser beams
$T_{tr}$	Coefficient of transmission
$V$	Voltage

- $Y_i$  Heights of the profile  
 $z$  Direction of wave propagation

## Acronyms

- AMLCD** Active Matrix Liquid Crystal Display  
**CVD** Chemical Vapour Deposition  
**DC** Direct Current  
**EBSD** Electron Backscattered Diffraction  
**EDS** Energy Dispersive Spectroscopy  
**FIB** Focused Ion Beam  
**HeNe** Helium Neon (laser)  
**ICDD** International Centre for Diffraction Data  
**IPF** Inverse Pole Figure map  
**IR** Infrared  
**LASER** Light Amplification by Stimulated Emission of Radiation  
**LC** Laser Crystallization  
**LED** Light Emitting Diode  
**LIC** Laser Interference Crystallization  
**LIMET** Laser Interference Metallurgy  
**LIP** Laser Interference Patterning  
**MASER** Microwave Amplification by Stimulated Emission of Radiation  
**MEMS** MicroElectroMechanical Systems  
**Nd:YAG** Neodymium-doped Yttrium Aluminium Garnet (laser)  
**PF** Pole Figure map  
**SAED** Selected Area Electron Diffraction  
**SEM** Scanning Electron Microscope

<b>SLG</b>	Super Lateral Growth
<b>STEM</b>	Scanning Transmission Electron Microscope
<b>TEM</b>	Transmission Electron Microscope
<b>TFT</b>	Thin Film Transistor
<b>UV</b>	Ultraviolet
<b>WLI</b>	White Light Interferometry
<b>XRD</b>	X-ray Diffraction
<b>YSZ</b>	Yttria Stabilized Zirconia

# Chapter 1

## Introduction

### 1.1 State of the art

The manipulation of metal film microstructures and properties to obtain the desired property at the desired location is one of the most important challenges in Materials Science and Engineering. Since the microstructure's size parameters exert a strong influence on material's properties [1], the control over microstructural modifications is a technical topic of major interest.

Pulsed laser irradiation of thin films has been widely used in the semiconductor and solar cell industries to improve device effectivity in advanced applications such as high-performance polycrystalline silicon (poly-Si) thin film transistors (TFT) for high-definition active matrix liquid crystal displays (AMLCD) [2]. This clean particulate-free noncontact method was developed to avoid the difficulties of conventional heat treatment via rapid melting and solidification [3]. A precise control of the growth direction, the grain-size and grain location is desired [4, 5]. Several methods have been developed to achieve this goal, *e.g.* by using spatially selective melting and lateral temperature modulation [6–9] or by applying the double laser recrystallization technique, which leads to ultra-large direction- and location-controlled poly-Si grain growth [5]. Conventional pulsed laser crystallization (LC) of amorphous Si (a-Si) was designed as a cheap and fast procedure to melt the amorphous film throughout its entire thickness and yields small-grained poly-

Si. However, the spontaneous nucleation that occurs randomly in the layer is difficult to control [10] and limits the final grain size. To overcome this difficulty, a crystallization regime, known as Super Lateral Growth (SLG, see section 2.2.3), was shown to obtain grains considerably larger than the a-Si film thickness [11]. However, being extremely sensitive to laser parameters or substrate preparation, this crystallization regime leads to a large grain size distribution and thus limits the device's uniformity [12].

As the control of grain sizes and boundary locations requires a complete melting of the film in selected areas, a spatially selective melting can be obtained by inducing a non-uniform in-plane temperature distribution during irradiation [8]. The production of a localized temperature gradient has been proposed *e.g.* through the use of masks to shape a laser beam [13] or the use of antireflective coatings that allow a selective control of the laser absorption [14]. Even though these techniques have a wider processing window than that provided by the SLG regime, their technical realizations is far from trivial and they involve multiple steps. A further development of the LC technique was therefore proposed: Laser Interference Crystallization (LIC) [8, 15–17]. LIC principally combines LC with holographic techniques [18] in order to obtain a substantial lateral growth (large crystallites) and oriented grain boundaries. Two coherent laser beams are thus brought to interfere on the sample surface (originally on a-Si films), which leads to a spatial modulation of the laser intensity and a further periodical film melting over its entire thickness [8].

Even though the principle of rapid lateral solidification was originally developed for the crystallization of Si thin films on  $SiO_2$  substrates [5, 6, 19, 20], it has recently been applied to the microstructure modification of thin metallic films [3, 21, 22]. The advantages of the LIC technique are multiple. It allows both a rapid melting and a rapid conduction of heat into the substrate, which results in quenching and supercooling of the molten pool [3]. Laser Interference Metallurgy (LIMET) was recently established as a tool for local and periodical patterning of metals [23–25] and polymers [26, 27]. It takes the advantages of being a pre-patterning-free procedure similar to LIC but not

limited to crystallization. The process provides the combined ability of influencing morphology (*e.g.* by creating a topography), microstructure (phase transformation, grain growth) and material's properties (hardness, friction coefficient, electrical resistivity) in an easy and cost efficient approach.

LIMET (also named Laser Interference Patterning) is used in this dissertation as a tool to produce the investigated direct laser-induced modification of thin films' physical and chemical properties by the creation of particular morphologies and microstructures.

## 1.2 Motivation

The work presented in the following dissertation was motivated by the microstructure modifications and their resulting influence on the intrinsic properties of thin films. To achieve a precise tailoring of microstructures, Laser Interference Patterning (LIP) was chosen, given its high potential for advanced functionalization [28–30] and local influence on intrinsic materials properties such as mechanical, optical, electrical and tribological properties [26, 31–33]. The idea was to use laser light to induce effective properties that act on the macroscale by producing long-range periodic architectures on the microscale. For example, nano and microcrystalline regions were produced in line-shaped grain size arrays. Composite materials are generally composed of two or more constituent materials (*e.g.* hard abrasive particles in a soft matrix) or alternating multiple layers (*e.g.* plywood, damascus steel), each possessing significantly different physical and chemical properties. This includes, however, additional steps in the fabrication of such materials. To overcome the added complexity, a one-step direct modification of the entire film thickness should be induced by using the modulated intensity of interfering laser light. Consequently, a composite effect in a single layer is generated, without any other subsequent fabrication steps (see figure 1.1). It was possible to influence the morphology and microstructure of thin films in order to subsequently affect their physical and chemical properties.

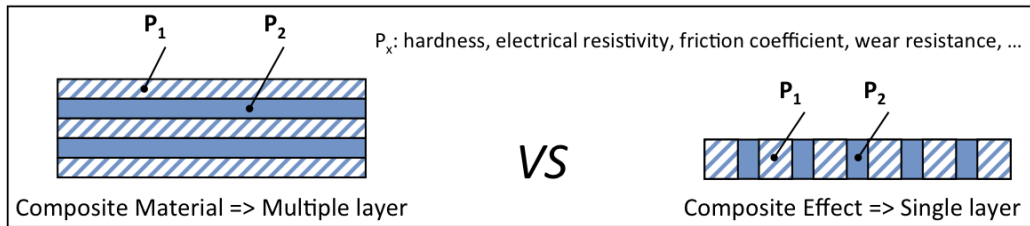


**Figure 1.1:** Illustration of the laser-induced composite effect via Laser Interference Patterning. A direct microstructure modification is aimed at influencing materials properties ( $P_x$ ) such as hardness, electrical resistivity, friction coefficient or wear resistance.

The key thread of the results reported in the present work is hence the effects produced through microstructure modulation in different pure metal



and metal-embedded thin films via Laser Interference Patterning [24,25]. To reveal the breakthrough of this novel technique, three main objectives were targeted:

- The design of advanced architectures induced by local melting and crystallization over the entire film thickness,
- The morphological, microstructural and thermal evolution of the obtained long-range ordered architectures of grain sizes and orientations (arrays),
- The exploitation of the LIP technique for electrical and tribological applications, *e.g.* (i) for local enhancement of film conductivity and (ii) for friction reduction in relevant technical systems such as electrical contacts under friction.

Different systems were considered for the investigations. First of all, thin films of pure noble metals (Pt and Au) were used to study the production of microstructure arrays. Given their ideal behaviour, due to a high resistance against corrosion and oxidation while applying thermal treatment, these films were selected as a model system. Additional pure metals were used (W and Cu) for comparison. Tungsten (W) shows the highest melting point of the metal class and thus a different reaction to a laser-induced temperature gradient is expected. Copper (Cu) is a half noble metal characterized by outstanding thermal and electrical conductivity as well as good corrosion resistance combined with a reasonable tensile strength. As a natural antimicrobial material, the intrinsic properties of pure copper make it an interesting system to be studied and confronted with other systems. To reveal potential applications for the microstructural design of such architectures and based on the expertise of french partners (*Institut Jean Lamour, Nancy, France*), the following systems were additionally chosen: (a)  $Cu_3N$  and (b)  $Pd_{0.25}Pt_{0.75}O_x$  for electrical properties and (c) yttria-stabilized zirconia with incorporated Au nanoparticles (*Au – YSZ*) for tribological applications. The choice of noble metal oxide (b) is based on the laser-induced decomposition into noble metal and oxygen, resulting from a high local heating of the samples. The resistivity of the decomposed metals is thus lower than the resistivity of

the original metal oxide. This effect, not being present in pure noble metals where LIP only induces grain growth or (re)crystallization, would not significantly affect the film resistivity. In the case of (a), the macroscopic film resistivity could be modified due to an induced partial decomposition of copper nitride in metallic copper (and the evaporation of nitrogen), inducing the coexistence of two low and high resistivity phases. Concerning (c), LIP is expected to locally promote a crystal grain growth and segregation of Au embedded nanoparticles and to lead to a significant effect on the friction behaviour.

The results obtained within the research activities summarized in this doctoral thesis have been fully or partially published in peer-reviewed scientific journals and conference proceedings as listed below:

1. R. Catrin, D. Horwat, T. Gries, B. Raillard, J.-F. Pierson, S. Migot, F. Mücklich. *Journal of Materials Research*, 27(6):879-885, 2012 (*Invited Feature Paper*) [34]
2. R. Catrin, T. Gries, D. Horwat, S. Migot, F. Mücklich. In *Materials Research Society Symposium Proceedings*, vol. 1339, p. mrss11-1339-(s01-04), 2011 [35]
3. R. Catrin, D. Horwat, J-F. Pierson, S. Migot, Y. Hu, F. Mücklich. *Applied Surface Science*, 257(12):5223-5229, 2011 [36]
4. M. Hans, C. Gachot, R. Catrin, B. Raillard and F. Mücklich. *Metall*, 63(11):579-581, 2009 [37]
5. R. Catrin, C. Gachot, G. Marchand, U. Schmid, F. Mücklich. In *Proceedings of SPIE*, vol. 7362, p. 736217-(1-6), 2009 [38]
6. C. Gachot, R. Catrin, A. Lasagni, U. Schmid, F. Mücklich. *Applied Surface Science*, 255(10):5626-5632, 2009 [22]
7. R. Catrin, A. Lasagni, C. Gachot, U. Schmid, F. Mücklich. *Advanced Engineering Materials*, 10(5):466-470, 2008. (*Cover page*) [21]
8. F. Mücklich, C. Gachot, R. Catrin, U. Schmid, A. Lasagni. In *Materials Research Society Symposium Proceedings*, 1059:KK(04-06), 2008 [39]

Aside the relevant theoretical background proposed in chapter 2 and the description in chapter 3, of the experimental procedure, the results of the objectives fixed above are organized in four chapters.

Chapter 4 deals with the **microstructural evolutions** of patterned pure metallic films through the formation of different grain-size regimes. Hereby, the possibility of fabricating periodic arrays with well-defined grain architectures under controlled parameters is shown. Additionally, the effect of a change in the grain-size regime on the mechanical behaviour is also considered. A **composite combination** of soft/hard nanoscale grains and hard/soft microscale grains is induced.

In chapter 5, a wet chemical etching procedure is applied to the previous pure metallic films, whose tailored microstructure is intended to be tested for a possible alternative and low cost approach to conventional lithographic techniques. A novel method for **straight-forward patterning** of metallic thin films is suggested.

Chapter 6 gives insight into the potential of the LIP technique to influence the film resistivity by a laser-assisted chemical decomposition processes. A significant **decrease of the film resistivity measured at the macro-scale due to microstructural modifications in the micro-scale** is concluded. An effective medium [40] that allows better electrical conduction paths is generated.

Chapter 7 summarizes the microstructural and tribological influences of LIP on soft nanoparticles (Au) embedded in a hard matrix (YSZ). The massive impact of LIP on the **reduction of the friction coefficient** in this system is shown. Through an induced localized crystal growth of Au and its segregation near the surface of defined regions, a potential **dry lubrication effect** could be revealed [41–43].

Finally, the overall conclusions and outlook of this work are detailed in chapter 8.



## Chapter 2

# Using laser light for surface engineering

**ABSTRACT:** More than fifty years ago, in May of 1960 in California, Theodore Maiman invented the first laser principally composed of a ruby and an intense flash lamp. What was thought at that time as a "laboratory curiosity", was actually the beginning of a new era in materials science and a revolution in everyday life. The remarkable properties of laser beams allow a large diversification of their applications. Lasers are a primary component of some of our more modern communication systems, they are used to read barcodes, in laser printing or in compact disk players. Lasers radically transform industrial processes, where they are used for cutting, drilling, welding or heat treatment. In medicine, lasers are commonly used *e.g.* for hair or tattoo removal; in ophthalmology for surgery, where precise and localized treatments are needed. Lasers are also under constant development in laboratories, and the current global laser market is estimated at about \$6 billion yearly. The laser principle and the required elements to obtain a laser beam are described in section 2.1. Additionally, the interaction between laser beams and matter, particularly the effects induced in metals are also reported in section 2.2. A brief overview of the interference principle of laser light as well as the patterning technique applied in this work are finally given in section 2.3.

## 2.1 Laser principle

A laser consists in a highly directional, high-intensity beam with a typically very pure frequency or wavelength. Contrary to common light such as incandescent lamps or LED's, which emit light in multiple directions, laser light propagates parallel waves in one direction over long distances. This property is called spatial coherence. Additionally, laser light is monochromatic with wavelengths ranging from the microwave and infrared (IR) regions through the visible, ultraviolet (UV), vacuum ultraviolet, and into the soft-X-ray spectral regions. This property is called temporal coherence. LASER is an acronym for Light Amplification by Stimulated Emission of Radiation. Stimulated emission of radiation is a natural process first identified by A. Einstein in 1917. It occurs as a beam of light passes through a specially prepared medium and stimulates its atoms to emit light in exactly the same direction and wavelength as that of the original beam [44]. In 1954, Townes and Schawlow [45] designed the first device using Microwave Amplification by Stimulated Emission of Radiation (MASER). It constituted the premiss of the first laser fabricated by Maiman [46]: a laser beam with a 694.3 nm wavelength, opening a new age in the field of optics.

### 2.1.1 Amplification by stimulated emission of radiation

Laser light is produced as a result of electrons jumping from an excited energy level (within a radiating species) to a lower-lying energy level. During this process, radiating light contributes to the laser beam. The radiating species include atoms (HeNe laser), molecules ( $CO_2$  laser), liquids, dielectric solids (Nd:YAG laser) and semiconductor materials. At room temperature, each of these species possesses its lowest energy level referred to as the ground state. By means of an external energy source (pumping), the electrons are moved to higher levels, called excited levels. The electrons then decay back to lower levels within a particular period of time (lifetime of the level). Three types of processes involving light/atom interaction exist: spontaneous emission, absorption and *stimulated emission*. The latter is responsible for inducing laser light and will be further developed. Stimulated emission (see figure

2.2a) results from the collision of an electron in a higher-lying level and a photon with the atom. During this process, the photon stimulates the atom to radiate a second photon having exactly the same energy as that of the incident photon and traveling in the same direction, satisfying the laws of conservation of energy and momentum. Hence, one photon leads to two identical photons, resulting in light amplification as seen in figure 2.1. However, stimulated emission is attenuated by the process of absorption which occurs simultaneously. Spontaneous emission also tends to attenuate the stimulated emission that is needed for light amplification. Hence, stimulated emission must be the predominant process.

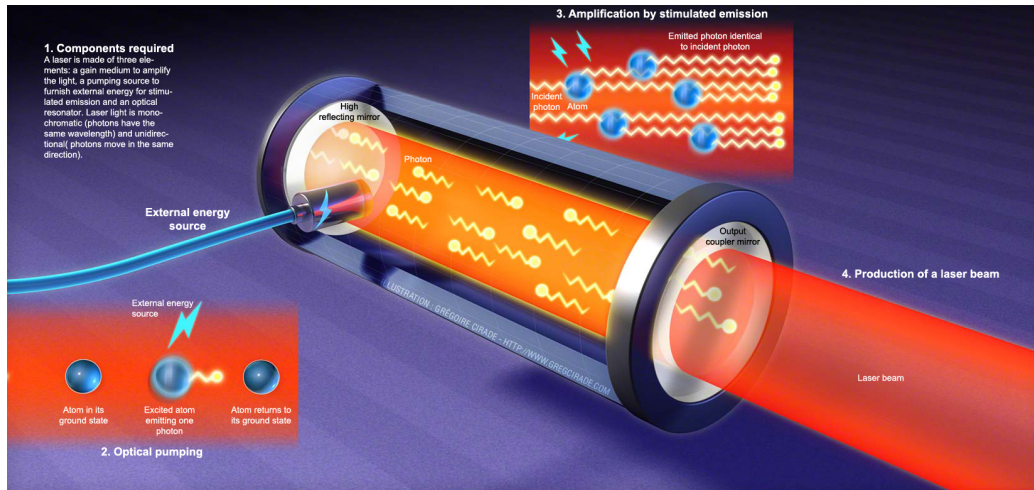


**Figure 2.1:** General overview of a laser with a description of the different components and physical processes required for the emission of a laser beam. *Reproduced with permission*

Einstein showed that the probability of absorption is numerically equal to the probability of stimulated emission [47]. Stimulated emission is therefore the inverse process of absorption. The sole difference is that absorption is proportional to the population density  $n_1$  of atoms residing in the ground state and stimulated emission is proportional to the population  $n_2$  residing in the excited level. For stimulated emission to become predominant, the condition  $n_2 > n_1$  must be satisfied. This phenomenon is called *population inversion*. However, the fulfillment of this condition is not trivial, as atoms are naturally in their lowest energy level (ground state) due to spontaneous

emission (equilibrium). In order to impose a non-equilibrium state on an atom, external energy must be provided in order for the atom to attain its excited state. This process is called *pumping*.

### 2.1.2 Laser pumping and optical cavity

Laser pumping consists in populating level 2 ( $n_2$ , excited) while depopulating level 1 ( $n_1$ , ground state) so that population inversion can occur. Furnishing energy to the atoms is thus needed and part of this energy will be then restituted within the amplification of the radiation at the frequency  $\nu$ . Several pumping methods such as electrical, chemical or optical methods are available, in which energy comes from different sources. Optical pumping of lasers generally applies to the pumping of liquid (dye) lasers and to dielectric solid-state lasers and is provided by either flash lamps or other lasers. However, the use of radiation at the frequency  $\nu$  resonating with the transition between levels 1 and 2 is not convenient. Even if the radiation is intense, the maximum that could be induced is  $n_1 = n_2$ , inducing transitions equally within stimulated emission and absorption. Population inversion is thus impossible with a two-level optical pumping. A three-level (figure 2.2b) or even four-level (figure 2.2c) optical pumping is thus preferred.

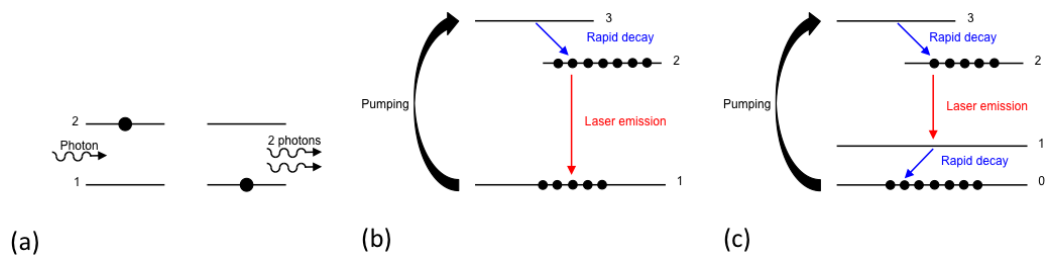


**Figure 2.2:** Schematic representation of (a) the stimulated emission, (b) a three-level pumping and (c) a four-level optical pumping.

In a four-level optical pumping, the energy level  $E_1$  is no longer the ground state of the atom: it is then possible to populate the high-level of the transition, while having the lowest level sparsely populated because of spontaneous deexcitation towards the ground state. This type of pumping is more suitable



*e.g.* for a laser working continuously and is also used in HeNe lasers.

Laser beam properties (direction, divergence, profile, etc.) are determined largely by the laser mirrors. Much like the Larsen effect (audio feedback), which occurs when a sound loop exists between an audio input (microphone) and an audio output (loudspeaker), the emitted light must return in the gain medium (amplifier) in order to induce an oscillation of the light (electromagnetic field). Therefore the re-injected light and the light wave must be in phase to achieve an amplification after each pass through the gain medium. In practice, the laser mirrors have to be well arranged to form a resonating optical cavity, the length of which is an integer multiple of the light's wavelength.

A **laser** can therefore be defined as a **source of coherent light**, consisting of an optical gain medium (amplifier) that is **pumped by an external energy source** and placed in a **resonating optical cavity** composed of several mirrors.

## 2.2 Laser-matter interaction

In order to induce a structural transformation in a material by means of light, the absorption mechanisms and dynamics have to be considered first. It is fundamental to remember that only the amount of energy absorbed by the material can contribute to processes like heating and melting. The absorption of particles without electrical charge and mass, named photons, is the basic principle of such an electromagnetic interaction. Within this interaction, the energy transmitted to the matter is then converted to heat, which induces metallurgical transformations in the irradiated material. Depending on the frequency of the radiation, different interaction mechanisms can be considered. The radiation emitted by lasers is situated between IR and UV, which means roughly between 0.1 and 10  $\mu\text{m}$ . The energy of a photon depends on the frequency  $\nu$  (Hz), thus on the wavelength  $\lambda$  (m) of the propagating wave. The energy quantum  $E_p$  can be expressed in terms of Planck's constant  $h$

and the light celerity  $c$ , given by:

$$E_p = h\nu = \frac{hc}{\lambda} \quad (2.1)$$

### 2.2.1 Wave propagation

Considering Maxwell's theory [48], an electromagnetic wave is characterized by its electric field  $\mathbf{E}$  and magnetic field. When a wave is propagating along the direction  $z$  in a medium with a complex index  $n^*$  (in absorbing media), the resolution of Maxwell's equations gives an expression for the electric field:

$$\mathbf{E} = \mathbf{E}_0 \exp\left(i\omega\left(t - \frac{n^*z}{c}\right)\right) \quad (2.2)$$

where  $\omega$  is the angular frequency ( $\omega = \frac{2\pi c}{\lambda}$ ) and  $t$  the time.

In absorbing media, the real refractive index  $n$  must be replaced by a complex index  $n^* = n - ik$ , where  $k$  is the extinction coefficient. The meaning of this coefficient  $k$  is that upon propagation over a distance  $z$ , the electric field decreases by the factor  $\exp(\frac{\omega kz}{c})$ , indicating that some of the light energy is absorbed. Then, considering an electromagnetic energy beam with an intensity (energy flux)  $I_0$  penetrating into a solid, liquid or gaseous medium, the variation of the transmitted energy  $I(z)$  according to the distance  $z$  depends on the absorption coefficient  $\alpha$  of the medium. The intensity of the electromagnetic wave propagating into the material decreases exponentially following the Lambert-Beer expression, where the absorption coefficient  $\alpha$  is the inverse of the absorption length, as given by:

$$I(z) = I_0 \exp(-\alpha z) \quad (2.3)$$

with:

$$\alpha = \frac{2\omega k}{c} = \frac{4\pi k}{\lambda} \quad (2.4)$$

Furthermore, when a beam of electromagnetic energy penetrates a given medium, a part  $A$  of its intensity is absorbed in the form of heat, a part  $T$

is transmitted through the material and a part  $R$  is reflected, following:

$$1 = A_{abs} + R_{re} + T_{tr} \quad (2.5)$$

where  $A_{abs}$ ,  $R_{re}$  and  $T_{tr}$  are the coefficients of reflexion, absorption and transmission of the material, respectively.

Considering an inhomogeneous medium (1), in which the refractive index varies in space and the reflection (2) of a perpendicularly incident wave in vacuum or air on the flat surface of a solid with refractive index  $n^*$ , the ratio  $R$  of reflected-to-incident irradiance is given by the Fresnel expression:

$$R = \left| \frac{n^* - 1}{n^* + 1} \right|^2 = \frac{(n - 1)^2 + k^2}{(n + 1)^2 + k^2} \quad (2.6)$$

### 2.2.2 Energy absorption by metals

The optical response of a metal is dominated by the conduction electrons, particularly the free electrons, which contribute to the optical properties. The potential energy level of these free electrons in a metal is located in the conduction band. During irradiation, the electrical part of the electromagnetic wave induces an oscillation of the free electrons and their collision in the conduction band. Drude's model describes the absorption of photonic energy (electromagnetic) by these free electrons. The collision effect is characterized by the time  $\tau_c$  between two collisions. The collision frequency  $\omega_c$  is given by:

$$\omega_c = \frac{1}{\tau_c} \quad (2.7)$$

The electrons concerned by Drude's model are those located in an energy band situated near the Fermi level. The width of such an energy band is the energy of a photon. Drude's model can be perfectly applied to current lasers, as the energies considered do not permit transitions between the valence band and the conduction band. However this model is no longer applicable at the highest energy levels, because the detailed knowledge of the electronic structure of a metallic material is needed to consider the contribution of the electrons from the valence band.

In the case of metals and in the wavelength spectrum of current lasers, the frequency of the wavelength  $\omega$  is in the range  $\omega_c < \omega < \omega_p$ , with the plasma frequency  $\omega_p$ , which separates the regime of large  $R$  and  $\alpha$  for  $\omega < \omega_p$  and the regime of small  $R$  and  $\alpha$  for  $\omega > \omega_p$ . Thus in the near-IR and visible regions, for most metals,  $n$  and  $k$  are as follows [48]:

$$n \simeq \frac{\omega_p}{2\omega^2\tau_c} \simeq 0 \quad \text{and} \quad k \simeq \frac{\omega_p}{\omega} \quad (2.8)$$

The reflection coefficient  $R$  is thus related to the DC conductivity  $\sigma_0$  by:

$$1 - R \simeq \frac{2}{\omega_p\tau_c} = \frac{2\epsilon_0\omega_p}{\sigma_0} \quad \text{and} \quad \alpha \simeq \frac{2\omega_p}{c} \quad (2.9)$$

where  $\epsilon_0$  is the dielectric constant in vacuum and  $c$  is the light celerity.

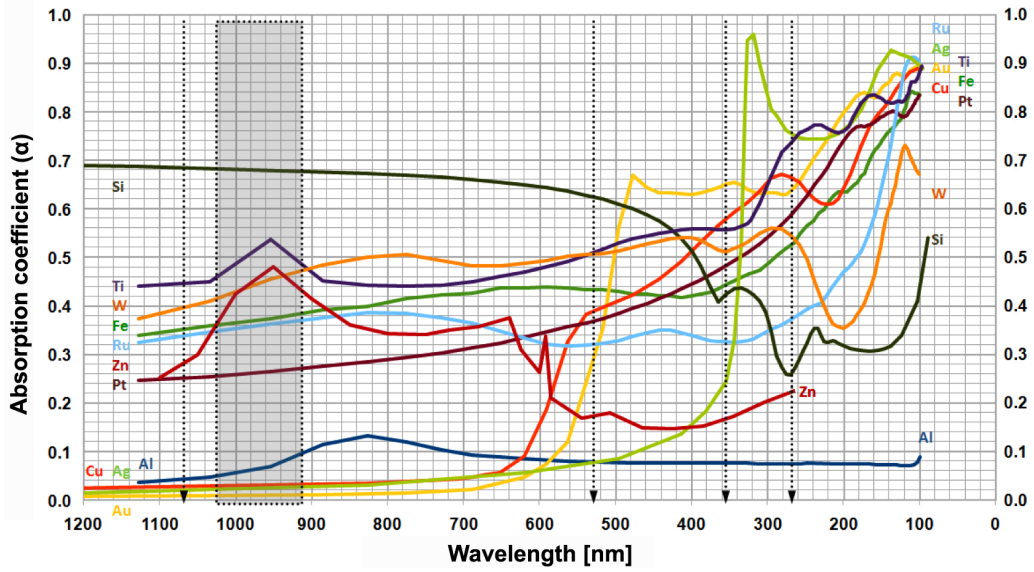


**Figure 2.3:** Evolution of the absorption coefficient  $\alpha$  (tabulated from [49]) with the wavelength  $\lambda$  of some metals and semiconductors. Three arrows specify  $\alpha$  at specific wavelengths available within the laser facility: 266, 355 and 1064 nm.

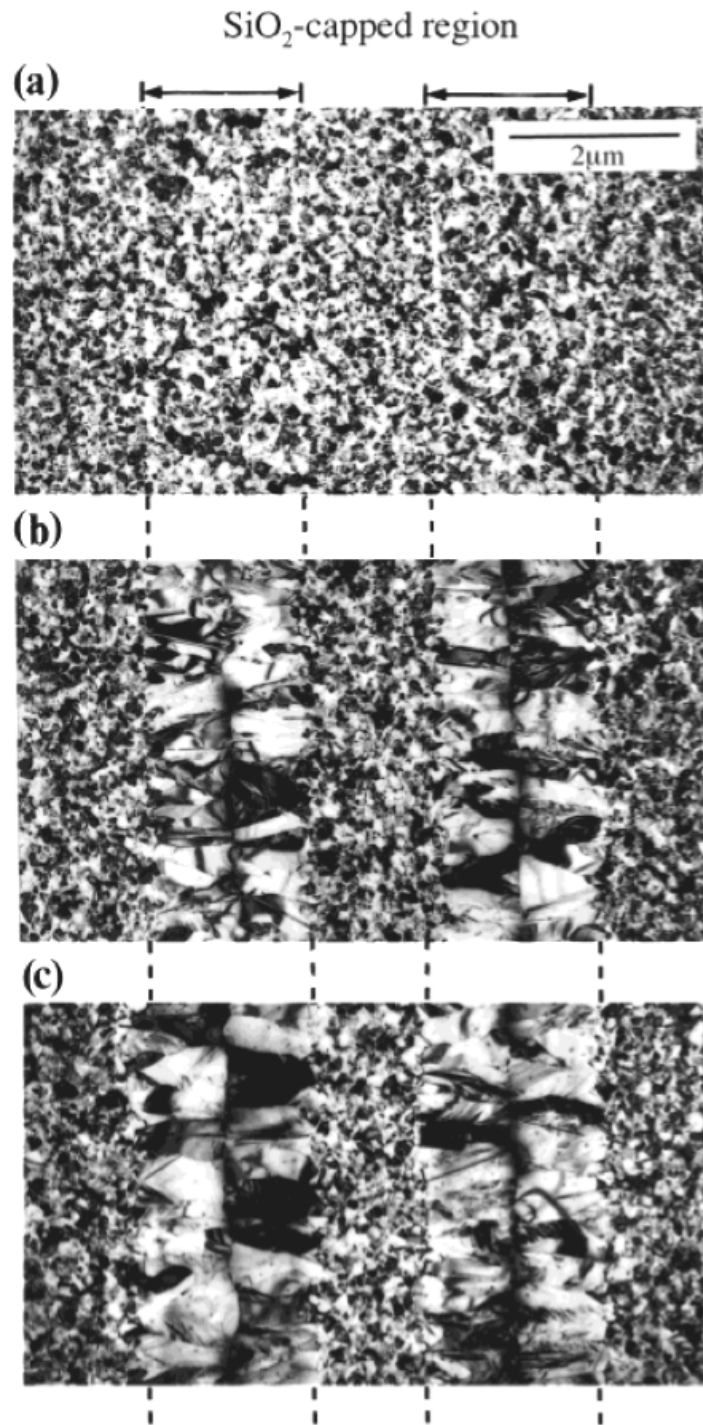
Figure 2.3 shows the evolution of the absorption coefficients of several metals depending on the wavelength.

### 2.2.3 Laser-induced crystallization

Combining laser interference patterning (LIP) with a nanosecond pulse duration on amorphous or nanocrystalline thin films can lead to changes in their microstructural properties. The films are molten as a result of an exposure to a laser pulse with an intensity above a certain threshold, and solidify leading to (re)crystallization at the local periodic heat zones. In the particular case of *super lateral growth* regime (SLG), it is possible to induce different effects such as the formation of large-grained polycrystal microstructures, directionally solidified microstructures, or location-controlled single-crystal regions in which grain sizes are many times bigger than the film thickness (up to several micrometers) [6].

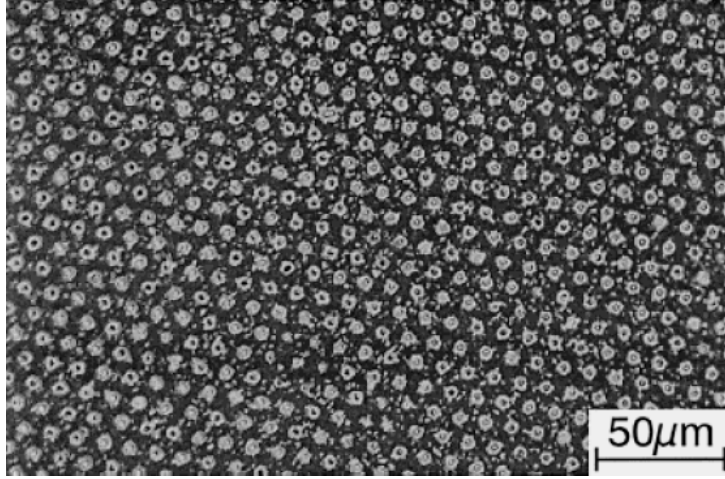
Three regimes are considered during laser-induced crystallization. The first one is known as the *low energy density regime*, in which the incident energy of the laser pulse is sufficient to induce partial melting of the thin films. The second is the *high energy density regime*, with incident energy high enough to melt the films completely. Finally, there is a *threshold energy density*, which leads to near-complete melting and generally depends on the film thickness, the pulse duration, the substrate temperature and the substrate conductivity [6]. Due to the near-complete melting of the films, the SLG regime (between partial and complete melting), can lead to the formation of large-grained microstructures. Im and co-workers [6] conducted experiments on Si films and argued that at the maximum point of melting, the non-molten portion of the underlying Si no longer forms a continuous layer, but consist of solid islands separated by small local regions having undergone complete melting. For this reason, non-negligible lateral growth can appear, starting from the non-molten islands that act as solidification seeds.

Figure 2.4 shows a TEM micrograph of a 100 nm thick Si film on top of a 2  $\mu\text{m}$  thick  $\text{SiO}_2$  layer. This layer was irradiated applying a single pulse of a uniform incident beam. At an incident energy density of 190  $\text{mJ}/\text{cm}^2$ , a small-grained microstructure is obtained (figure 2.4a). When increasing the laser intensity (290  $\text{mJ}/\text{cm}^2$ ), a *controlled* super lateral growth (c-SLG) microstructure can be obtained as shown in figure 2.4b. At this radiation inten-



**Figure 2.4:** Transmission electron micrographs (bright-field) of single-pulse-irradiated 100 nm Si films with a patterned  $\text{SiO}_2$  antireflective coating, irradiated at (a)  $190 \text{ mJ/cm}^2$ , (b)  $290 \text{ mJ/cm}^2$ , and (c)  $340 \text{ mJ/cm}^2$ , respectively. Reprinted from [6]

sity, the capped Si film region is completely molten, whereas the uncapped region is only partially molten [6]. The resulting microstructure shown in figures 2.4b and 2.4c consists of elongated and lateral columnar grains that originate from the unmolten regions of the film and meet at the centre of the laser-treated area. Due to a quick occlusion of a significant number of grains (particularly near the onset of growth), which starts in the small-grained region, not all of them reach the centre. In figure 2.4c, where the sample was irradiated at an even higher incident energy density ( $340 \text{ mJ/cm}^2$ ), the microstructure seems to be identical to the c-SLG microstructure shown in figure 2.4b [6].



**Figure 2.5:** Optical micrograph of an orientation-induced crystallised Si film. The large and periodically spaced bright areas represent (111)-oriented grains crystallized at  $600 \text{ }^\circ\text{C}$  for 2h. *Reprinted from [50]*

In the case of interference patterns produced by several coherent laser beams, it is possible to locally and periodically melt the material, inducing SLG. At the interference maxima positions where the films are locally heated, seeding points can be induced and a further annealing process favours (re)crystallisation only at the previously defined nucleation centres (see figure 2.5). The adjacent intensity minima regions are only partially affected. This allows a control of the lateral grain growth with a long-range order. By spatial modulation of the laser intensity, it is possible to generate nar-

row grain size distributions and controlled grain orientations [51]. Kelly and co-workers [17, 52] have shown the effect of a so called laser-crystallisation to produce microcrystalline Si seeds in amorphous silicon. Moreover, LIP applied using three laser beams leads to the formation of a periodic two-dimensional interference dot-like pattern. At the interference maxima, the intensity is high enough to induce crystallisation of the amorphous Si film, thereby promoting the formation of large grains, while at the interference minima the energy remains below this threshold value [6].

This method was also applied by Eisele et al. [53] in order to improve the absorption of silicon thin film solar cells. Melting and solidification lead to the formation of grain sizes as wide as the interference pattern period because of the stimulation of the lateral grain growth along the temperature gradient in the film. A schematic description of this phenomenon is shown in figure 2.6. Grains grow from both sides of the molten line and meet at the centre, causing topographical effects at the meeting point.

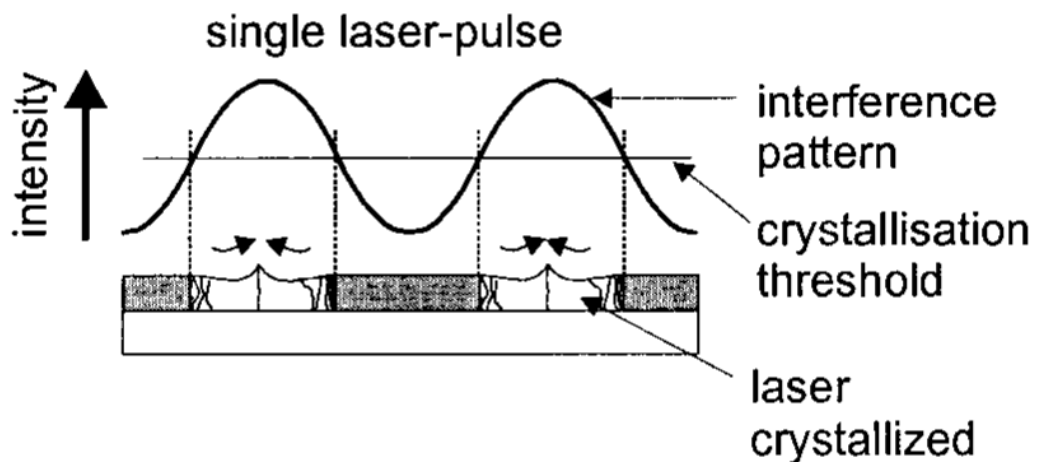


**Figure 2.6:** Schematic representation of the laser interference crystallization process in amorphous silicon. *Reprinted from [53]*



## 2.3 Laser interference patterning

### 2.3.1 Beam path

The concept of *laser interference metallurgy* (LIMET) was coined by Mücklich et al. to describe the patterning of metallic surfaces by interfering laser beams [25]. Principally, interfering laser beams of a high-power pulsed laser allow a direct lateral treatment of the metal's surface microstructure on the micro/nano-scale, based on photo-thermal mechanisms [54]. This recently developed technique allows the formation of well-defined long-range ordered periodic patterns at a typical microstructure scale (*i.e.* from the sub-micrometer level up to several micrometers) [23, 25, 55]. It covers large areas with interference periodicity fields produced by several coherent laser beams stimulating different metallurgical processes, such as melting, (re)crystallization, recovery, defect and phase formation. This technique requires one single preparation step whereas other structuring techniques comprise at least two (holography, irradiation, etching, etc) [56]. No masks are required and depending on the material, relatively large areas up to the  $cm^2$  range can be directly structured during each single irradiation pulse.

### 2.3.2 Interference principle of laser light

*Laser interference patterning (LIP)* is based on the interference principle of light. To calculate interference patterns, laser light is assumed to be perfectly monochromatic, with linear polarized plane waves. Then, the total electric field  $E$  of the interference pattern can be obtained by adding all  $n$  individual beams  $i$  in terms of  $\alpha_i$ ,  $\beta_i$ , which are the angles between the beams with respect to the interference plane (x,y,z) as illustrated in figure 2.7 and described in equation 2.10 [57]:

$$E = \sum_{i=1}^n E_i = \sum_{i=1}^n E_{i0} e^{-ik \sin \alpha_i (x \cos \beta_i - y \sin \beta_i)} \quad (2.10)$$

where  $E_{i0}$  is the amplitude of the electric field of each beam  $i$ ,  $k$  the wave number,  $\alpha_i$  and  $\beta_i$  the angles of the beams reaching the sample surface. The

wave number is directly connected to the beam wavelength  $\lambda$  through:

$$k = \frac{2\pi}{\lambda} \quad (2.11)$$

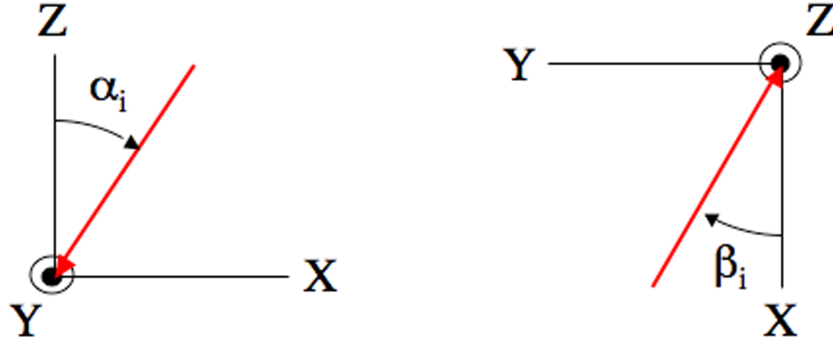


**Figure 2.7:** 3D representation of an electromagnetic wave.  $\alpha_i$  and  $\beta_i$  are the respective angles between the beams and the (x,z) and (x,y) interference planes.

The intensity distribution  $I$  of several beams can be evaluated through:

$$I \propto |E|^2 \quad (2.12)$$

and can be calculated, *e.g.* in the case of:

- two-beam interference with  $E_{01} = E_{02} = E_0$ ;  $\alpha_1 = \alpha_2 = \alpha$ ;  $\beta_1 = 0, \beta_2 = \pi$  by:

$$I \propto 4E_0^2 \cos^2(kx \sin \alpha) \quad (2.13)$$

A periodic **line-like** patterning is obtained (see figure 2.8) and characterized by a period  $P$  given by:

$$P = \frac{\lambda}{2 \sin(\frac{\theta}{2})} \quad (2.14)$$

where  $\theta$  is the angle between the laser beams.

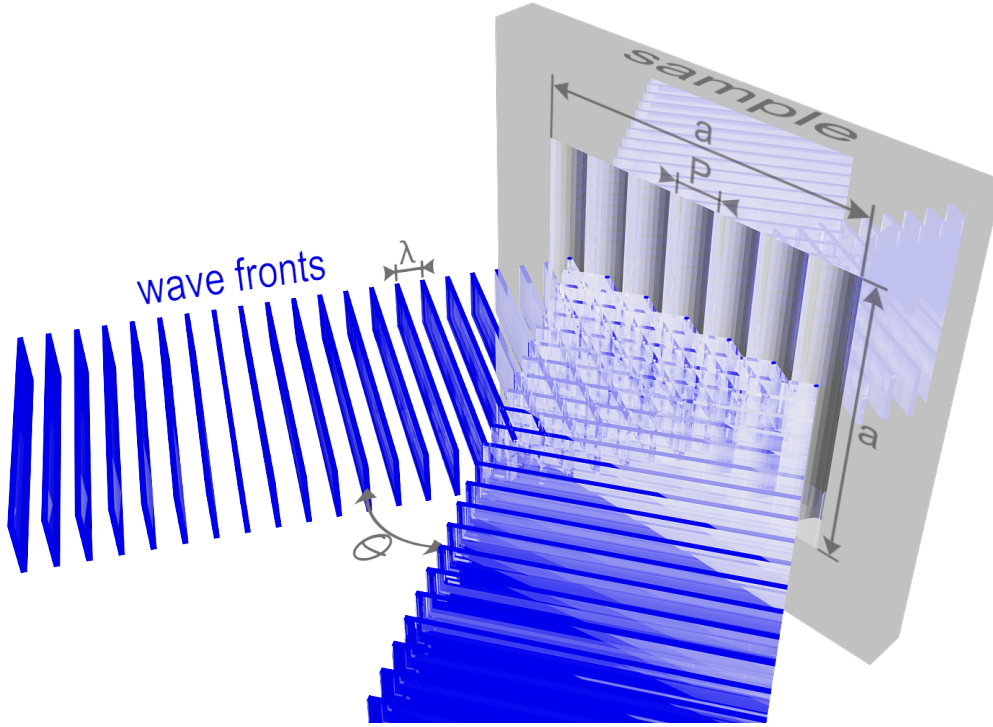


**Figure 2.8:** Schematic representation of two-beam interference, producing a line-like pattern. The wavelength  $\lambda$  and the angle between the two beams  $\theta$  directly define the structure period  $P$  in the patterned surface  $a^2$ . A cross-section of the beam is shown in order to view the resulting structure, otherwise hidden by the wave fronts.

- three-beam interference with  $E_{01} = E_{02} = E_{03} = E_0$ ;  $\alpha_1 = \alpha_2 = \alpha_3 = \alpha$ ;  $\beta_1 = 0, \beta_2 = \frac{2\pi}{3}, \beta_3 = -\frac{2\pi}{3}$  by:

$$I \propto E_0^2 \propto$$

$$\left[ \begin{aligned} & \left( -\cos(kx \sin \alpha) - \cos \left( k \sin \alpha \left( -\frac{x}{2} - y \frac{\sqrt{3}}{2} \right) \right) - \cos \left( k \sin \alpha \left( -\frac{x}{2} + y \frac{\sqrt{3}}{2} \right) \right) \right)^2 \\ & + \left( -\sin(kx \sin \alpha) + \sin \left( k \sin \alpha \left( -\frac{x}{2} - y \frac{\sqrt{3}}{2} \right) \right) - \sin \left( k \sin \alpha \left( -\frac{x}{2} + y \frac{\sqrt{3}}{2} \right) \right) \right)^2 \end{aligned} \right]^2 \quad (2.15)$$

A periodic **dot-like** patterning is obtained (see figure 2.9).

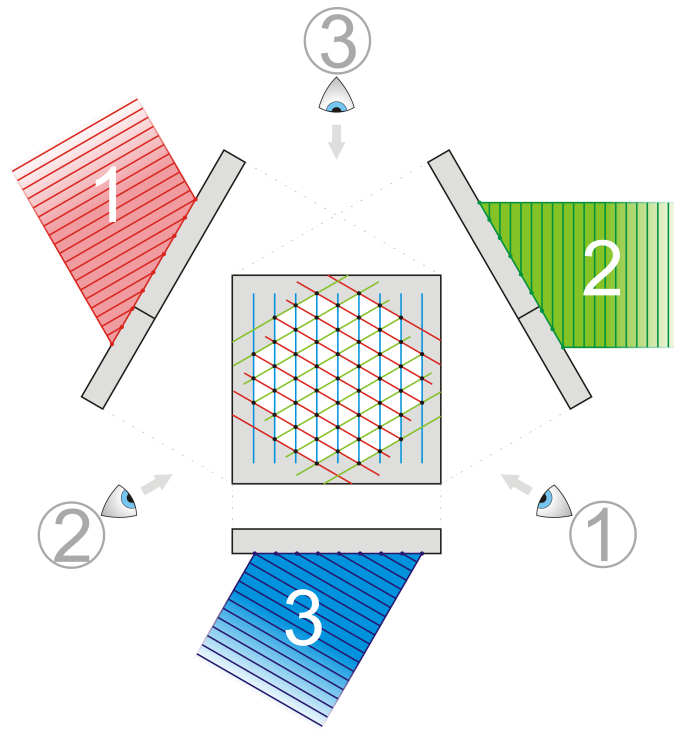


**Figure 2.9:** Schematic representation of three-beam interference, producing a dot-like pattern. The three sub-beams (1, 2, 3) have the same wavelength, but are coloured differently for optimal rendering.

Figure 2.10 below gives a 3D view of three incoming sub-beams (having the same wavelength) interfering at the sample surface.

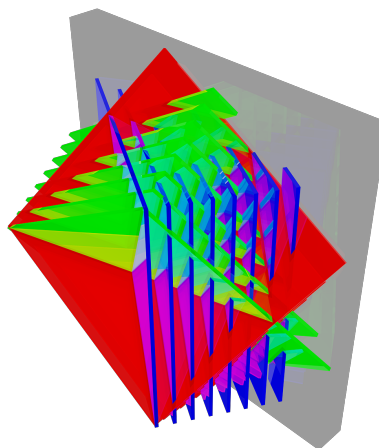


**Figure 2.10:** 3D representation of the three sub-beams interfering on the sample surface.

# Chapter 3

## Experimental approach

**ABSTRACT:** The different thin films studied in this work were synthesized by means of electron beam evaporation (chapters 4 and 5) or magnetron sputtering (chapters 6 and 7). The subsequent laser treatment procedure by laser interference patterning is reported in order to investigate the influence of laser irradiation on the metal-based films. A further chemical etching in aqua regia was performed on the films studied in chapter 5. The characterization of the films was mainly done using White Light Interferometry (WLI) and a dual beam workstation comprising a Scanning Electron Microscope (SEM) equipped with a field emission gun, and a Focused Ion Beam (FIB). The microstructure analysis was obtained by X-ray Diffraction (XRD), Transmission Electron Microscopy (TEM) and Electron Backscattered Diffraction (EBSD) in order to investigate the laser-induced physical processes that govern the laser-matter interactions. Finally, several materials properties (hardness, film resistivity and friction coefficient) were measured in order to determine the modifications induced by the laser interference patterning procedure used in this work and to report on the suitability of the results in the foreseen applications. In view of the latter, nanoindentation, the four-point probe method and nanotribometry were applied.

## 3.1 Film preparation

### 3.1.1 Electron beam evaporation

Electron beam (e-beam) evaporation was used to produce the Ti/Pt and Ti/Au bilayers (15 nm/300 nm) used in chapters 4 and 5. This was done on double-sided polished, (100)-oriented p-type silicon wafers ( $\varnothing = 4''$ ,  $\rho_{Si} = 5 - 50 \Omega \cdot \text{cm}$ , 300  $\mu\text{m}$  thick) from pellets with a purity of 99.95 % in standard equipment from Balzers (PLS 570). At a residual base pressure of less than  $5 \cdot 10^{-7}$  mbar, the deposition process of both metal types started and was performed subsequently without breaking the vacuum to avoid oxidation effects. The titanium layers deposited with a rate of about 0.4 nm/s have a nominal thickness of 15 nm and serve as an adhesion promoter. The Pt and Au top layers were synthesized with an emission current of 250 mA resulting in a growth rate of about 0.5 nm/s. During deposition none of the substrates were nominally heated and all substrates were placed on a rotary stage, ensuring improved homogeneity of the layer thickness within the samples and from sample to sample. The distance between the pellet and the sample holder was about 60 cm. Before irradiation, the 4'' wafer was diced into specimens of about 10x10 mm<sup>2</sup> to fit into the experimental set-up and to ease the handling [58, 59].

### 3.1.2 Magnetron sputtering

A magnetron sputter facility (Von Ardenne, PPS - A200) was employed to synthesize the 300 nm thick Ti/W films on (100)-oriented silicon wafers. The following sputter parameters were applied: sputter power (500 W), argon gas pressure ( $3 \cdot 10^{-3}$  mbar) and gas flow (60 sccm).

A second magnetron sputtering facility was used to produce the  $\text{Cu}_3\text{N}$  and  $\text{Pd}_{0.25}\text{Pt}_{0.75}\text{O}_x$  used in chapter 6 and the gold-incorporated yttria stabilized zirconia matrix ( $\text{Au} - \text{YSZ}$ ) films used in chapter 7. The experimental device used is a sputtering chamber (40 L) pumped down via a combination of a back and a turbomolecular pump allowing a base vacuum of  $10^{-6}$  mbar. The gas flow rates were regulated using MKS flowmeters. The facility is

equipped with two magnetron systems separated by 120 mm and 100 mm from each other, in the case of  $Cu_3N$  /  $Pd_{0.25}Pt_{0.75}O_x$  and  $Au - YSZ$  respectively. The films were deposited on sodalime glass slides. The distance between the glass substrates and the targets was fixed at 50 mm, except for gold, which was fixed at 100 mm. The films were deposited without external heating and the deposition temperature reached was close to 50 °C.

For the work detailed in chapter 6, 550 nm thick  $Cu_3N$  films were deposited by reactive magnetron sputtering of a copper target ( $\varnothing = 50$  mm, 3 mm thick and purity over 99.9 %). The copper target was powered by an Advanced Energy Pinnacle+ 5 kW DC pulse generator in an argon nitrogen mixture. The argon and nitrogen gas flow rates were fixed to 30 and 10 sccm, respectively. The total pressure was measured close to  $7 \cdot 10^{-3}$  mbar by a MKS Baratron absolute gauge. The discharge frequency was fixed at 50 kHz and the off-time at 4  $\mu$ s. The current applied to the copper target was kept constant at 0.3 A. 350 nm thick  $Pd_{0.25}Pt_{0.75}O_x$  films were deposited by reactive magnetron co-sputtering using palladium and platinum targets ( $\varnothing = 50$  mm, 3 mm thick and purity over 99.9 %). The palladium and platinum targets were powered by an Advanced Energy Pinnacle+ 5 kW DC pulse generator in pure oxygen operated at 350 kHz, off-time 1.4  $\mu$ s and at 315 kHz, off-time 1.1  $\mu$ s, for Pt and Pd respectively. The oxygen gas flow rate was 30 sccm and the total pressure was measured close to  $3 \cdot 10^{-3}$  mbar by a MKS Baratron absolute gauge. The current applied to the palladium and platinum targets was set to 1 A. The deposition duration was fixed to 20 min and the film thickness has been evaluated by tactile profilometry with an accuracy of 20 nm and verified by focused ion beam.

For the work detailed in chapter 7, 140 nm thick Au-YSZ films were deposited in similar conditions as described above. The deposition was also performed by reactive magnetron co-sputtering of gold and Zr/Y targets ( $\varnothing = 50$  mm, 3 mm thick and purity over 99.9 %). The Zr/Y target, composed of  $Zr_{0.84}Y_{0.16}$ , was powered by an Advanced Energy Pinnacle+ 5 kW DC pulsed generator operated at 50 kHz, off-time 4  $\mu$ s and the Au target by an Advanced Energy MDX 1.5 kW DC generator. Argon and oxygen flow rates were regulated using Alphagaz flowmeters at 20 and 6.3 sccm, respectively.

Within these deposition conditions, the total pressure was measured close to  $2.5 \cdot 10^{-3}$  mbar by an MKS Baratron absolute gauge. The currents applied to the Zr/Y and Au targets were 0.7 A and 0.1 A, respectively. These conditions resulted in a metal atomic ratio  $\text{Au}/(\text{Au}+\text{Zr}+\text{Y})$  close to 0.55 as measured by Energy Dispersive X-ray Spectrometry (EDS). The deposition duration was fixed at 3 min 45 s. Moreover, a 300 nm thick YSZ film was deposited by sputtering the Zr/Y target alone under similar conditions. The deposition time was 20 min.

### **3.1.3 Chemical etching**

Chemical etching was carried out on the Ti/Pt and Ti/Au samples studied in chapter 5 by applying aqua regia. This etchant is a mixture of concentrated nitric acid, concentrated hydrochloric acid and water, used at a volumetric ratio of 1:8:7 ( $\text{HNO}_3 : \text{HCl} : \text{H}_2\text{O}$ ). This solution is commonly used to dissolve inert noble metals like gold and platinum [60]. To achieve an acceptable etch rate, aqua regia is heated to 65 °C for the platinum and 35 °C for the gold thin films. Typical etch rates for Pt and Au are  $\approx 3.6$  nm/min and  $\approx 680$  nm/min, respectively [61]. The samples were put into the etching solution for 3 min. Subsequently, they were rinsed with deionised water and dried with purified air for inspection purposes.

## **3.2 Laser interference arrangement**

The principle of interference applied to laser light, as described in section 2.3, was applied to the samples studied in this work. A high power nanosecond pulse Nd:YAG ( $\text{Nd} : \text{Y}_3\text{Al}_5\text{O}_{12}$ ) laser from Spectra Physics (Quanta Ray PRO 290), working at a fundamental wavelength of 1064 nm was used. The pulse duration is 10 ns and the repetition rate (frequency) is set to 10 Hz. For the best absorption in most of the considered species (see figure 2.3 in section 2.2.2) and due to technical considerations of the available optics in the UV range, the samples were irradiated by the third harmonic at a wavelength of 355 nm. In order to produce an interference pattern on the samples, a



specific beam path must be assembled, as seen in figure 3.1 for a two-beam interference pattern and in figure 3.2 for a three-beam interference pattern.

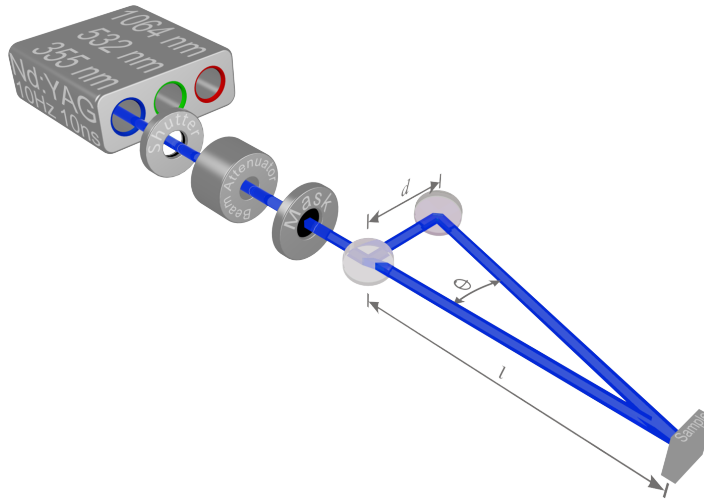


**Figure 3.1:** Representation of the laser beam path during two-beam interference patterning experiments.

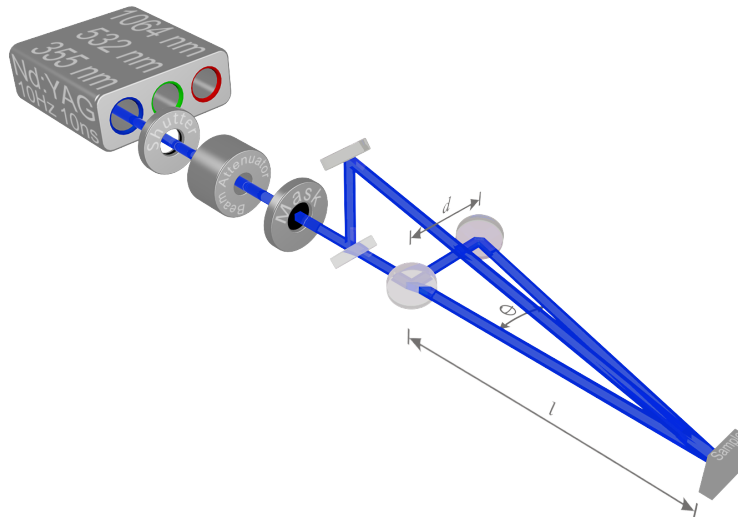


**Figure 3.2:** Representation of the laser beam path during three-beam interference patterning experiments.

Therefore, the primary laser beam is split into two or three sub-beams, depending on the type of interference pattern, via a 50/50 (two beams) or a 2/3 and a 50/50 (three beams) beam splitter(s) ( $45^\circ$ ). These sub-beams are then guided and focused by mirrors and lenses to interfere on the sample surface, resulting in a line-, dot- or lattice-like interference pattern (see more details in section 2.3). To avoid back reflexion at the different optical elements, anti-reflexion coatings are used. A variable attenuator, consisting in an optical assembly of a half-wave plate and two thin film polarisers, is also used to control the laser beam energy delivered from the primary beam. In order to control the interference pattern applied, two key parameters were tuned during the laser experiments: the energy  $E$  of one pulse and the interference period  $P$ . The specific amount of energy (Gaussian distribution) is controlled through the variable attenuator and monitored with a power meter (Power Max PM30V1) and the magnitude of the period can be modified according to equation 2.14, by changing the angle between the incoming beams at a constant wavelength. Experimentally, the distances  $d$  and  $l$  are adjusted to obtain the desired period. The number of pulses was kept constant to single pulse irradiation.

An overview of the parameters used to pattern the different samples in this work is given in table 3.1 below.

Chapter	Sample	$E$ [mJ/cm <sup>2</sup> ]	Thickness [nm]	P [ $\mu$ m]
4 / 5	Ti/Pt	220 - 859	15/300	4 - 7
	Ti/Au	360 - 636		
	Ti/Cu	340		
	Ti/W	420-710		
6	$Cu_3N$	247	550	5
	$Pd_{0.25}Pt_{0.75}O_x$	132	350	
7	Au-YSZ	91	140	5, 15

**Table 3.1:** Summary of samples and laser parameters used in this work.

## 3.3 Topographic and microstructural characterization

### 3.3.1 White light interferometry

The topographic characterization of the samples was realized using a white light interferometer (WLI, New View 200, Zygo), equipped with a 40x Mirau interference objective. Based on Michelson's interferometer, this optical surface profiler allows the measurement of structure depth and period with a vertical resolution smaller than 1 nm.

Additionally, in chapter 7, this technique was also used to gather surface roughness parameters of the patterned samples. Abbott-Firestone curves were obtained from the data analyzed with the software Metro Pro. These curves simulate the effect of wear on a bearing surface, representing the depth below a reference level parallel to a solid surface (ordinate) versus the percent bearing area intercepted by a horizontal line at that depth (abscissa). Mathematically, it is the cumulative probability density function of the height of the surface profile and can be calculated by integrating the profile trace. Skewness ( $R_{sk}$ ) and kurtosis ( $R_{ku}$ ) were deduced from the Abbott-Firestone curves.  $R_{sk}$  is a measure of symmetry of the surface profile around the mean line. Negative skew indicates a predominance of valleys, while positive skew indicates a "peaky" surface. A bearing surface should thus exhibit a negative skew.  $R_{sk}$  is defined as:  $\mathbf{R}_{sk} = \frac{1}{n(\mathbf{R}_q)^3} \sum_{i=1}^n \mathbf{Y}_i^3$ , where  $Y_i$  represents the heights of the profile and  $R_q$  the root-mean-square roughness (rms). The kurtosis  $R_{ku}$  is given by:  $\mathbf{R}_{sk} = \frac{1}{n(\mathbf{R}_q)^4} \sum_{i=1}^n \mathbf{Y}_i^4$ .  $R_{ku}$  is a measure of the randomness of heights, and the sharpness of a surface. A perfectly random surface has a value of 3; the greater the difference with 3, the less random and more repetitive the surface is. Surfaces with spikes have higher values; bumpy surfaces exhibit lower values.

### 3.3.2 Focused ion beam: dual beam workstation

The films were imaged with a high-resolution scanning electron microscope (SEM) equipped with a field emission gun combined with a focused ion beam (FIB, FEI Strata DB 235) at 5 kV acceleration voltage. Energy-dispersive X-ray spectroscopy (EDS) line scans were carried out in chapter 6 through several interference lines of the patterned films and on the sample surface of as-deposited films using a Si(Li) detector (EDAX) at 10 kV acceleration voltage.

### 3.3.3 X-ray diffraction

Grazing incidence X-ray diffraction analysis has been performed using a Philips Panalytical X'pert MRD/MPD 7 axe diffractometer. A  $Cu - K\alpha$  radiation X-ray source ( $\lambda = 0.154056$  nm) was used at a  $1^\circ$  incidence angle, operated in line focus mode with an acceleration voltage of 40 kV and a tube current of 40 mA. Only the phase analysis of as-deposited  $Pd_{0.25}Pt_{0.75}O_x$  in chapter 6 was performed using a CPS120 INEL diffractometer with a  $Co - K\alpha$  radiation X-ray source ( $\lambda = 0.178897$  nm) at  $4^\circ$  incidence angle, operated at an acceleration voltage of 35 kV and a tube current of 25 mA. The obtained diffraction patterns were evaluated using the data from the International Centre for Diffraction Data (ICDD).

### 3.3.4 Transmission electron microscopy

Transmission electron microscopy (TEM) lamellae of the patterned films were prepared by FIB milling [62] to provide further details as to their morphology and microstructure. The thin foils were then analyzed within a CM200 Philips microscope. Scanning transmission electron microscopy (STEM) observations have also been carried out within the FIB equipment.

### 3.3.5 Electron backscattered diffraction

In chapter 4, texture and grain-size distributions of the films were analyzed using electron backscattered diffraction (EBSD) within the FIB. The com-

plete automatic analysis of the resulting Kikuchi patterns was done using the OIM Software (TSL) at an acceleration voltage of 20 kV and recorded by means of a DigiView camera system. To produce a crystallographic orientation map, the electron beam is scanned over a selected area and the resulting Kikuchi patterns are indexed and analyzed automatically. The results of the EBSD measurements are presented in form of inverse pole figure maps (IPF), with the corresponding pole figures (PF).

## 3.4 Evaluation of material properties

### 3.4.1 Hardness

A TriboIndenter (Hysitron Inc., Minneapolis, MN) Nanomechanical Testing System was used to perform the nanoindentation tests performed in chapter 4. The diamond indenter in this system served as both the indenter and the imaging probe. Thereby, it is possible to locate the tailored structures with nanometre resolution while indenting the substrate. The peak load of 200  $\mu\text{N}$  was selected to limit the indentation depth at 10 % of the total 300 nm film thickness (indentation depth: 25 nm for Ti/Pt and 30 nm for Ti/Cu). This ensures that the measurements are neither affected by the geometry of the structured surface nor by the substrate. A Berkovich (three-sided pyramidal tip,  $142.3^\circ$ ) diamond indenter was used and carefully calibrated for its area function on standard material. Using the calculation method developed by Oliver and Pharr [63], local determination of both the hardness ( $H$ ) and the Young modulus ( $E$ ) have been carried out.

### 3.4.2 Electrical resistivity

The four-point probe method was applied to measure the electrical resistivity of the films, as reported in chapter 6. A Keithley 2700 multimeter and a Keithley 237 high-voltage source were used. All four gold-plated CuBe probes were positioned in a line with a uniform spacing  $S$  of 1 mm and are supported by springs on the other end of the probe head. The current was

applied stepwise from  $-0.1$  A to  $0.1$  A with  $0.001$  A increments. Thin films thicknesses  $d \ll \frac{S}{2}$  can generally be considered as semi-infinite, their sheet resistivity described by [64]:

$$\rho = \frac{\pi d}{\ln 2} \frac{V}{I} \simeq 4.532 \cdot d \cdot \frac{V}{I} \quad (3.1)$$

In this formula,  $V$  corresponds to the measured induced voltage drop (in the two inner probes) due to an applied current  $I$  (in the two outer probes). This sheet resistivity is only a measurement of the average resistivity over the thickness of an ideal semi-infinite sample (usually a thin square sample).

### **3.4.3 Friction coefficient**

Friction coefficients ( $\mu$ ) have been measured using a ball-on-disk nanotribo-meter (CSM Instruments). Each test presented in chapter 7 has been repeated at least 5 times in different regions to ensure reproducibility. Tests have been performed in linear reciprocating mode with an alumina ball ( $\varnothing = 1.5$  mm). Constant normal load ( $F_n = 1$  mN) to avoid substrate effect, half amplitude (0.2 mm), number of laps (100 cycles) and linear velocity (0.5 mm/s) have been applied in air at room temperature (25 °C) and relative humidity above 50 %.

## Chapter 4

# Local modifications of the morphology and the microstructure\*

**ABSTRACT:** The physical and chemical properties of materials are strongly correlated with their microstructure. Much effort is invested in the microstructure design of metallic thin films and the detailed understanding of dependencies, such as the impact of thermal annealing on the corresponding grain and microtexture characteristics. Laser Interference Metallurgy has been developed to locally and periodically modify the microstructure as well as the mechanical properties of thin films. The main focus of this chapter is the microstructural design of periodic arrays in pure metallic thin films. The possibility of controlling the (re)crystallization process by adjusting the laser energy density is demonstrated. Dynamic aspects of the induced (re)crystallization process such as temperature distribution were also studied based on thermal simulations. The texture and grain size distribution were studied by Electron Backscattered Diffraction. This reveals a preferred orientation of the micro-grains, which grow following the thermal gradient induced during laser irradiation. The influence of the laser radiation on the mechanical properties was also studied by nanoindentation.

---

\*Partially published in R. Catrin et al. *Adv. Eng. Mat.* **10**(5):466-470, 2008 [21] and in C. Gachot, R. Catrin et al. *Appl. Surf. Sci.* **255**(10):5626-5632 [22].

## 4.1 Introduction

Interfering beams from a high-power pulsed laser allows a direct lateral treatment to the surface microstructure of metals on the micro/nano-scale based on photo-thermal mechanisms [54]. Laser Interference Metallurgy (LIMET) allows the formation of periodic patterns with a well-defined long-range order on metallic surfaces at the length scale of typical microstructures (from sub- $\mu\text{m}$  to several micrometers) [23, 25, 55]. This recently developed technology takes advantage of the large area periodicity of interference fields produced by several coherent laser beams stimulating different metallurgical processes with a long-range order, such as melting, (re)crystallization, recovery, topography, defect and phase formation. Moreover, this kind of microstructure design also allows the tailoring of materials properties by obtaining the desired property at the desired location. Thus, the obtained combination of nano- and micro-scaled grain-sizes leads to periodic and well-defined arrays, exhibiting enhanced mechanical properties, like hardness or yield strength [65, 66]. Various examples demonstrate the versatility of this technique for unique surface architectures and controlled properties in friction and wear [67–70] or thermo-electrical applications in microelectromechanical systems (MEMS). In this context, the control of grain-size distributions as well as grain orientations in metals plays an important role in the localized optimization of physical properties. It is well known that the hardness and fracture toughness of polycrystalline materials are strongly correlated by the Hall-Petch law [1]. Thus, the combination of a periodic distribution of nano- and microcrystalline or ultra-fine-grained regions in a composite architecture provides high strength and ductility, in other words, high fracture toughness. Additionally, LIMET requires one single preparation step whereas other structuring techniques comprise at least two different steps (holography, irradiation, etching, etc) [56]. Moreover, no masks are required and relatively large areas up to the  $\text{cm}^2$  range depending on materials properties can be directly structured during each single irradiation pulse. In this chapter, a detailed study of the crystallization scenarios in different metallic thin films showing significantly varying melting temperatures are presented with a focus on the grain mor-



phology and microtexture. A combination of the results with finite element simulation contribute to the elucidation of the observable mechanisms.

## 4.2 Results and discussion

### 4.2.1 Microstructural design of advanced architectures

Different microstructural architectures were fabricated in Ti/Pt and Ti/Au films using single laser pulse interference experiments. Figure 4.1 shows three different types of periodic patterns produced in Ti/Pt films using the two- (figures 4.1.a and 4.1.e) and three-beam laser configuration (figure 4.1.b). As described in chapter 3, two interfering laser beams permit the fabrication of a line-like periodic pattern whereas the superposition of three laser beams results in a dot-like pattern. In figure 4.1.b, three different morphologies can be identified. Region 1 corresponds to the as-deposited (nearly unaffected) surface at the interference minima positions, exhibiting a nano-grained structure with grain sizes in the 15 – 25 nm range. In region 2, a fine-grained microstructure is observed ( $\approx 90$  nm), whereas in region 3 large  $\approx 800$  nm grains perpendicular to the interference fringes can be found (*i.e.* interference maxima regions). The formation of large grains at the interference maxima positions in such a preferred growth direction results from the local melting and posterior re-solidification of the film and is basically initiated by the temperature gradient developing perpendicular to the interference fringes. This phenomenon is known as Super Lateral Growth (SLG) [6, 8, 71]. Above a given laser fluence, laterally growing grains appear in this regime, originating from the unmelted areas (interference minima) and propagating to the completely molten regions (interference maxima). In figures 4.1.a and 4.1.b, a centre-line at the interference maxima can be observed, which results from the lateral growth of the grains from both sides of the molten pool at the interference maxima following the temperature gradient. Additionally, if the sample is rotated  $90^\circ$  and re-irradiated after the first laser pulse, a lattice-like pattern is fabricated, as shown in figure 4.1.e.

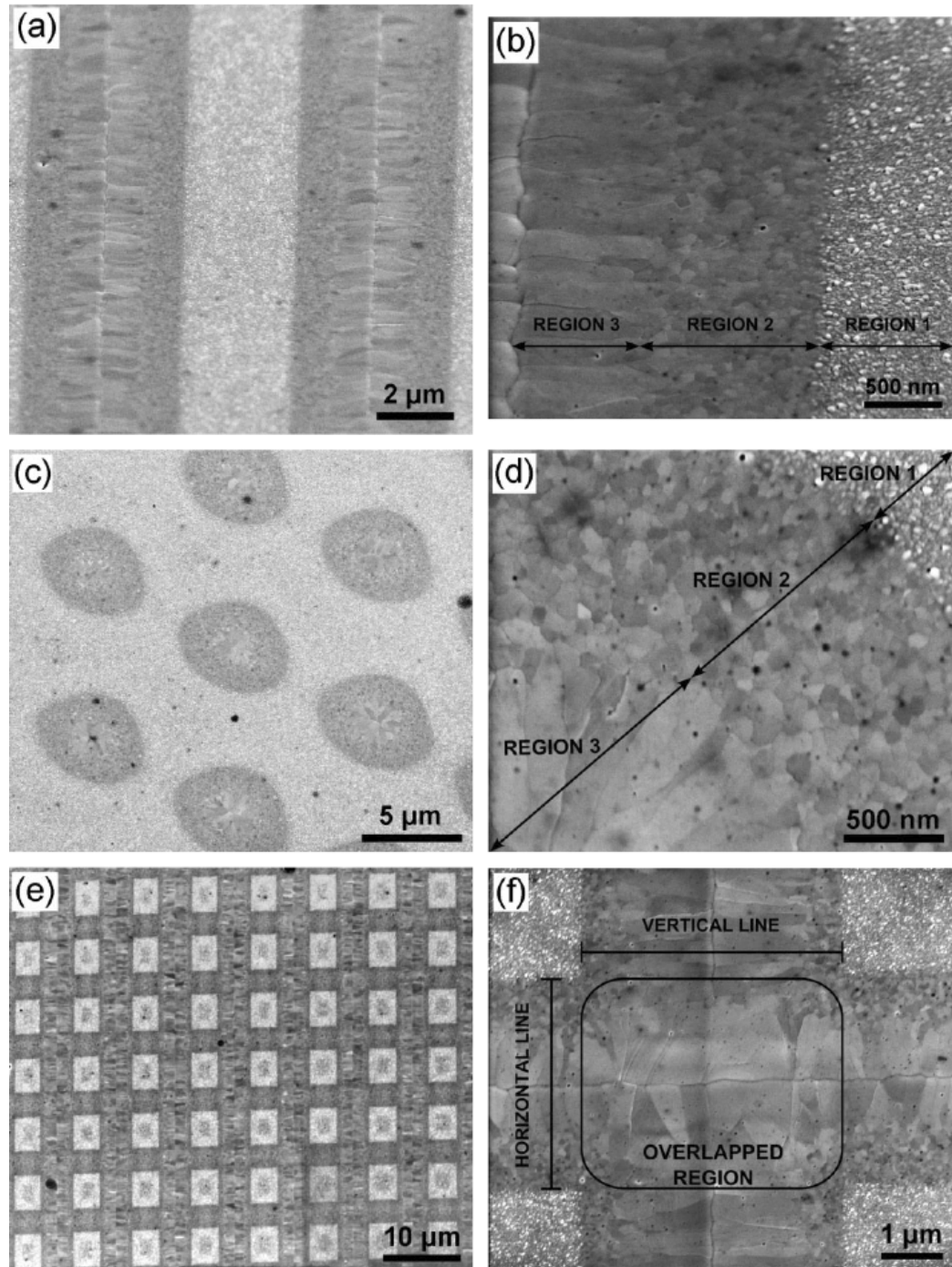


**Figure 4.1:** Laser-induced crystallisation in Ti/Pt thin films. (a, b) line-like pattern ( $F = 476 \text{ mJ/cm}^2$ ) indicating three different regions (nanocrystalline: region 1, fine-grained: region 2 and microcrystalline: region 3); (c, d) dot-like pattern ( $F = 859 \text{ mJ/cm}^2$ ) with the grains radially distributed (region 3); (e, f) lattice-like pattern ( $F = 709 \text{ mJ/cm}^2$ ). Reprinted from [21]

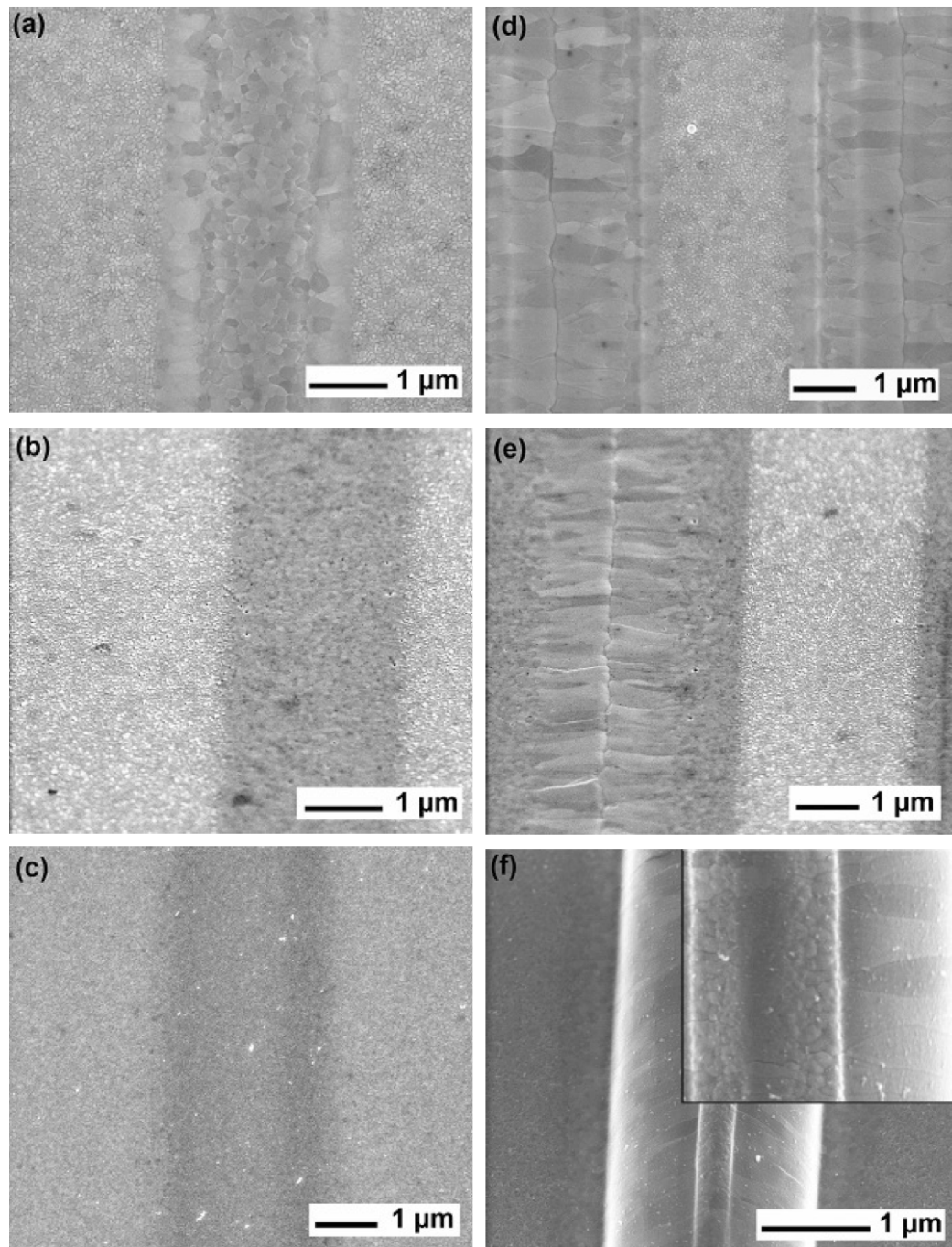
Due to the melting procedure applied twice to the metallic film, a different grain morphology with larger grains preferably oriented along the temperature gradient induced by the second pulse is observed (see figure 4.1.f at the overlapping regions of the lattice-like pattern). In the case of the dot-like structure, generated with the three laser beam configuration (figure 4.1.c), the grains grow radially towards the centre of the dots, also following the induced thermal gradient. According to the results reported on the previous configuration, three regions differing in microstructure can be observed, as shown in figure 4.1.d. These results show the possibility of fabricating different periodic arrays with well defined grain architectures under controlled laser parameters, such as laser fluence, pulse number and period.

Depending on the used energy density and the material, significant differences in the crystallization behaviour of the films can be observed. The results indicate basically three principal energy density regimes:

1. Partial melting of the films by low laser fluences,
2. Complete melting of the metallic layers for relatively high laser fluences,
3. Super Lateral Growth: crystallization scenario located between the partial and the complete melting process [6, 17, 50].

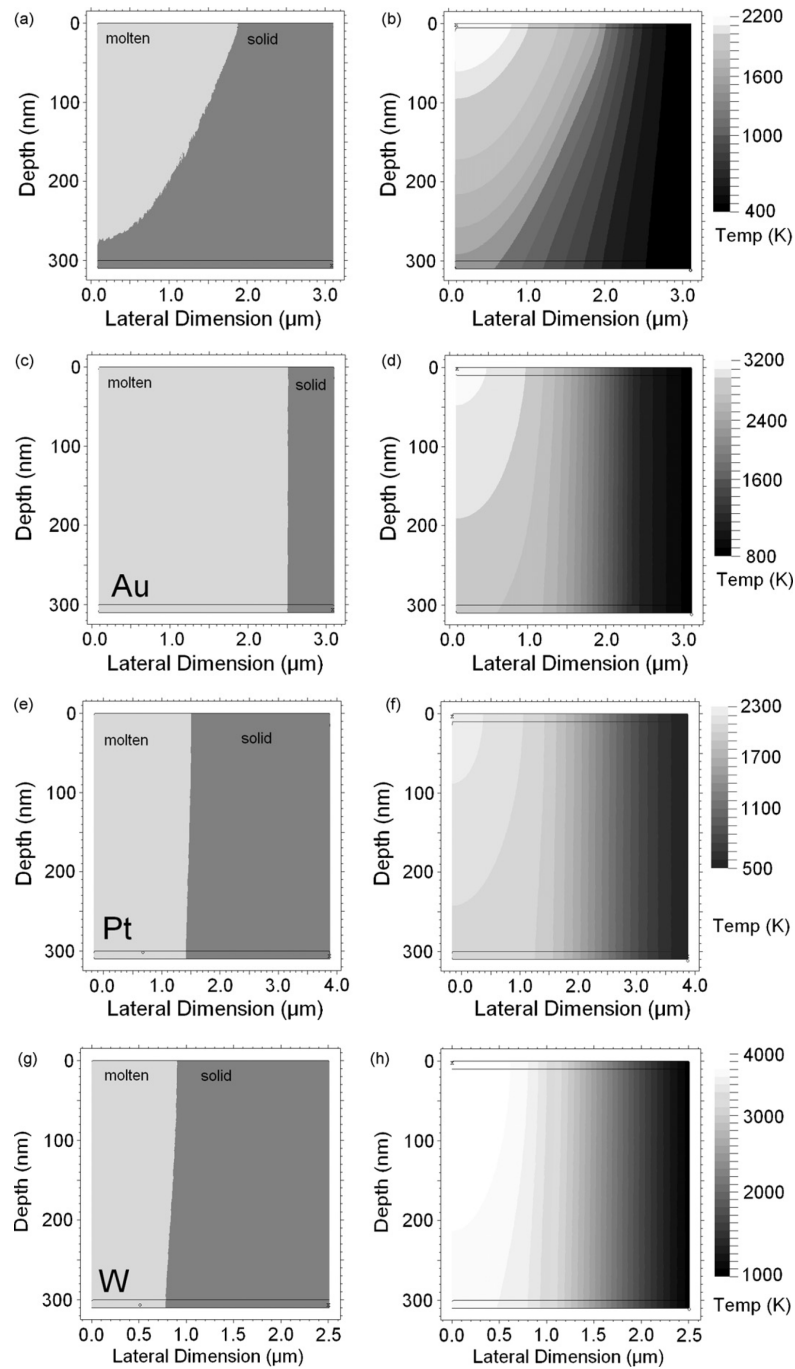
To illustrate the differences in these three energy density regimes, metallic samples (Ti/Au, Ti/Pt, and Ti/W) were irradiated and the morphological influences are summarized in the SEM micrograph of figure 4.2. The left (a, b, and c) and right (d, e, and f) rows denote the low and high fluence regimes, respectively. In order to understand the different morphologies of the irradiated samples, we performed two dimensional (2D) finite element numerical simulations. The simulations yield the time and spatial distribution of the solid-liquid interface during the exposure of the metallic samples to the interference patterns and are based on the heat diffusion equation. Further information about the model can be found in [72].

Figure 4.2.a represents the partial melting in a 300 nm thick Ti/Au film. Cross sections performed with a focused ion beam (FIB) verified that the



**Figure 4.2:** Morphology of irradiated Ti/Au, Ti/Pt and Ti/W films at different laser fluences. Left (a, b, and c) and right (d, e, and f) rows denote the low and the high fluence regimes, respectively. (a, d) Ti/Au,  $F = 360,636 \text{ mJ/cm}^2$ , (b, e) Ti/Pt,  $F = 220,535 \text{ mJ/cm}^2$ , (c, f) Ti/W,  $F = 420,710 \text{ mJ/cm}^2$ . Reprinted from [22]

film was not molten over the entire thickness. The same result was obtained using the thermal simulations as shown in figure 4.3.a. In addition, the calculated temperatures at the interference maxima and minima positions were 2200 K and 450 K, respectively (figure 4.2.b). Although the quenching rates during the laser irradiation can reach values of up to  $10^{10}$  K/s [54], the microstructure does not consist of very small grains in that case. During the vertical resolidification process, grains with typical sizes in the range of the film thickness appear. The vertical regrowth is triggered by a thin Au layer remaining in the solid state. A grain coarsening in the laser intensity maximum can be unambiguously identified. On the other hand, both the Ti/Pt (figure 4.2.b) and Ti/W films (figure 4.2.c) do not reveal such a distinct grain growth. Especially the Ti/W thin films seem to be nearly unaffected by the laser treatment. Obviously, the used energy density was not high enough to induce a considerable grain growth compared to gold. This can be mainly attributed to the low melting point of Au ( $\approx 1337$  K) in comparison to Pt ( $\approx 2045$  K) and W ( $\approx 3695$  K). In contrast, a deviating crystallization mechanism can be seen in figures 4.2.d-f. A so called Super Lateral Growth appears. In a very narrow processing window, in which the films are nearly completely molten, needle shaped grains are growing from unmolten regions (laser intensity minima) towards the molten laser interference maxima positions. This situation is illustrated in figure 4.3, where the temperature distribution for the three studied systems, together with the two-dimensional information about the phase (liquid or solid) of the metallic layers is shown. As can be seen in the figure, the temperature gradient (figures 4.3.c, 4.3.e and 4.3.g) is parallel to the film surface, which means that the recrystallization front is perpendicular to the film surface. Moreover, the adjacent unmolten areas act as heterogeneous nucleation sites for the laterally growing grains. These grains are subsequently impinging with one another forming a clear centre line. The maximum extent to which the grains are able to grow depends strongly on the energy density, the pattern period as well as the substrate temperature [6]. In our case, the substrates were not heated. According to the thermal simulations, the temperature differences between the interference maxima and minima are about 2400 K, 1800 K and



**Figure 4.3:** Thermal simulation of irradiated Ti/Au at low (a, b) and high (c, d) fluence regimes, Ti/Pt and Ti/W. In (a, c, e, g) the liquid-solid interface is shown during the resolidification process. The thermal gradient over the film cross-section, starting from the centre of a laser intensity maximum position is shown in (b, d, f, h). See in figure 4.2 for laser fluences. *Reprinted from [22]*

3000 K for Ti/Au, Ti/Pt and Ti/W at laser fluences of 636 mJ/cm<sup>2</sup>, 535 mJ/cm<sup>2</sup> and 710 mJ/cm<sup>2</sup>, respectively (figures 4.3.d, 4.3.f and 4.3.g). A more detailed look at the magnified insert of figure 4.2.f for the Ti/W film demonstrates that the lateral grains do not proceed to the centre of the laser intensity maximum. Round shaped grains in the middle of this region arise due to the deep supercooling and spontaneous nucleation of the film. A large periodicity or low laser fluence can facilitate this nucleation. The pattern period in this case was 5 μm. In order to avoid the spontaneous nucleation, the width of the intensity maxima regions must be narrow enough and the thermal gradient sufficiently high. Apart from that, the Ti/Au and particularly the Ti/W films show a strong topography. Generally, a surface tension gradient caused by temperature differences in adjacent areas induces a material flow from the warmer to the cooler regions which is known as the Marangoni effect [73]. The Marangoni instabilities depend mainly on two time scales: the thermo-capillary and the diffusive time scale [74–76]. The thermocapillary flow leads to the already mentioned material transport from the laser intensity maximum to the intensity minimum. As opposed to this effect, the diffusive mechanism tries to stabilize the film resulting in two competitive processes. It remains unclear which of the main factors influence or promote the respective mechanism. Due to the fact that the laser irradiation of the samples was performed under ambient conditions, a possible explanation could be the influence of adsorbates or oxide layers on the surface of the irradiated samples. These adsorbates could also promote the spontaneous nucleation of the film at the central area (figure 4.2.f). Laser experiments under a protective atmosphere (Argon or vacuum) should enable the verification of this hypothesis.

## 4.2.2 Long-range ordered architectures of grain sizes and orientations

In order to study the influence of laser radiation on the microstructure of metallic films under Super Lateral Growth regime, grain sizes and particularly texture states were determined in the Ti/Pt films previously characterized (see figure 4.1) by means of Electron Backscattered Diffraction (EBSD). Figure 4.4.a shows the grain size distribution of the lattice-like pattern, represented in figure 4.4.b (grain size map). Three different peaks can be well distinguished, which are related to a specific microstructure. In the as-deposited region, the grain-size is too low to be indexed by EBSD, as the corresponding values are below the resolution of the measurement equipment (resolution of 30 nm). In the vertical and horizontal lines, which were molten once (see in 4.1.f), the grain-size distribution is between 0.4  $\mu\text{m}$  and 1  $\mu\text{m}$  with a maximum centered at 0.8  $\mu\text{m}$ . On the other hand, at the regions where the Ti/Pt bilayer was molten twice (i.e. at the lattice-like structure, see interrupted line square in figure 4.5.c below), the grain size increases up to  $\approx 2 \mu\text{m}$  (figure 4.4.a).

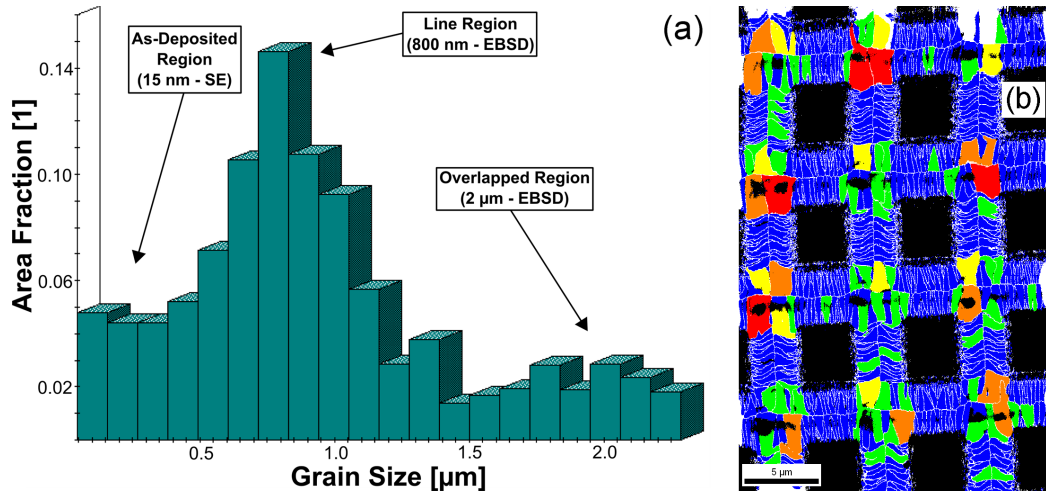


**Figure 4.4:** Grain-size distribution performed in lattice-like patterned Ti/Pt thin films. The grain-size distribution (a) reveals the grain-size difference between the overlapped region and the vertical and horizontal lines, evaluated from the grain size map (b). The black regions in the corners of (b) describe the nano grains from the as-deposited region, where no indexing is possible (i.e. below the EBSD detector resolution).



This result demonstrates that the formation of different film morphologies can be obtained by controlling the number of incident laser pulses (see in figure 4.1.f). The grain orientation of the irradiated Ti/Pt thin films was analyzed using Electron Backscatter Diffraction. Figure 4.5 shows both the Pole Figure map (PF) and the Inverse Pole Figure map (IPF) of a selected area of the lattice-like pattern, where the determination of the orientation of the crystal ensemble has been performed (figure 4.5.c). In the IPF map (figure 4.5.c), the predominant blue color indicates that the  $\langle 111 \rangle$  direction is the preferential one, as shown in the orientation triangle (corner in figure 4.5.c). At the interference maxima positions, illustrated by vertical and horizontal lines (excluding the overlapping zone due to the use of two subsequent laser pulses as described above), the grains are oriented perpendicularly to the interference lines. At these positions, the grain orientation analysis illustrated in figures 4.5.a and 4.5.b shows that the most frequent grain-growth direction is the  $\langle 110 \rangle$ . Texture analysis of the overlapped region reveals a  $\langle 111 \rangle$  direction, parallel to the normal of the sample (see PF in figures 4.5.a-b and 4.5.d). In order to get a more precise insight, the two domains at one interference maximum were cropped to perform texture analysis (see in figure 4.5.a-b). The results point out that a completely different texture apart from the global texture is observed. However, the texture analysis which corresponds to the overlapped region (see interrupted line square in figure 4.5.c), shows a (111)-fibre texture (figure 4.5.d). The same result was obtained using X-ray diffraction studies of the entire surface of the sample. Yet this result is observed due to the overlapping of different domains with specific orientations. Thus, global analyses performed using X-ray diffraction offer only limited insight into the local microstructure.

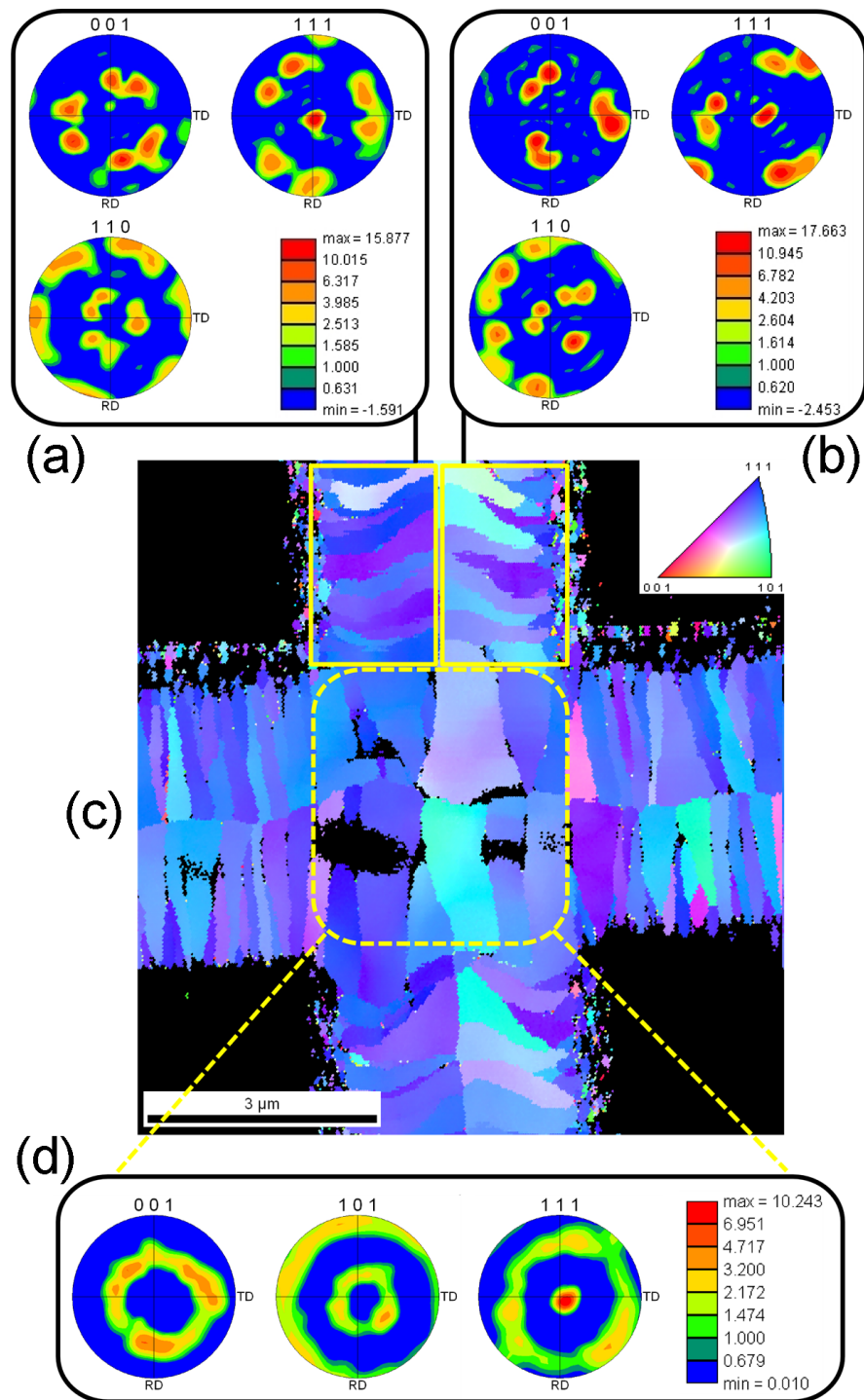


**Figure 4.5:** Texture analysis performed on lattice-like structured Ti/Pt thin films. Two kinds of measurements were performed in order to find the orientation of grains in the overlapped regions (c, d) and also in the vertical and horizontal regions (a, b). *Reprinted from [21]*

### 4.2.3 Mechanical composite effect

In order to reveal the mechanical behaviour of irradiated films and thus the possibility of creating a composite combination of soft/hard nanoscale grains and hard/soft microscale grains within laser interference patterning (LIP), nanoindentation tests were performed on Ti/Pt and Ti/Cu films. A nanoindenter was used for the experiment. Within this system, the diamond indenter served as both the indenter and the imaging probe. Thereby, it is possible to locate the tailored structures with a nanometre resolution while indenting the substrate. The experimental details are described in chapter 3).

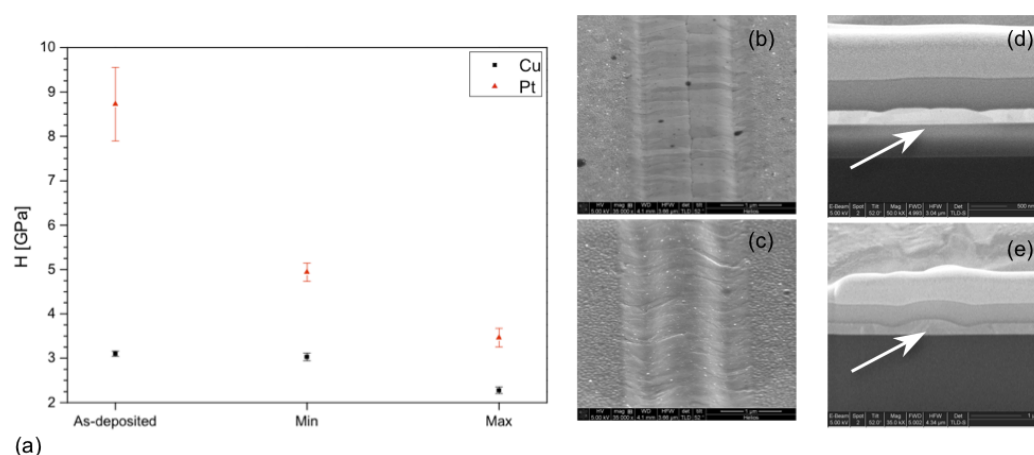


**Figure 4.6:** Nanoindentation tests on 300 nm Ti/Pt and Ti/Cu thin films. (a): The hardness measured ( $H$  in GPa) is plotted against the indent position, e.g. in as-deposited (non irradiated, nanocrystalline) zones, in interference minimum (nanocrystalline - nc) and maximum (microcrystalline - mc). (b) and (c): SEM micrographs of Ti/Pt and Ti/Cu, respectively, showing one mc maximum and two half nc minima. The determination of the hardness was carried out using the model of Oliver and Pharr [63]. (d) and (e): cross sections of Ti/Pt and Ti/Cu, respectively, showing in one mc maximum the total crystallization in the whole film thickness (see white arrows).

Figure 4.6.a presents the results obtained after five nanoindentations in each region: as-deposited, interference minimum (Min) and interference maximum (Max). In the Max regions, the indents were placed in one grain close to the centre line (impingement of the laterally growing grains), while in the Min regions, they were placed in the middle of the area. Figure 4.6.b and

4.6.c present the 52° tilted SEM micrographs of the indented films before being experimented. The microstructure obtained by laser interference irradiation reveals a high topography in the case of Ti/Cu and a smaller one for the Ti/Pt. Furthermore, two specific types of grain morphology are visible: a nanocrystalline zone (nc) in the interference minimum (small dots right and left) and a microcrystalline (mc) zone in the interference maximum. Figure 4.6.d and 4.6.e also show the microstructure in the film cross-sections, characterized by a crystallization in the whole film thickness. Moreover, comparing the two chosen materials reveals that nc-grains in Pt ( $\approx 25$  nm) are smaller than nc-grains in Cu ( $\approx 60$  nm). Confronting those morphological observations to the graph presented in figure 4.6.a, the following conclusions can be made:

1. Original as-deposited Pt grain-sizes are 2x smaller than that of Cu, which explains the general higher hardness of Pt in all three regions.

2. Introducing

$$\Delta H_{Ti/Pt} = H_{Ti/Pt}(Min) - H_{Ti/Pt}(Max)$$

$$\Delta H_{Ti/Cu} = H_{Ti/Cu}(Min) - H_{Ti/Cu}(Max)$$

where  $H_{Ti/Pt}(Min) = 4.94$  GPa,  $H_{Ti/Pt}(Max) = 3.46$  GPa,  $H_{Ti/Cu}(Min) = 3.03$  GPa and  $H_{Ti/Cu}(Max) = 2.28$  GPa, then  $\Delta H_{Ti/Pt} = 30\%$  and  $\Delta H_{Ti/Cu} = 25\%$ . The hardness difference in the fabricated composite between a minimum and maximum is in the same order of magnitude for the two films and thus seems not to depend on the material. The most influencing parameter here is the change in grain size regime between maxima and minima, which leads to the fabrication of a periodically organized composite material consisting of well-defined nano and microcrystalline grain arrays.

3. In the case of Ti/Pt, the hardness in the nc minimum zone ( $H_{Ti/Pt}(Min)$ ) is 43% lower than in the nc as-deposited state ( $H_{Ti/Pt}(As - dep.)$ ). This is not the case for Ti/Cu, for which  $H_{Ti/Cu}(Min)$  decreases only by 2%. This behaviour is mainly due to thermal effects appearing in the interference minima zones, as demonstrated in the thermal simulations in the

above section 4.2.1. First of all, in those “not cold” regions, the temperature reaches about 800 K, which is high enough to induce a smooth microstructural evolution in the interference minima regions, leading to larger nanocrystals than the original as-deposited nc-grains. However, in the case of Ti/Cu, the small difference between  $H_{Ti/Cu}(Min)$  and  $H_{Ti/Cu}(As - dep.)$  could be explained through weaker morphological evolutions in the interference minima due to enhanced thermal conductivity compared to Ti/Pt.

Still, the laser-induced topography created in the films at the interference maxima zones does not permit a clear dissociation from the induced microstructure. The manner in which those factors influence the measurements and further tribological tests is not trivial and has yet to be elucidated. The possibility of separating the contributions of microstructure and topography is difficult and should contribute to reveal the potential of the method.

### 4.3 Summary

In summary, it has been shown that Laser Interference Metallurgy is a powerful tool for the microstructural design of thin metallic films by fabricating periodic structures with tailored morphologies and microstructures in the nano and micrometer scale. This means a defined size and orientation of the grains with lateral periodicity. Different periodic architectures were fabricated using two and three interfering laser beams, leading to the creation of three different microstructures (*i.e.* nano-grained, fine grained and large-grained). Furthermore, it has been shown that such a microstructural architecture confers the film interesting mechanical properties in a mechanical composite. In addition, the thermal gradient induced in the film during the laser irradiation has been identified as a factor in the lateral growth direction and the preferred orientation of the grains. Subsequent laser pulses have been shown to further modify the grain size. This leads to overlapping regions with larger grain sizes, due to the second melting of the film. Finally, texture analyses have proven the corresponding impact on the microstruc-

ture and the anisotropy of the periodic structures. The size and scale of the tailored structures produced by this technique could be beneficial with regard to thermo-electrical as well as tribo-mechanical applications.

## Chapter 5

# Selective wet chemical etching of laser interference patterned films\*

**ABSTRACT:** The physical and chemical behaviour of materials is strongly correlated with their microstructure. Laser interference patterning is used to locally tune the grain architecture of metallic thin films by inducing a defined size and orientation of the grains with lateral periodicity. This technique enables the local nucleation and crystallization of amorphous or nanocrystalline metallic thin films, thus combining nano- and microcrystalline regions ordered in periodic line- or lattice-like arrangements in a composite architecture. After having locally modified the microstructure of e-beam evaporated Ti/Pt and Ti/Au films by laser irradiation, a wet chemical etching procedure was induced in hot aqua regia. A selective etching is achieved without the use of conventional lithography. The microcrystalline zones of specific oriented grains show a higher resistance against the wet chemical etchant than the as-deposited nanocrystalline areas which are completely removed down to the substrate. This procedure may be a low cost alternative approach to conventional lithographic techniques and provide a novel method for straight-forward patterning of metallic thin films.

---

\*Published in R. Catrin et al. *Proc. of SPIE* **7362**(736217):1-6, 2009 [38].

## 5.1 Introduction

Since the early 1980's, microelectromechanical systems (MEMS) predominantly refers to the fabrication of micromechanical parts for Si microsensors. The fabrication of such parts involved a selective directional etching process using etch masks in order to prevent specific Si substrate arrays from being etched [77]. As one of the main bulk micromachining technologies, this traditional anisotropic etching of silicon has been widely used in silicon sensors and actuators for a long time. However this lithographic technique includes several preparation steps, which have crucial consequences on processing time and productivity. Instead of preferentially etching the film after its deposition to fabricate a sensing film, Majoo et. al. [78] took advantage of microheating capabilities combined with Chemical Vapour Deposition (CVD) to achieve an alternative maskless selective deposition of sensing films over the heated zones. They actually incorporated conductance electrodes to locally heat the sensor platform and thus induce a preferred growth of the film in these regions. Nevertheless, this technique still involves numerous complicated steps, in particular for the preparation of microheaters prior to the selective film growth. To reduce the overall complexity, a solution consisting in directly modifying the microstructure of metallic thin films, tailoring their mechanical properties such as hardness and acting as preferential etching zones is hereby reported. Prior to a maskless etching, the electron beam deposited nano-grained films are periodically recrystallized using the interference principle of light with a nanosecond high power pulsed laser. The fabrication of a specific grain morphology leads to a rapid one-step wet selective material removal, which could be of interest for the low cost fabrication of micromachined devices.

## 5.2 Results and discussion

Here, the effect of a laser-induced selective wet chemical etching is reported by investigating the microstructures in Ti/Pt and Ti/Au film surfaces before and after etching. Before etching, all the samples were laser irradiated,



producing a specific periodic and well-defined microstructure and grain morphology, which are key factors to obtain a selective etching without using any lithography. The influence of annealing before etching is also suggested as outlook.

### **5.2.1 As-irradiated morphologies before etching**

Figure 5.1 shows the microstructure evolution of the e-beam deposited and laser-irradiated Ti/Pt (figures 5.1.a-b) and Ti/Au (figures 5.1.c-d) thin films. The laser parameters for structuring are detailed in the figure captions (see chapter 3 for more details). The as-deposited nano-grained morphology is characterized by grain sizes of about 20 nm for the Au and Pt surface metallization, determined by FIB measurements. Irradiating the films with superimposed laser beams results in periodic patterns, which are characterized by a lateral grain growth with typical dimensions of  $\sim 800$  nm in the area of the laser interference maxima, alternated with untreated regions at the interference minima. This is known as super lateral growth [6, 8], more details have already been published elsewhere [21, 22] (see also section 2.2.3). In figures 5.1.a and 5.1.c, a centre line in the interference maxima positions can be observed. It results from the lateral grain growth originating from both sides of the molten pool that is generated from the high energetic pulse during the laser irradiation. In the case of Ti/Au (figure 5.1.c), the limit between the as-deposited zones and the lateral recrystallized zones presents a particular morphology characterized by globular grains, which is absent in the Ti/Pt irradiated films. Those round-shaped grains arise due to the deep supercooling and spontaneous nucleation of the film. Figures 5.1.b and 5.1.d represent a lattice-like pattern resulting from a  $90^\circ$  sample rotation between two laser pulses. One can observe that in the overlapped regions, the grains grow further and are preferably oriented along the temperature gradient induced by the second pulse.

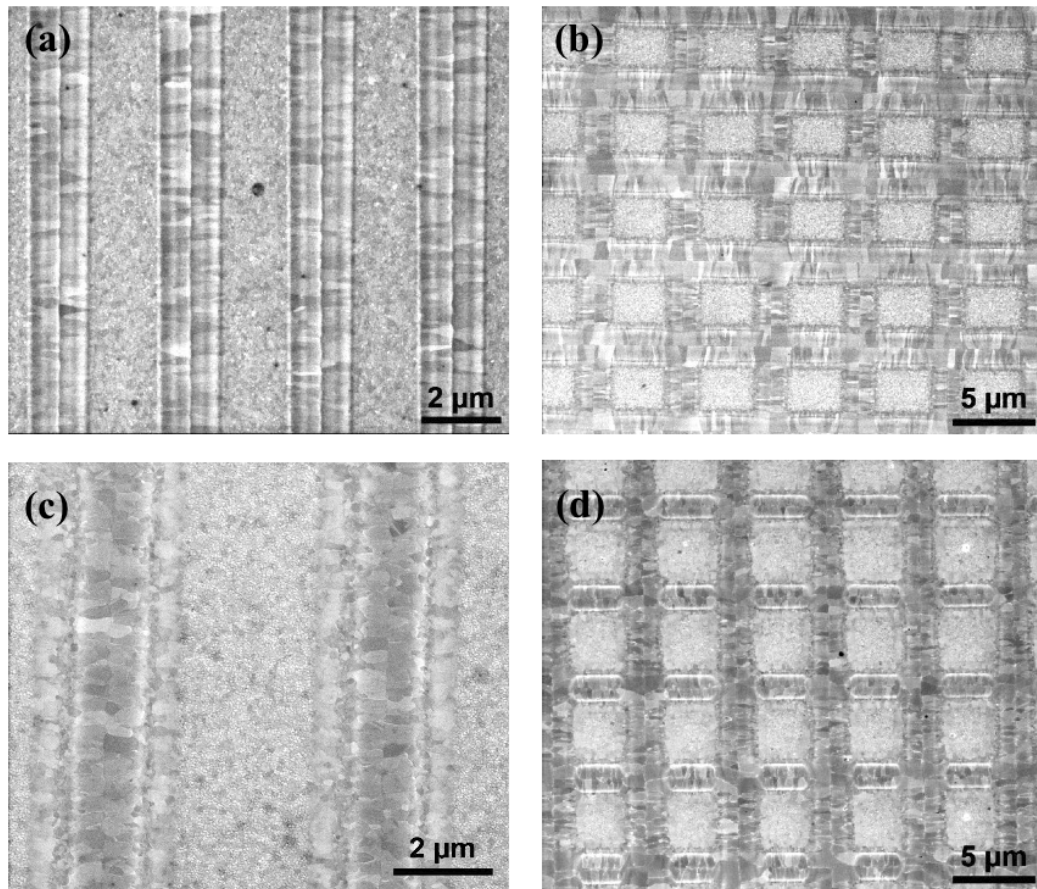


**Figure 5.1:** As-irradiated morphologies of Ti/Pt (a, b -  $600 \text{ mJ/cm}^2$ ) and Ti/Au (c, d -  $350 \text{ mJ/cm}^2$ ) obtained using laser interference patterning. Both of the films show a periodic laser induced recrystallization of the nano-grained as-deposited state. The grains are elongated and grow perpendicular to the interference fringes, following the temperature gradient initiated during the laser treatment. Additionally, a lattice-like pattern can be fabricated, rotating the sample  $90^\circ$  and irradiating a second time (b, d). Reprinted from [38]

## 5.2.2 Effect of chemical etching

The previously patterned Ti/Pt and Ti/Au films are now exposed to aqua regia for 3 min at 65 °C and 35 °C, respectively. The aim of the primary laser patterning was to create a morphological patterning that favours a selective wet chemical etching of the films without using etch-resist masks. Figures 5.2.a and 5.2.c illustrate the results of the selective etching procedure for line-like patterns in Ti/Pt and Ti/Au films, while figures 5.2.b and 5.2.d show those applied for the lattice-like patterned Ti/Pt and Ti/Au bilayers, respectively. The inserts at the upper right corner of figures 5.2.a-d are magnified zones of the micrographs that offer a detailed view of the etching effects and the corresponding microstructure. In both films, a selective etching of the films is obtained after exposure to aqua regia. In the case of the line-like patterns, the interference minima zones have been etched down to the Si or  $SiO_2$  surface, while leaving the lateral-grained interference maxima zones at the Ti/Au samples almost unaffected. In comparison, these areas are, in the case of Ti/Pt, substantially attacked. In addition, a thin layer of as-deposited Pt is still detectable in the interference minima zones, due to etching parameters, which could be adjusted more precisely. Figure 5.2.b presents the lattice-like pattern of the Ti/Pt samples, which exhibit a higher etch selectivity between the two regions, resulting in square-shaped islands of etched regions surrounded by metallic lines. For the Ti/Au film the situation is quite different, as the etchant has dissolved the gold film only in regions presenting a globular morphology (see figures 5.2.c-d). Both the as-deposited and the large-grained regions remain nearly unaffected by the etchant. Nevertheless, a well-defined etched line following the limit of the large grains of the interference maxima zone is produced, acting as a barrier between the two neighbouring regions.

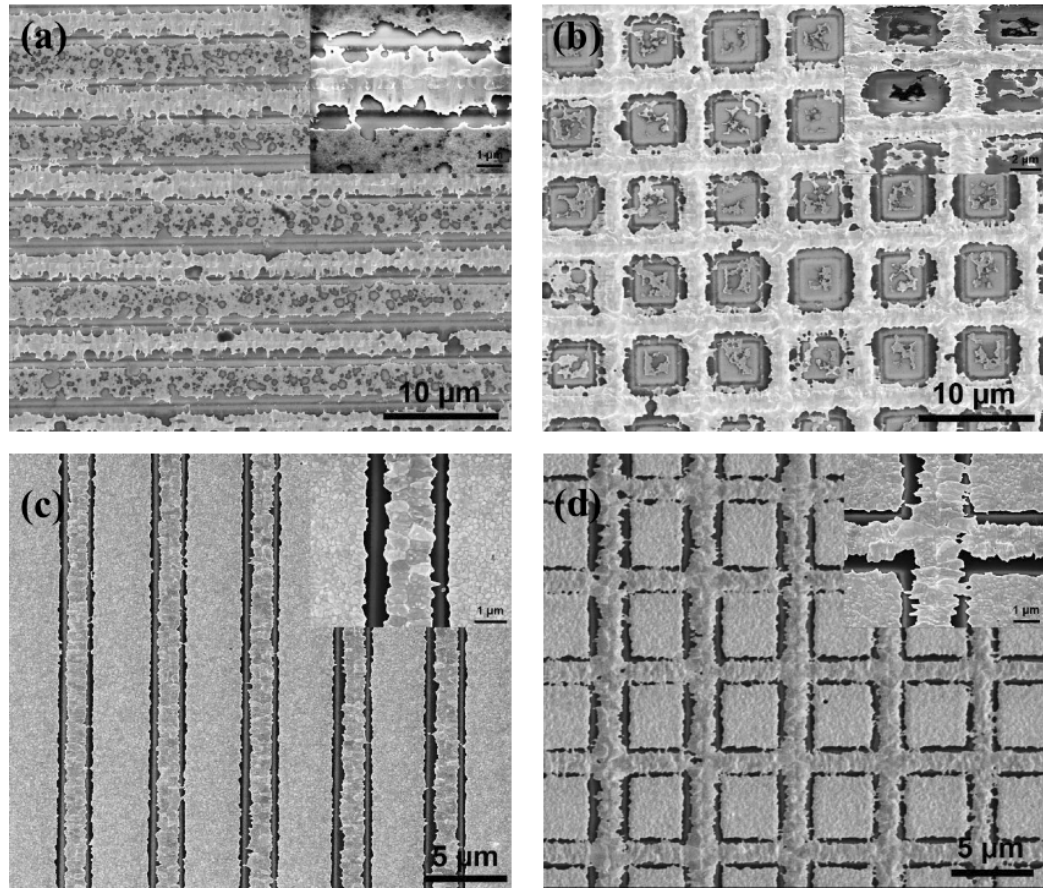


**Figure 5.2:** Effect of the wet chemical etching applied for both Ti/Pt and Ti/Au thin films. The Ti/Pt (a, b) was etched for 3 min at 65 °C and the Ti/Au (c, d) for 3 min at 35 °C. The different surface metallizations exhibit a selective etching with different etching behaviours. In the case of (a) and (b), the laser interference minima areas (as-deposited) have been etched, while for (c) and (d), these zones show no etching. The Au film is etched at the limit between the as-deposited region and the irradiated interference maxima zones. *Reprinted from [38]*

### 5.2.3 FIB cross section in Ti/Pt

The following cross section of a line in a large grained region of lattice-patterned Ti/Pt has been performed by FIB (see details in chapter 3) in order to investigate the etch attack of aqua regia in more detail. On the one hand, one can see in the deeper view of figure 5.3 that the as-deposited regions show a very good etch selectivity and only the laser-induced (re)crystallized

zones remain after the chemical attack. On the other hand, as soon as the as-deposited zones are quasi totally etched, the aqua regia can penetrate under the recrystallized Pt, etching the interface region between the Ti/Pt film and the substrate.

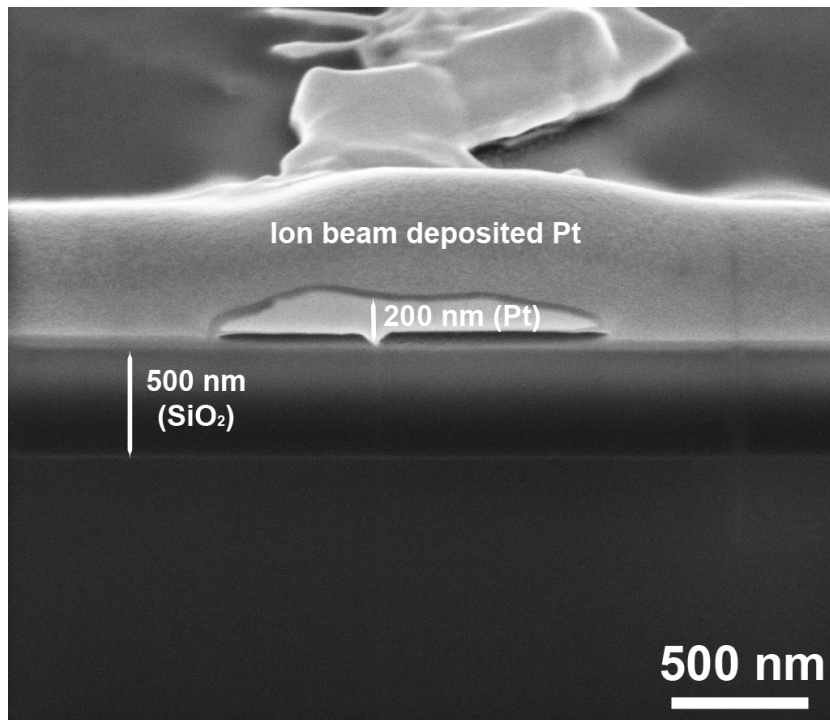


**Figure 5.3:** FIB cross section made in a (re)crystallized region of the line-like interference pattern in Ti/Pt after etching. Parallel to the unetched Pt recrystallized lines, an etching effect under the Pt line can also be observed. *Reprinted from [38]*

This demonstrates that further improvements in the irradiation and the etching procedure are necessary to minimize the material removal below the (re)crystallized regions. Moreover, measurements of the film thickness in the large-grained zone indicate that such zones show a material removal of 1/3 of the deposited film thickness, which is in good agreement with the creation of a local and selective wet chemical etching.

### 5.2.4 Effect of relaxation before etching

In order to get insight into the impact of thermal treatment, patterned un-etched Ti/Au films with satisfying etching performance, were annealed for 30 min at 120 °C in a vacuum furnace ( $1 \cdot 10^{-5}$  mbar) after laser patterning and before chemical etching in aqua regia for 3 min.

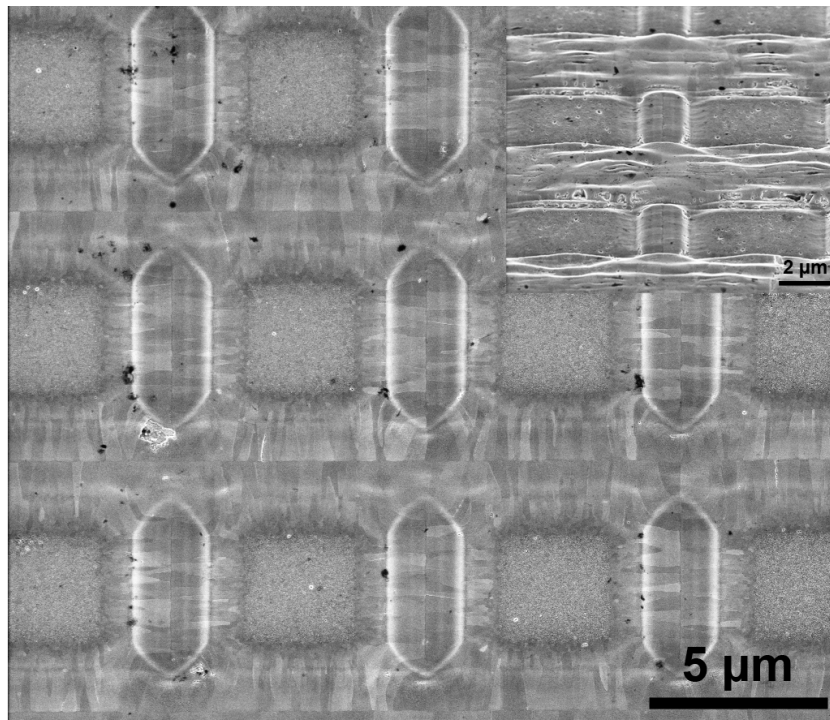


**Figure 5.4:** Morphology of Ti/Au after annealing in a vacuum furnace ( $1 \cdot 10^{-5}$  mbar) at 120 °C for 30 min and further applying the standard etching procedure described in the experimental part. After the relaxation of the film a further etching of the nano-grained zones is no longer observed as in figures 5.2.a and 5.2.b, but an increase in roughness of the (re)crystallized zones is visible. *Reprinted from [38]*

In figure 5.4, the effect of annealing on the etching procedure is depicted. The morphology strongly differs with that of figure 5.2 without pre-annealing. In contrast to figure 5.2.d, an attack of the globular grain zones located between the as-deposited and the large-grained area (see figure 5.4) is not detectable. The insert in figure 5.4 provides a 52° tilted view of the sample surface after etching. It reveals a predominant enhancement of the surface

roughness rather than a material removal. The pre-annealing procedure could induce a relaxation of residual stresses combined with a further increase in grain size, responsible for a slighter etching impact on the Ti/Au films.

### **5.3 Summary**

The effect of laser-induced tailoring of the grain morphology of Ti/Pt and Ti/Au thin films prior to a one-step selective wet chemical etching in hot aqua regia has been reported. Depending on the used systems, different etching behaviours have been observed, leading to a selective material removal either in the as-deposited regions (Ti/Pt), or in the zones between the interference minima and maxima (Ti/Au). Nevertheless additional investigations of the etch attack under the sample surface of Ti/Pt reveal a "sub-etching" that calls for a further refinement of the experimental conditions. Finally, a relaxation of the film in a vacuum furnace indicates higher resistance to the wet chemical etching procedure, increasing the surface roughness rather than leading to selective material removal.





## Chapter 6

# Laser-assisted chemical decomposition for electrical conductivity enhancement\*

**ABSTRACT:** Laser interference patterning (also known as Laser Interference Metallurgy) is used to locally tailor the microstructure of as-deposited oxide ( $Pd_{0.25}Pt_{0.75}O_x$ ) and nitride ( $Cu_3N$ ) thin films to induce chemical decomposition, responsible for a decrease in electrical resistivity. This results in a locally porous microstructure due to the simultaneous emission of gaseous nitrogen and oxygen. The process generates local metal precipitation of Pt or Cu in the oxide or nitride matrix at the nanometer scale. Thus, isolated metallic clusters with low resistivity coexist with a high resistivity phase, establishing a preferential electrical conduction path and giving the system a lower effective resistivity. The decomposition process is investigated by the four-point probe method, X-ray diffraction, spectrophotometry, white light interferometry, scanning and transmission electron microscopy.

---

\*Published in R. Catrin et al. *Appl. Surf. Sci.* **257**(12):5223-5229, 2011 [36] and in R. Catrin et al. *Mat. Res. Soc. Symp. Proc.* **1339**:mrss11-1339-s01-04, 2011 [35].

## 6.1 Introduction

Microstructural evolutions are directly responsible for effects on the physical, mechanical, electrical and also chemical behaviour of materials. *A fortiori* in the case of thin films, size effects may also lead to a more complex interpretation of the results and require more specific attention in their advanced microstructural design as well as the detailed understanding of dependencies on the material response. The thermal decomposition of metal oxide and nitride thin films can be exploited to generate original microstructures such as high specific surface area metal islands on an oxide matrix [79] or dispersed particles with different core and surface compositions [80]. Thereby, physico-chemical properties of the as-grown films are strongly impacted by thermal treatments. Copper nitride ( $Cu_3N$ ) is a metastable compound under normal conditions well known to decompose in the 100 – 470 °C range [81–84]. This compound can easily be formed in thin film form by reactive magnetron sputtering with physical properties highly depending on the nitrogen stoichiometry [85]. Palladium oxide ( $PdO$ ) and platinum oxide ( $PtO_2$ ) are stable in normal conditions but decompose in air around 850 °C [86] and 450 °C [87], respectively. Thus, the thermal decomposition of complex  $Pd_{1-y}Pt_yO_x$  thin films produced by physical vapour deposition methods [80], [88] is rather complex but is characterized for  $y \geq 0.4$  by the crystallization of metallic nanoparticles below 750 °C in a mixture of methane and oxygen [80, 88]. The interference principle of light from a high-energy nanosecond pulse laser source, so-called laser interference metallurgy [25] leads to a periodic thermal treatment with a local melting of the surface of the material. This one-step process allows a surface tailoring resulting in periodic structures organized in well-defined geometrical patterns and is hence expected to generate decomposition patterns in  $Cu_3N$  and  $Pd_{1-y}Pt_yO_x$ . In the present chapter, the influence of laser interference irradiation within nanosecond single pulses on the microstructure and electrical resistivity of  $Cu_3N$  and  $Pd_{0.25}Pt_{0.75}O_x$  thin films deposited by reactive magnetron sputtering is reported.

## 6.2 Results and discussion

### 6.2.1 Thermodynamics of the Pd-Pt-O system

The Gibbs energy of formation of a compound allows the evaluation of its stability in a given environment. Figure 6.1 displays the thermal evolution, under 1 bar of air, of the Gibbs energy of formation of  $PdO$  and  $PtO_2$ . Negative values indicate the thermodynamic stability of the compound; the magnitude indicates the reactivity of the metallic element towards oxygen. If thermodynamic equilibrium is reached, Pd and Pt elements should be oxidized within  $Pd_{0.25}Pt_{0.75}O_x$  films after deposition, thus Pt-O and Pd-O bonds should break around 500 °C and 850 °C, respectively (see in figure 6.1).

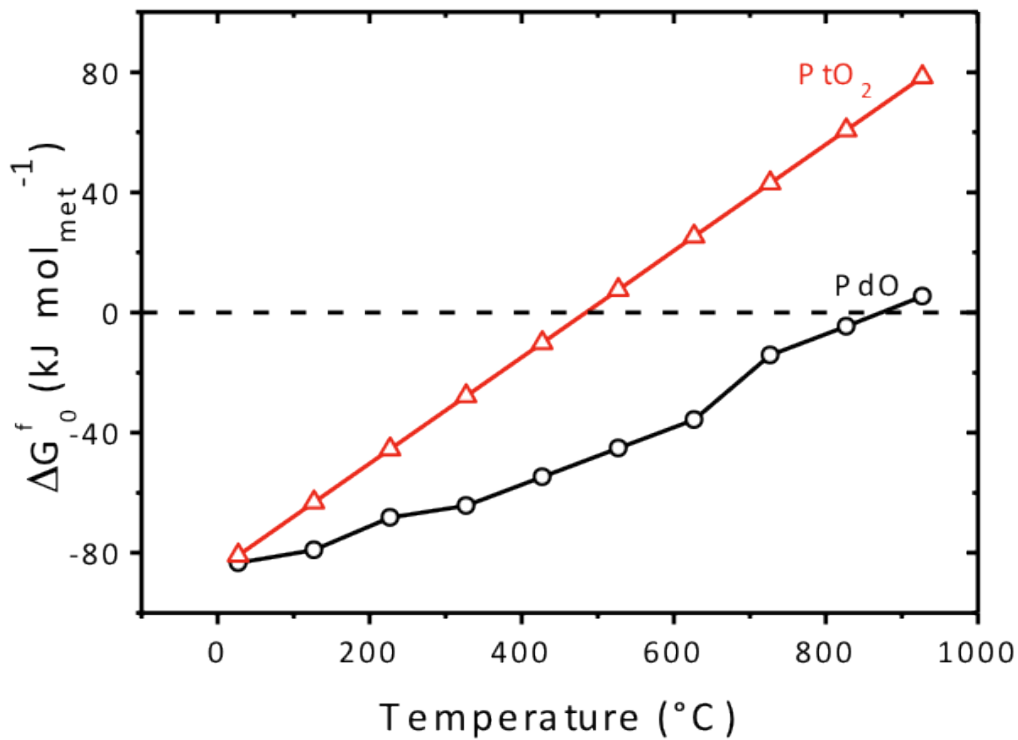


**Figure 6.1:** Thermal evolution, under 1 bar of air, of the Gibbs energy of formation of  $PdO$  and  $PtO_2$ . The values are given for 1 mol of metal. Reprinted from [35]

## 6.2.2 Morphological and topographical evolutions

Figure 6.2 shows the scanning electron micrographs of the nitride ( $Cu_3N$ ) and oxide ( $Pd_{0.25}Pt_{0.75}O_x$ ) thin films irradiated by single pulses within the laser interference system described in the experimental part.

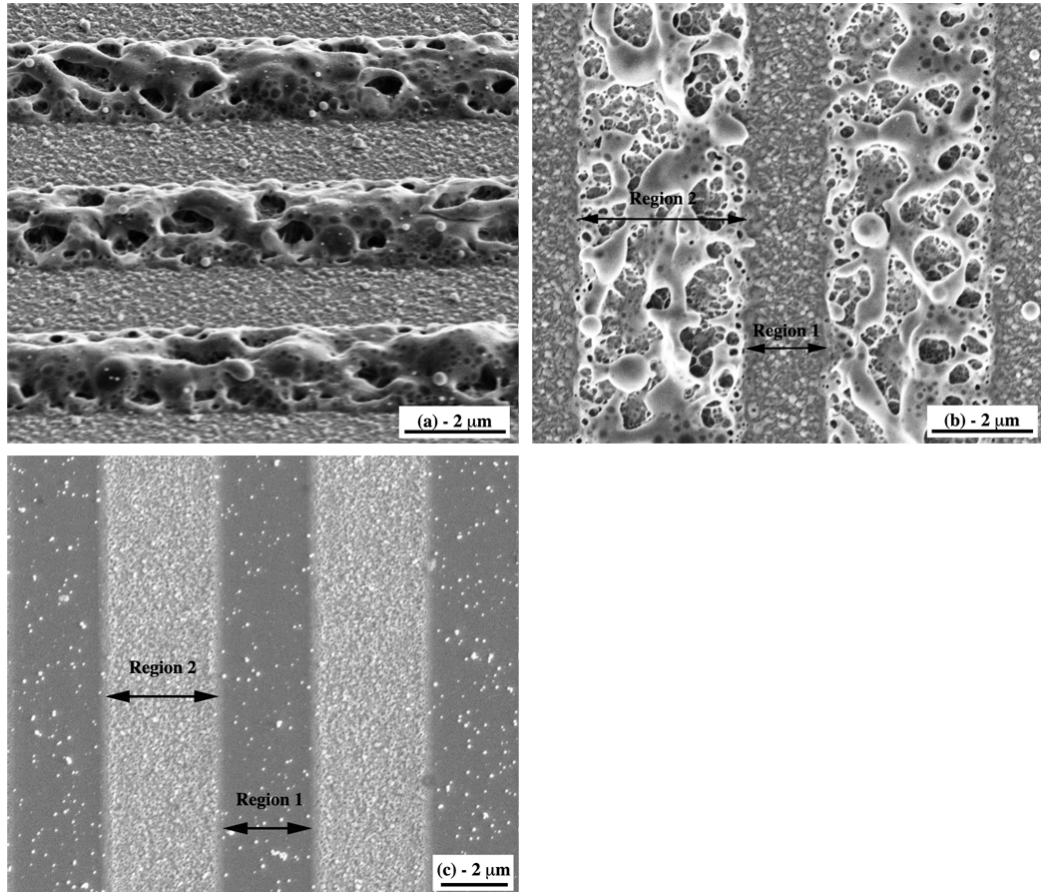


**Figure 6.2:** Morphological evolution of patterned  $Cu_3N$  (a, b) and  $Pd_{0.25}Pt_{0.75}O_x$  (c) observed by SEM. In (b) and (c), region 1 and region 2 correspond to the laser interference minimum (“untreated”) and maximum (porous and foamy), respectively. (c) is characterized by numerous tiny porous clusters. *Reprinted from [36]*

The 550 nm thick  $Cu_3N$  has been irradiated with a laser fluence  $F$  of 247 mJ/cm<sup>2</sup> and the 350 nm thick  $Pd_{0.25}Pt_{0.75}O_x$  with  $F = 132$  mJ/cm<sup>2</sup>. The line-like interference patterns result from the superposition of two individual laser beams. As shown in figure 6.2a-c, the surface morphology of

both films changes drastically after irradiation and consists of two different morphological regions as indicated in figures 6.2b and 6.2c. Region 1 corresponds to the zone of the interference minimum and region 2 to that of the interference maximum, each region having a period  $P$  of about  $5\ \mu\text{m}$ . Further detailed understanding of the laser-induced microstructure influences are detailed in chapter 4 and can also be found in [21, 22]. In figures 6.2a and 6.2b ( $\text{Cu}_3\text{N}$  system), an irregular porous and foamy structure can be observed in region 2, while region 1 exhibits a similar morphology to the as-deposited film. Closer observations of the as-deposited state and region 1 have shown a dense morphology characterized by crystals with an average diameter of approx.  $100\ \text{nm}$ . Region 2 in figure 6.2c ( $\text{Pd}_{0.25}\text{Pt}_{0.75}\text{O}_x$  system) is characterized by a rough surface, composed of many tiny white porous clusters which are, however, homogeneously distributed over the whole region 2. The latter are in some cases ejected onto region 1 during the interaction. Finite element simulations in pure metallic thin films have already demonstrated that the temperature can reach up to  $3000\ \text{K}$  in this region, with high quenching rates of up to  $10^{10}\ \text{K/s}$  [22, 25]. By observing the films under a white light interference microscope (WLI), surface profiles reveal their topography by providing the height as a function of the distance along an imaginary surface cross-section (see figure 6.3 below). For both films, the positive bulges correspond to the interference maxima (region 2) and the negative cavities to the interference minima (region 1). By comparing the two profiles, it is found that the porous and foamy structure in region 2 of  $\text{Cu}_3\text{N}$  (Fig. 2a) also gives the surface a heterogeneous interference pattern, with different patterning amplitudes along the surface cross-section. In contrast, the profile of  $\text{Pd}_{0.25}\text{Pt}_{0.75}\text{O}_x$  exhibits a homogeneous topography over the analyzed area. These observations correlate with the SEM micrographs of figure 6.2, which reveal, in region 2, a smoother microstructure for  $\text{Pd}_{0.25}\text{Pt}_{0.75}\text{O}_x$  compared to  $\text{Cu}_3\text{N}$ .

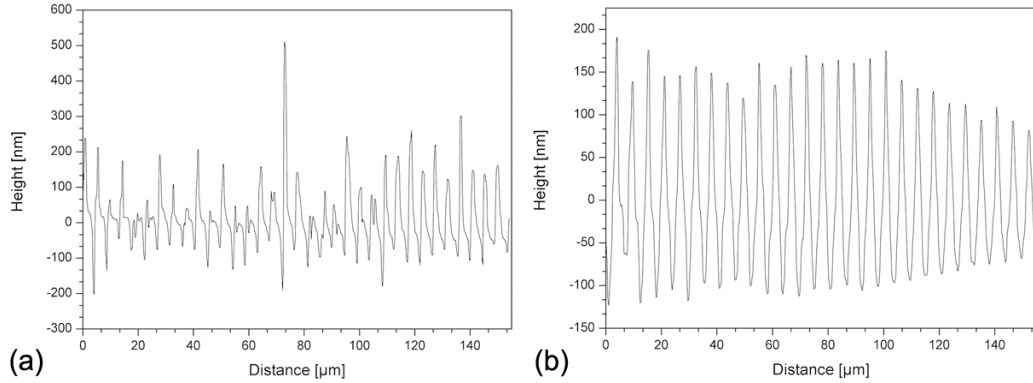


**Figure 6.3:** Surface profiles of patterned  $Cu_3N$  (a) and  $Pd_{0.25}Pt_{0.75}O_x$  (b), determined using a white light interferometer (WLI) in the observed section perpendicular to the sample surface. The positive bulges correspond to the interference maxima (region 2) and the negative cavities to the interference minima (region 1) in both films. *Reprinted from [36]*

### 6.2.3 Microstructural analysis

In order to understand and interpret the microstructure evolution of the films after laser irradiation, grazing incidence X-ray diffraction (XRD) of both as-deposited (non-patterned) and patterned states of  $Cu_3N$  and  $Pd_{0.25}Pt_{0.75}O_x$  were performed. The diffractograms in figure 6.4.b show a rough background caused by intense diffused scattering from the films and glass substrates. For the as-deposited  $Cu_3N$  film (figure 6.4a), X-ray diffraction only evidences the presence of the copper nitride phase exhibiting a strong preferred orientation in the [111] direction. However, after the laser patterning process the diffraction pattern shows an additional peak at  $d = 0.2090$  nm, which could not be interpreted as a diffraction line of  $Cu_3N$ . According to the ICDD, it can be identified as the (111) reflection peak of copper. The presence of this peak indicates that the film contains both copper nitride and copper after laser irradiation. This leads to the assumption that laser irradiation induces the partial decomposition of  $Cu_3N$  into copper and gaseous  $N_2$ . In parallel, the cell parameter of the  $Cu_3N$  phase can be estimated from the position of the (111) diffraction line of  $Cu_3N$  at 0.3841 nm for the as-deposited film and 0.3829 nm for the patterned film. The theoretical lattice

constant for  $Cu_3N$  is 0.3817 nm. The  $Cu_3N$  phase in the as-deposited state can be interpreted as overstoichiometric in nitrogen and closer to stoichiometry in the patterned state [85]. According to the XRD analysis performed in  $Pd_{0.25}Pt_{0.75}O_x$  and shown in figure 6.4.b, no crystalline phase has been detected in the as-deposited state. Thus, the as-deposited film can be considered as XRD amorphous. After patterning, the diffractogram presents two characteristics: a dominant broad diffraction peak characteristic of amorphous phases and two small, sharp and relatively well-defined peaks. The latter indicates the existence of a crystalline phase after the laser irradiation. These peaks can be identified as Pt or Pd (111) and (200). It can therefore be concluded that the laser irradiation of  $Pd_{0.25}Pt_{0.75}O_x$  induced the formation of metallic noble metal particles through the partial decomposition of the film. It is worth noting that the stable single oxides  $PdO$  and  $PtO_2$  decompose in air around 450 °C [87] and 850 °C [86] respectively.

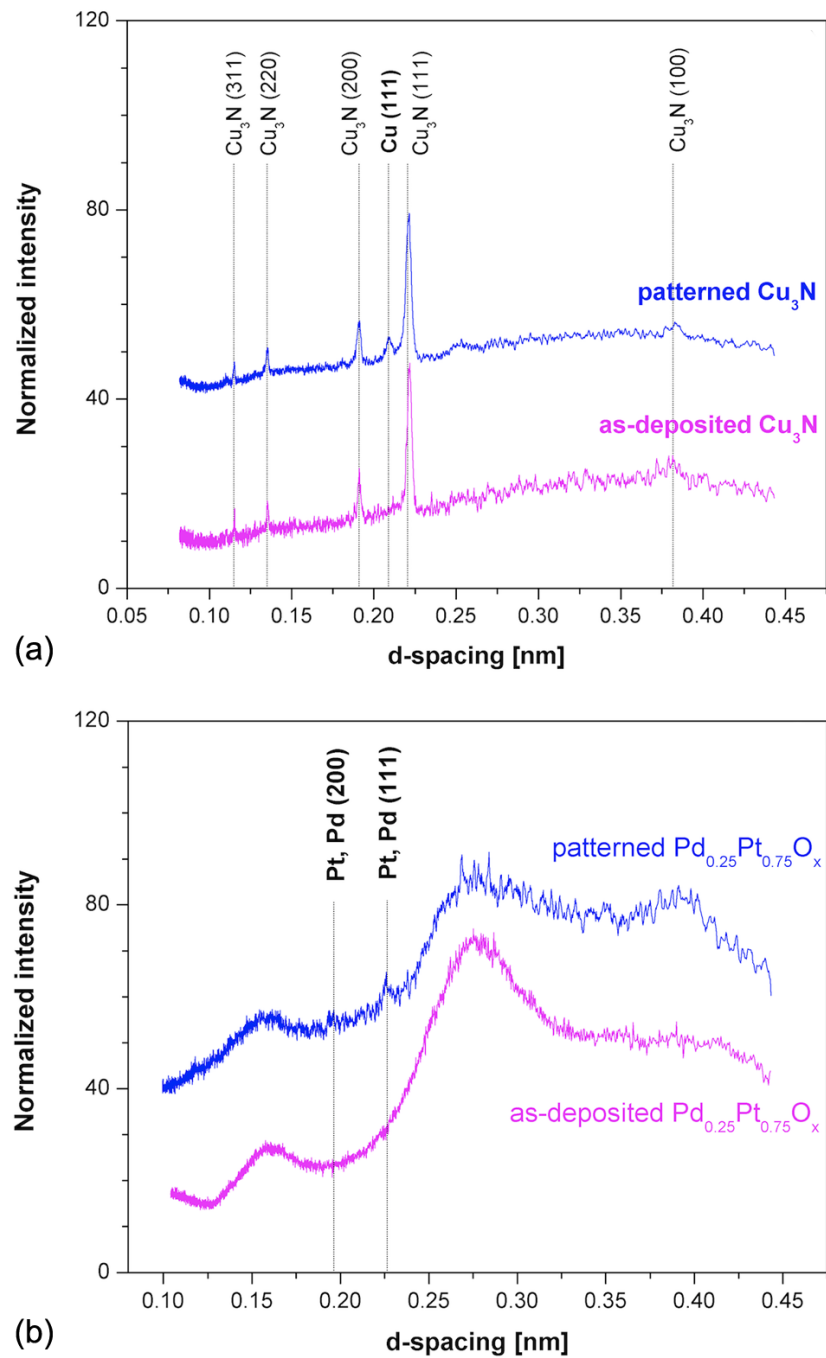


**Figure 6.4:** Grazing Incidence X-Ray diffractograms of (a) the as-deposited (un-patterned) and the patterned  $\text{Cu}_3\text{N}$  films; (b) the as-deposited and the patterned  $\text{Pd}_{0.25}\text{Pt}_{0.75}\text{O}_x$  films. In (b), the X-Ray source used for analysis of the as-deposited state is a  $\text{Co} - K\alpha$  radiation at a  $4^\circ$  incidence angle, while in the patterned state of (a) and (b), a  $\text{Cu} - K\alpha$  radiation at  $1^\circ$  incidence angle is used. Reprinted from [36]



Figure 6.5a shows the STEM image of the cross section lamella of the  $Pd_{0.25}Pt_{0.75}O_x$  laser patterned film at the boundary between an interference maximum and minimum. This sheds light on the in-depth morphology of the coating. In region 2 of the interference maximum, approximately 40 nm of the outer surface (towards the core of the film) appear to have been strongly affected by the laser irradiation. In contrast, there is no evidence of such modification in region 1 of the interference minimum. A careful observation of the film core in both regions reveals the presence of dark islands dispersed in a clear background. The size of these islands is greater near the interface between the coating and the glass substrate. This observation may indicate the presence of metal nanoparticles. TEM investigations provide further details on the actual microstructure at the nanometer scale. Figures 6.5.b and 6.5.c display the dark field images and corresponding selected area electron diffraction (SAED) pattern of the film core in the interference minimum and maximum regions, respectively. The SAED patterns show characteristic electron diffraction rings of nanocrystalline phases. The electron diffraction signature can be indexed by considering the face-centered cubic structure of platinum and palladium. The dark field images corresponding to a selected region of the (111) diffraction ring show the presence of a large amount of metallic nanoparticles at the core of the coatings. The typical size of these particles is in the nanometer range. Local particle aggregations are observed, which may correspond to the dark islands observed by STEM. Moreover, it partially explains the detection of the X-ray diffraction peak of metallic platinum and/or palladium after laser irradiation (figure 6.4b). It was not possible to evidence a clear difference in the particle density between the interference minimum and maximum cores. It is worth noting that bigger particles were observed near the interface between the  $Pd_{0.25}Pt_{0.75}O_x$  coating and the glass substrate and in the area near the surface of the interference maximum region. The poor thermal diffusivity of glass can explain a significant laser energy accumulation at the film/substrate interface facilitating the decomposition of the oxide film and the growth of metal particles. Similar processes may be present in the  $Cu_3N$  films that show similar STEM features as in the  $Pd_{0.25}Pt_{0.75}O_x$  films after interference.

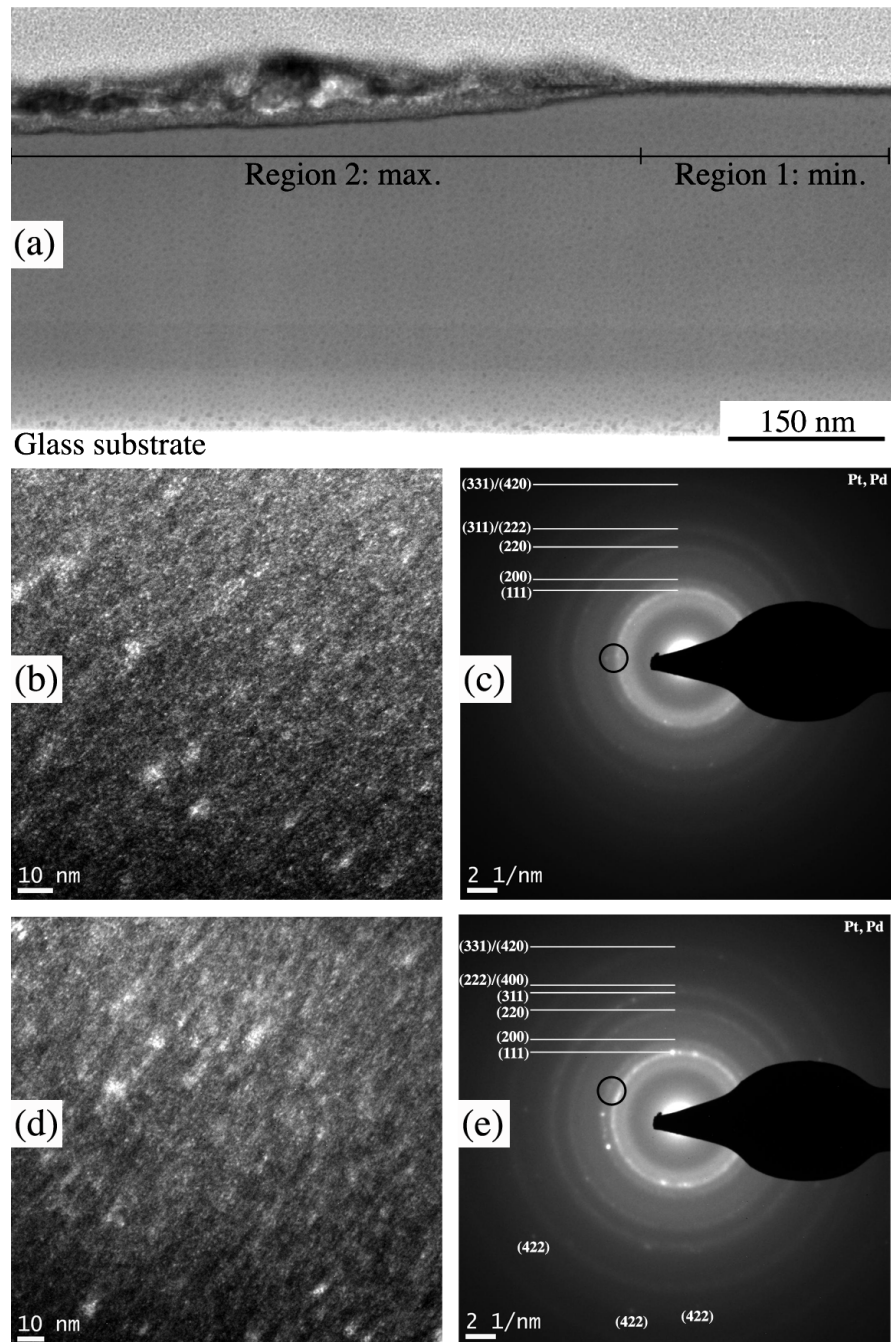


**Figure 6.5:** Microstructural investigations of  $Pd_{0.25}Pt_{0.75}O_x$  films. (a) shows a STEM image of the cross-section lamella at the boundary between maximum and minimum interference. (b) and (d) provide dark field images of the interference minimum and maximum regions, respectively. (c) and (e) display the corresponding selected area diffraction (SAED) patterns in the marked circle, exhibiting electron diffraction rings characteristic of nanocrystalline phases. *Partially reprinted from [36]*

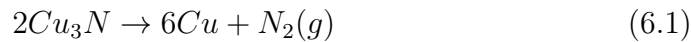
## 6.2.4 Chemical composition analysis

In order to locate the possible phase changes that appeared after laser patterning, already suggested through the aforementioned XRD analyses, further EDS measurements were performed at the film surface and are summarized in tables 6.1 for  $Cu_3N$  and 6.2 for  $Pd_{0.25}Pt_{0.75}O_x$ . First, line scans over two pattern periods were performed in the  $Cu_3N$  sample and show an overall sinusoidal fluctuation of the nitrogen concentration. The corresponding graphs are not enclosed due to insufficient picture resolution for correct visualization. We therefore additionally provide in tables 6.1 and 6.2 the results of the chemical composition measurements in randomly selected areas of regions 1 and 2.

	Region 1 (at. %)	Region 2 (at. %)
N	20.3	14.3
Cu	79.7	85.7

**Table 6.1:** Randomly evaluated chemical composition by EDS of patterned  $Cu_3N$  in regions 1 (interference minima) and 2 (interference maxima).

The amount of nitrogen in the porous and foamy region 2 is obviously lower (about 6 at.%) than that of the as-deposited region 1. This elemental distribution (see in table 6.1) of nitrogen and copper supports the hypothesis that  $Cu_3N$  at least partially decomposes in region 2 around the laser interference maxima. Usually, copper nitride decomposes into metallic copper ( $Cu$ ) and nitrogen ( $N_2$ ) at a low temperature, in the 100 – 470 °C range [81–84]. Around the interference maxima (region 2), the absorbed laser energy is high enough to heat the whole film up to, or even above, the decomposition temperature. Laser patterning thus triggers the thermal decomposition of copper nitride. The film morphology in this region even suggests a surface boiling of the film followed by rapid quenching. According to the following reaction, nitrogen can be evaporated from the film and metallic copper can be formed (confirmed by XRD analysis):



Because of the emission of gaseous nitrogen, the film bulged and burst outwards, forming numerous pores, thereby explaining the foamy microstructure observed at the surface of region 2 (figure 6.3.b). The results of randomly selected measurements in regions 1 and 2 of the  $Pd_{0.25}Pt_{0.75}O_x$  film (figure 6.2.c) are available in table 6.2.

	Region 1 (at. %)	Region 2 (at. %)
O	71.9	66.9
Pt	20.7	24.1
Pd	7.4	9.0

**Table 6.2:** Randomly evaluated chemical composition by EDS of patterned  $Pd_{0.25}Pt_{0.75}O_x$  in region 1 (interference minima) and region 2 (interference maxima).

Even though EDS usually overestimates the oxygen content, the chemical composition can be roughly described as a linear combination of those of  $Pt_2O$  and PdO. Secondly, they indicate an evaporation of oxygen together with the formation of metallic platinum in region 2 (interference maximum). From the existence of white tiny porous clusters observed in figure 6.2.c, characteristic of the patterned  $Pd_{0.25}Pt_{0.75}O_x$  morphology, one can assume that such a microstructure evolution is caused by the laser-triggered surface decomposition of  $Pd_{0.25}Pt_{0.75}O_x$  in metallic Pt and the parallel evaporation of oxygen. This observation, together with the two diffraction lines attributed to Pt (111) and (200) revealed by the diffractogram of patterned  $Pd_{0.25}Pt_{0.75}O_x$ , shows that this film can be locally partially decomposed.

### 6.2.5 Evolution of the electrical resistivity

The two systems previously characterized were then analyzed with the four-point probe method. The two films were laser-irradiated by several contiguous single pulses to form a patterned area of  $10 \times 10 \text{ mm}^2$  and the measurements of their electrical resistivity were performed both in the as-deposited state and after patterning. Moreover, a distinction has been made by measuring both films in the directions parallel and perpendicular to the line-like pattern. The results are summarized in table 6.3.

	As-deposited $\rho(\times 10^{-6}\Omega m)$	Perpendicular $\rho(\times 10^{-6}\Omega m)$	Parallel $\rho(\times 10^{-6}\Omega m)$
$Cu_3N$	$> 2.7 \pm 6.10^{-3}$	$1.0856 \pm 7.10^{-3}$	$1.09056 \pm 7.10^{-3}$
$Pd_{0.25}Pt_{0.75}O_x$	$116790 \pm 143$	$3672 \pm 2$	$3548 \pm 2$

**Table 6.3:** Evolution of electrical film resistivity  $\rho$ , measured by the four-point probe method in  $Cu_3N$  and in  $Pd_{0.25}Pt_{0.75}O_x$ , both before and after laser irradiation. A distinction has been made as to measuring perpendicular or parallel to the line-like pattern.

All the patterned samples have lower resistivity than their corresponding as-deposited ones, although their surfaces become more porous and rough: the resistivity of the  $Cu_3N$  film is about 60% lower after laser irradiation and the resistivity of the patterned  $Pd_{0.25}Pt_{0.75}O_x$  is about 31 times lower (about 97%). Since in all these laser-irradiated samples a partial decomposition occurs as a result of the laser patterning, the large decrease in the resistivity after patterning can be considered as a result of these decomposition processes. In  $Cu_3N$ , metallic copper was formed after patterning due to the partial decomposition of copper nitride and the evaporation of nitrogen. Therefore, two phases coexist in this state: a low resistive phase (metallic Cu) and a semiconducting phase (consisting of residual  $Cu_3N$  crystals), whose conductivity is highly sensitive to its nitrogen stoichiometry [8]. As the cell parameter of the  $Cu_3N$  phase decreases after patterning, so does its resistivity. Therefore it can be assumed that better electrical conduction paths are established via metallic Cu precipitates and quasi-stoichiometric  $Cu_3N$ . An effective medium [40] is generated which consists of three different phases: metallic Cu,  $Cu_3N$  and pores. In the second system,  $Pd_{0.25}Pt_{0.75}O_x$ , the resistivity variation may result from a slightly different mechanism. The segregation of platinum provides sites with low electrical resistivity coexisting with pores and a highly resistive  $Pd_{1-y}Pt_yO_x$  phase, with a y value necessarily lower than 0.75 and whose resistivity is different from the initial  $Pd_{0.25}Pt_{0.75}O_x$  phase. The resistivities resulting from the current established parallel and perpendicular to the pattern show a very small and non significant difference (see in table 6.3): less than 0.5% in  $Cu_3N$  and about 3.4% in  $Pd_{0.25}Pt_{0.75}O_x$ . In  $Cu_3N$ , the electrical resistivity in the direction perpendicular to the pattern is even slightly lower than that in the parallel direction.

The energy dissipated at the interference minima is not equal to zero [22] and the interaction time allows some thermal diffusion from region 2 to region 1. Thus, although the morphology of region 1 is apparently unaffected by the laser interaction, some changes occur such as a modification of the nitrogen / oxygen stoichiometry and the precipitation of metallic particles as shown for the  $Pd_{0.25}Pt_{0.75}O_x$ . The observation of metallic particle precipitation is thus in line with the reduction of resistivity occurring after the laser treatment and the absence of electrical heterogeneity between parallel and perpendicular measurement directions. If the decomposition of the oxide coating was complete but limited to the interference maxima regions, the serial and parallel resistance model could be used to explain the electrical behaviour. Since the resistivity of a metal (in the  $\mu\Omega cm$  range) is much lower than that of the as deposited oxide, parallel and perpendicular measurements would be initially determined by the metal and oxide resistivity, respectively. The decomposition of  $Cu_3N$  and  $Pd_{0.25}Pt_{0.75}O_x$  triggered by laser interference is demonstrated, yet without any clear observation of an anisotropy of the electrical resistivity. Shorter and repeated interference times are known to minimize the thermal effect of laser interference treatments and to minimize thermal conduction [27]. Therefore, future investigation directions should include multiple pulses in the femto/pico-second time scale to try to steepen the transition between regions 1 and 2 and to minimize porosity formation in region 2.

### 6.3 Summary

A local laser-induced chemical decomposition of  $Cu_3N$  and  $Pd_{0.25}Pt_{0.75}O_x$ , leading to a significant lowering of the electrical resistivity has been reported. After structuring those systems by means of laser interference, metallic low-resistive Cu and Pt precipitates have been formed from the nitride and oxide films, together with an evaporation of nitrogen and oxygen, respectively. This evaporation generates a porous and foamy microstructure at the surface of the interference maxima regions. The chemical composition of the oxide or nitride matrix is also affected by the irradiation. These phenomena result

in the lowering of the overall sample resistivity. Furthermore, the expected resistivity anisotropy, resulting from the geometry of the interference pattern is not observed. This can be explained by the precipitation of metallic nanoparticles in the film core independently of the interference maxima and minima zones and by the introduction of porosity at the interference maxima surfaces.





## Chapter 7

# Segregation and growth of nanoparticles for the reduction of the friction coefficient\*

**ABSTRACT:** Laser interference patterning and the hereby induced microstructure modifications have been investigated in gold/yttria-stabilized zirconia nanocomposite films. Transmission electron microscopy was used to study the influence of the laser treatment on the structure and microstructure of the samples. The impact of laser patterning on the friction coefficient has been evidenced. The initial microstructure consisted of gold nanograins homogeneously distributed in the yttria-stabilized zirconia matrix. A noticeable growth and coalescence of gold nanograins occurred near the surface in specific regions. Simultaneously, a foamy morphology, mostly consisting of gold crystals, was formed at the surface and is responsible for a drastic diminution of the friction coefficient after patterning. Furthermore, the influence of the film topography on the friction behaviour is analysed using Abbot-Firestone curves. In contrast to thermal annealing, the laser treatment proposed here is a fast procedure to partially relocate gold at the film surface and provide a local solid lubrication.

---

\*Published in R. Catrin et al. *Mat. Res. Soc. Symp. Proc.* **1339**:mrss11-1339-s01-04, 2011 [35] and in R. Catrin et al. *J. Mat. Res.* 27(6):879-885, 2012 [34].

## 7.1 Introduction

Innovation in materials science relies on the possibility to control the morphology, microstructure and chemistry of materials. Specific properties can thereby be obtained. Noble metals are fascinating for various reasons, among which is their poor reactivity towards oxygen or absence thereof. The association of noble metals with other metallic elements can produce original microstructures and morphologies, more particularly upon thermal annealing and in the presence of oxygen [79, 80]. We recently showed that the electrical conductivity of noble-metal-based oxides and nitrides can be tailored by laser interference patterning [36]. Within this method, described in detail in [25], the interference of single laser pulses is used to tailor both the morphology and the microstructure of thin films [21]. Due to a high local thermal gradient produced in a very short time, metallurgical effects like lateral grain growth [21, 22], chemical decomposition [36] or intermetallic phase precipitation [32] are promoted. Gold is the only element that does not present a thermodynamically stable oxide under normal conditions. In contrast, zirconium and yttrium are highly reactive towards oxygen as they can form zirconia ( $ZrO_2$ ) and yttria ( $Y_2O_3$ ). Therefore, upon synthesis of thin films constituted by Au, Zr, Y and O atoms, gold is expected to segregate in metallic form in an oxide matrix. The present study is dedicated to the effect of laser interference patterning on the structure, microstructure and friction behaviour of sputter-deposited gold/yttria-stabilized zirconia (Au-YSZ) nanocomposite films. This chemical system is of interest for its potential applications in the field of catalysis [88] and gas detection [89]. Moreover, and important for our case, Au-YSZ nanocomposites were shown to exhibit improvements in tribological properties compared to YSZ due to microstructural adaptive changes influencing the friction coefficient [41–43].

## 7.2 Results and discussion

### 7.2.1 Thermodynamics of the Au-YSZ system

The Gibbs energy of formation of a compound allows to evaluate its stability in a given environment. Figure 7.1 displays the thermal evolution, under 1 bar of air, of the Gibbs energy of formation ( $\Delta G_f$ ) of  $ZrO_2$  and  $Y_2O_3$  as well as the standard Gibbs energy of formation ( $G$ ) of auric oxide  $Au_2O_3$ .

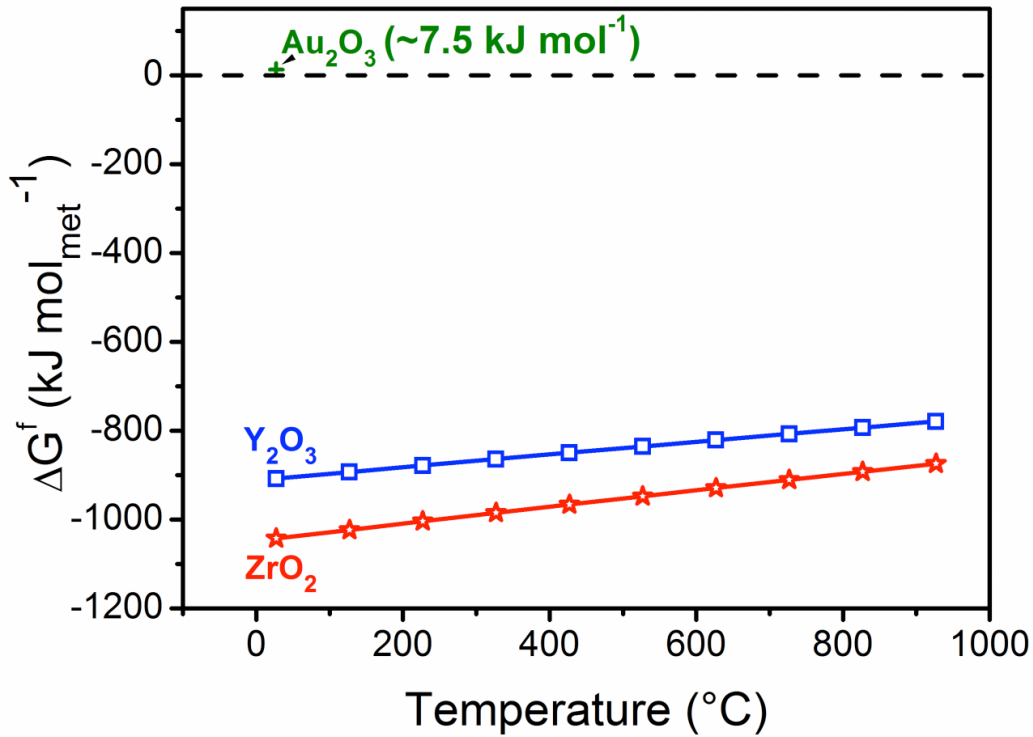


**Figure 7.1:** Thermal evolution, under 1 bar of air, of the Gibbs energy of formation of  $ZrO_2$ ,  $Y_2O_3$  and the standard Gibbs energy of formation of  $Au_2O_3$ . The values are given for 1 mol of metal. Reprinted from [35]

The standard value of  $\Delta G_f$  for 1 mole of metal for  $Au_2O_3$  was taken from [90] while the thermal evolutions of  $\Delta G_f$  for 1 mole of metal for  $ZrO_2$  and  $Y_2O_3$  were calculated using the data tabulated in [91] as follows:

$$\Delta G_f^{ZrO_2} = G^{ZrO_2} - G^{Zr} - G^{O_2} \quad (7.1)$$

$$\Delta G_f^{Y_2O_3} = \frac{1}{2}(G^{Y_2O_3} - 2G^Y - \frac{3}{2}G^{O_2}) \quad (7.2)$$

Negative values indicate the thermodynamic stability of the compound; the magnitude indicates the reactivity of the metallic element towards oxygen. Given the strongly negative values of  $\Delta G_f$  for  $ZrO_2$  and  $Y_2O_3$ , it is expected that Zr and Y will be oxidized in the as-deposited state and will remain in this state upon heating. In contrast, gold should be present in the metallic state. Therefore, in contrast to recent observations in the Pd-Zr-Y-O system [88], nanocomposite films consisting of gold particles embedded in a YSZ matrix are expected to form by condensing Au, Zr, Y and O atoms as observed in [41–43]. Furthermore, no chemical reaction should occur upon heating the Au-YSZ films, unless the melting point of YSZ (2680 °C) is reached with the LIP treatment.

## 7.2.2 Segregation and grain-growth of Au nanoparticles

The observation by SEM of the film surface after LIP indicates an alternation of bands with a constant width throughout each spot. The bands are of two distinct morphologies, namely smooth (region 1) and rough (region 2), and are repeated with a period equal to the interference period (P). Using SEM, it was impossible to detect the slightest difference between the surface morphology of the as-deposited film and region 1 after LIP. Therefore, regions 1 and 2 correspond to the interference minima and maxima, respectively. Figure 7.2.a shows the surface of the sample treated with  $P = 5 \mu\text{m}$ . A typical selected area electron diffraction (SAED) pattern for region 1 is displayed in 7.2.b-left. The broad and weak diffraction rings highlight the nanocrystalline character of the coating. These have been ascribed to metallic gold and YSZ. Thus, an Au-YSZ nanocomposite arrangement was formed upon the vapour condensation. This is in line with both the X-ray diffraction analysis conducted by Voevodin et al. [41–43] on thermally annealed films of similar Au content and with the thermodynamic considerations above.

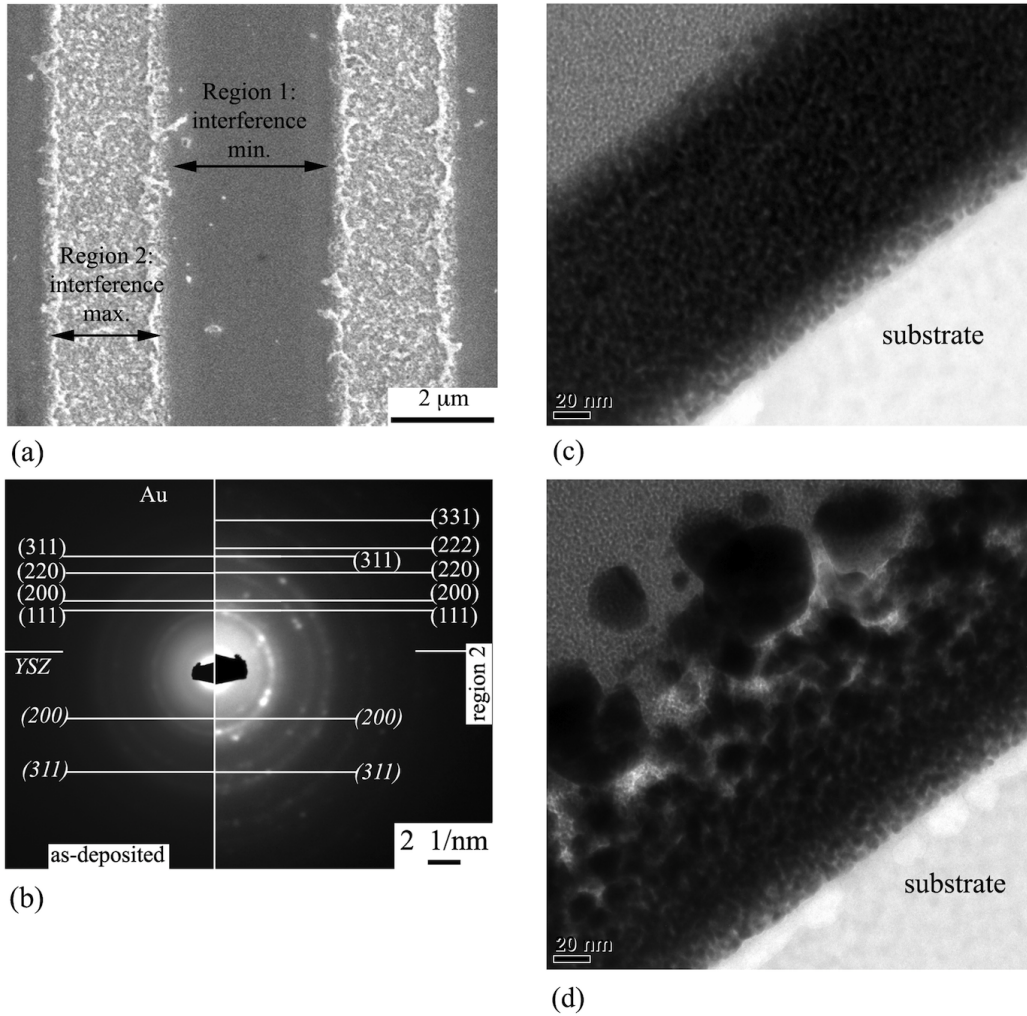


**Figure 7.2:** (a) Morphology evolution of laser-interference-patterned Au-YSZ thin films observed by SEM. Regions 1 and 2 correspond to the laser interference minimum and maximum, respectively. (b-d) Microstructural investigations of Au-YSZ. Part (b) displays SAED patterns from the as-deposited state (b-left) and region 2 (b-right). (c) and (d) provide bright field views of the as-deposited state and region 2, respectively. *Reprinted from [35]*

Additionally, the dark spots observed on the corresponding bright field TEM image in 7.2.c can be ascribed to gold nanoparticles, whose average diameter has been estimated at 6 nm and confirmed by X-ray diffraction analysis. The particles are homogeneously dispersed in the YSZ matrix without significant changes in the microstructure throughout the film thickness. As

observed in 7.2.d, LIP had a massive impact on the crystal growth near the surface of the interference maximum zone (region 2). Approximately half of the film thickness is strongly affected by the treatment. Notably, a foamy morphology consisting of gold crystals was formed at the film surface. These changes resulted, not only in an enhanced definition of the electron diffraction rings of Au and YSZ, but also in the presence of well-separated spots for metallic gold (7.2.b-right). Therefore, the local heating induced by LIP triggered a local growth of the gold particles.

### 7.2.3 Dry lubrication effect

Friction tests have been performed on pure YSZ and on as-deposited and laser patterned Au-YSZ films. In the case of LIP-treated samples, the sliding direction (parallel or perpendicular to the interference bands) has been considered in order to study the effect of the anisotropy induced by the laser treatment. 7.3 presents the friction coefficient ( $\mu$ ) of a pure YSZ film and of the Au-YSZ nanocomposite films before and after LIP for two structure periods (5  $\mu\text{m}$  and 15  $\mu\text{m}$ ) and sliding directions (parallel or perpendicular to the interference bands). The friction coefficient of pure YSZ is quite high at  $0.54 \pm 0.06$ . It is observed that the incorporation of gold nanoparticles strongly lowers the value of  $\mu$  down to  $0.18 \pm 0.01$ . After LIP the reduction is even more pronounced (down to  $0.051 \pm 0.008$ ), which could be ascribed to the partial relocation of Au at the film surface through laser-induced crystal grain growth and diffusion as observed by TEM (7.2.d). This provides a local solid lubrication that matches the observations made by Voevodin et al. on thermally annealed samples [41–43]. Moreover, both the structure-pattern period and the sliding direction appear to significantly influence the friction behaviour. For the sliding direction parallel to the interference bands, the structure periods of 5  $\mu\text{m}$  and 15  $\mu\text{m}$  lead to similar values of  $\mu$  of  $0.091 \pm 0.008$ . Compared to sliding tests in the parallel direction, tests perpendicular to the interference bands lead to increased values of  $\mu$  at  $P = 5 \mu\text{m}$  and decreased values at  $P = 15 \mu\text{m}$ . It is generally accepted that  $\mu_{\text{perpendicular}} < \mu_{\text{parallel}}$  [92].

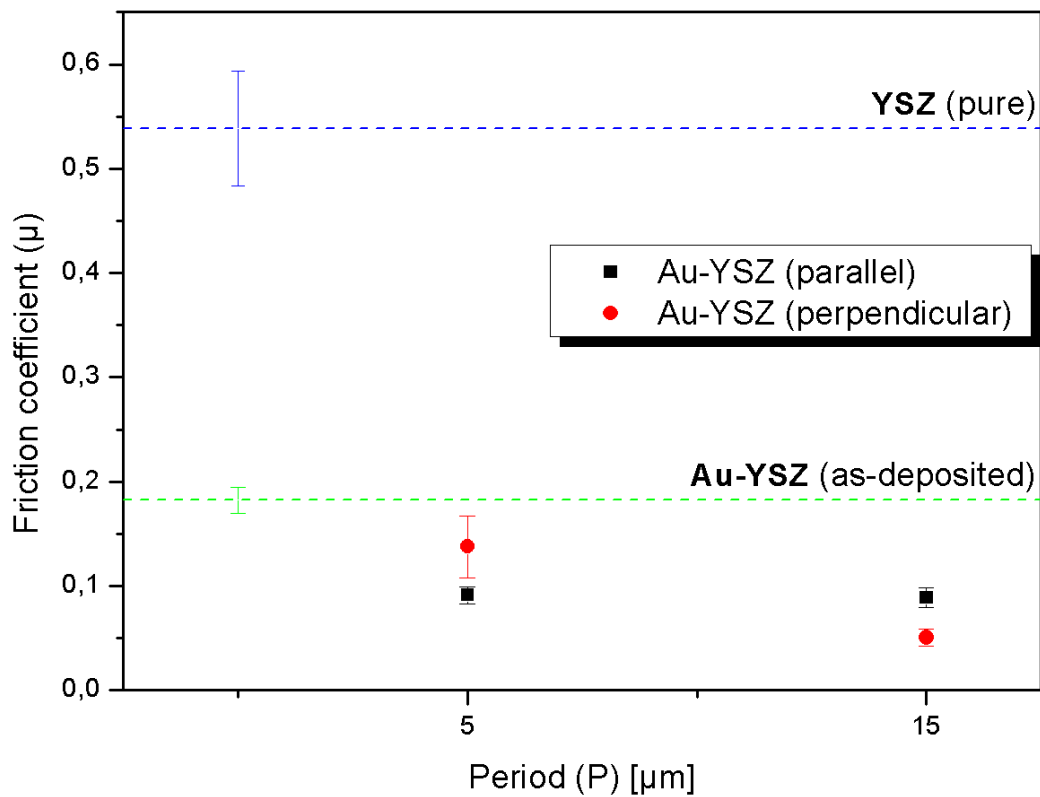


**Figure 7.3:** Friction coefficient of Au-YSZ films before and after patterning, depending on the structure period (5  $\mu\text{m}$  and 15  $\mu\text{m}$ ) and the sliding direction (parallel or perpendicular). The friction coefficient of a pure YSZ film is given for reference.

Views of the residual wear track after 100 cycles are shown in 7.4 for the two structure periods and the two sliding directions. The white bands correspond to the interference maxima and the dark bands to the interference minima. The similarity of the results obtained with 5  $\mu\text{m}$  and 15  $\mu\text{m}$  can be explained through the wear track, which is wider than the patterning period: the sliding ball hardly “feels” the difference between the two geometries. Even though it has not been quantified in this study, the contact areas in the wear track should be equivalent in both cases.

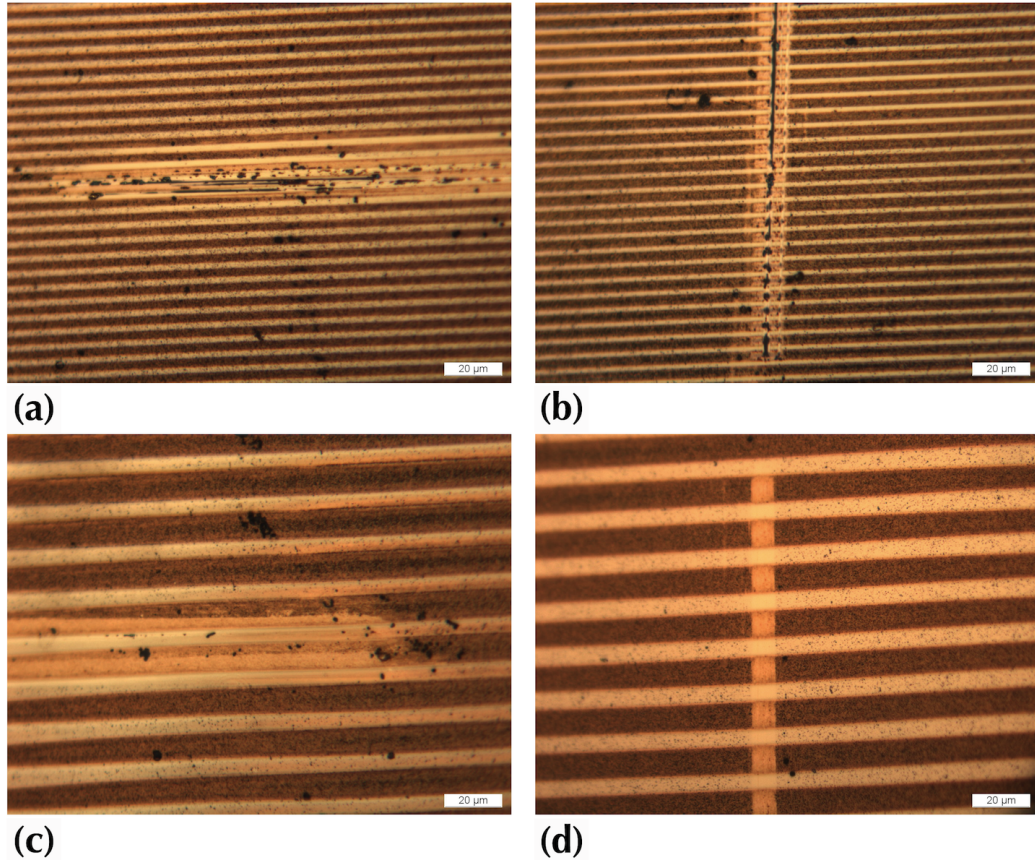


**Figure 7.4:** Views of the wear track for the two structure periods: (a, b) 5  $\mu\text{m}$ , (c, d) 15  $\mu\text{m}$  – for both parallel (a, c) and perpendicular (b, d) sliding directions. The scale in the lower right corners corresponds to 20  $\mu\text{m}$ .

In order to propose an explanation for the differences resulting from sliding tests perpendicular to the interference bands, the surface roughness of the patterned films was analyzed using WLI; the results are summarized in figure 7.5.a in the form of Abbott-Firestones curves,  $R_{sk}$ ,  $R_{ku}$  and local surface profiles. In the case of the film patterned at 15  $\mu\text{m}$ ,  $R_{sk}$  presents a negative value (-0.015) and  $R_{ku}$  has a value of 2.737. Both values are characteristic for a bumpy bearing surface, which is confirmed by the depth profile in 7.6. Moreover, the fact that  $R_{ku}$  has a value of 2.737, close to 3, indicates the high randomness of the profile. In contrast, the film patterned at 5  $\mu\text{m}$  presents a high value of kurtosis ( $R_{ku} = 3.995$ ). The surface randomness is low, in accordance with the low structure period, and  $R_{sk}$  is positive.



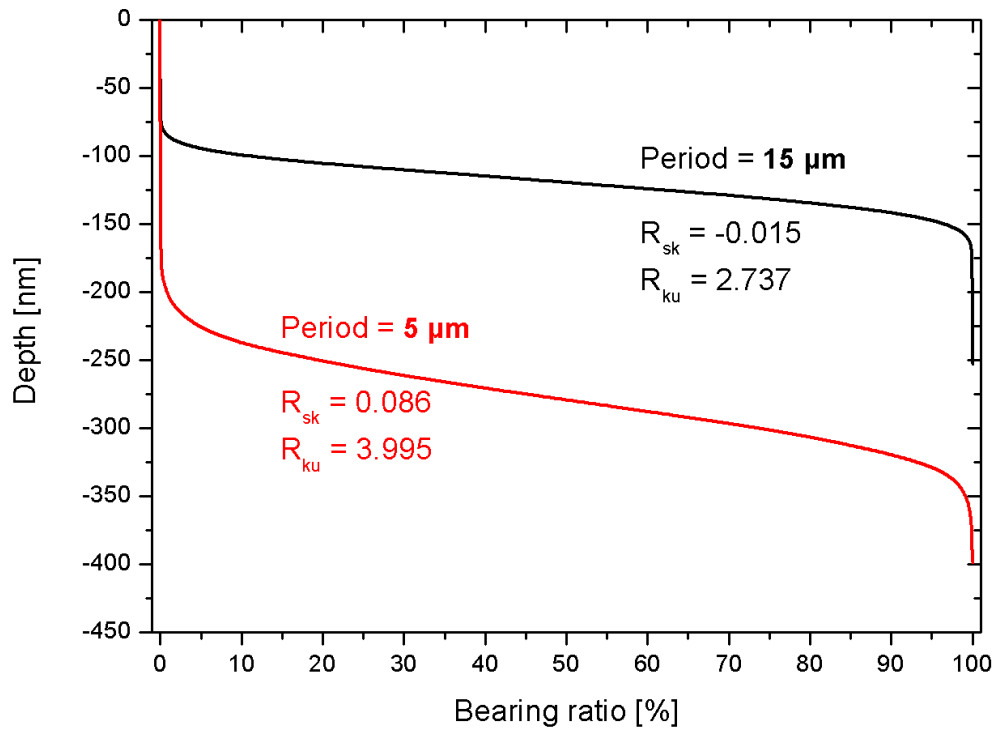


**Figure 7.5:** Calculation of the Abbott-Firestone curves, skewness ( $R_{sk}$ ) and kurtosis ( $R_{ku}$ ) for the patterned Au-YSZ with periods of 5 μm and 15 μm.

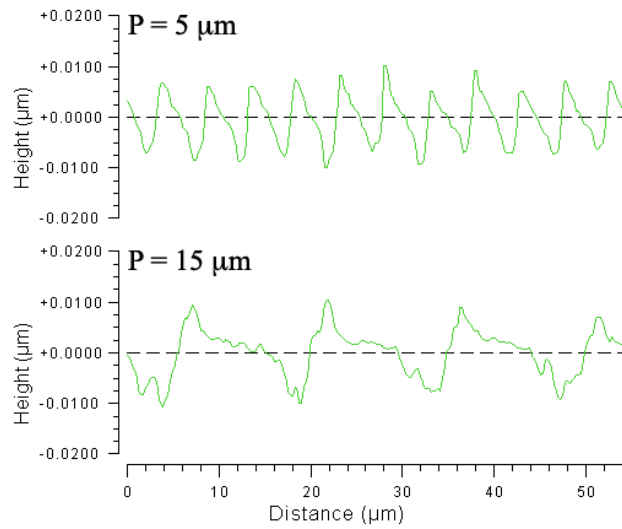


**Figure 7.6:** Local surface profiles characteristic for the two structure periods (5 μm and 15 μm).

Both values are consistent with a peaky surface as seen in figure 7.6, which results in high contact pressure. In the Abbott-Firestone curves in figure 7.5, it is observed that at a similar bearing ratio, the structure at 5  $\mu\text{m}$  should be more damaged. This can result in a prior delamination of the film as observed in 7.4.b and explain the higher friction coefficient in perpendicular sliding for this film.

### 7.3 Summary

The influence of laser interference patterning (LIP) on the microstructure of sputter-deposited nanocomposite Au-YSZ thin films with a Au/(Au+Zr+Y) ratio of 0.55 has been investigated by transmission electron microscopy. The gold atoms of Au-YSZ are present in the form of metallic nanograins in a YSZ matrix after deposition, which is consistent with the positive standard enthalpy of formation of auric oxide  $Au_2O_3$ . In the interference maxima zones, LIP induced a noticeable growth of gold grains and foam near and at the film surface, respectively. Friction tests indicate that the presence of gold nanoparticles in the as deposited state reduces the friction coefficient by a factor 3 compared to pure YSZ. The reduction is even more drastic after the LIP treatment was applied. Indeed friction coefficients in the 0.05-0.14 range were achieved depending on the patterning period and sliding direction. The lower friction coefficient after patterning can be explained through the relocation of gold at the film surface and through the surface profile generated by LIP as evidenced in the Abbott-Firestone curves. These results can benefit tribological applications for which dry lubrication is desirable. In contrast to thermal annealing, LIP is a fast and localized process.

# Chapter 8

## Conclusions and outlook

Different aspects of the microstructure modification of metallic thin films via Laser Interference Patterning were studied in the present work. The major achievements are highlighted as follows.

1. **Production of periodic arrays of interference minima and maxima.** Rapid melting and lateral solidification through the entire film thickness produced alternated nano- and micro-grained (larger than the film thickness) microstructures.
2. **Tailored crystallization behaviour.** By adjusting the irradiation parameters on the different pure metallic films, three energy density regimes could be observed: partial melting, complete melting or Super Lateral Growth (between partial and complete melting).
3. **Laser-induced temperature gradient.** Thermal simulations of the patterned samples revealed a significant temperature difference between interference minima and maxima, *e.g.* reaching 3000 K in the case of Ti/W films. Marangoni convection forces were also argued to be responsible for the topography within the solidification process.
4. **Grain size and grain orientation control.** Laser processing was shown to allow the control of the grain size distribution and the modification of the film texture.

5. **Mechanical composite effect.** The produced arrays of different grain sizes have enabled a hardness difference of about 30% between interference minima and maxima. The microstructure modification of the as-deposited films results in an increase of the stiffness (large-grained microstructure) without loss of ductility (nano-grained microstructure).
6. **Fabrication of periodic architectures for selective etching.** The microcrystalline zones of specifically oriented grains have shown a higher resistance against the wet chemical etchant, which places the laser-assisted procedure as a possible low cost alternative to conventional lithographic techniques.
7. **Control of the local conductivity.** The microscale periodic laser-induced chemical decomposition of particles in certain thin films is responsible for a macroscopic decrease of the electrical resistivity of 60% ( $Cu_3N$ ) to several orders of magnitude ( $Pd_{0.25}Pt_{0.75}O_x$ ).
8. **Microstructure relocation and reduction of friction coefficient.** The periodic heat treatment induced by LIP allowed a precise segregation and crystal growth of gold particles in specific areas of the films, leading to a significant decrease of up to 70% in the friction coefficient.

These results reveal the potential of the LIP method in two industrial fields.

- **Electronics.** Since the fabrication of electrical devices on a variety of substrates needs different processing techniques to achieve electrically functional electronics or optical inks, LIP makes the bridge between materials science and the electronics industry. By locally controlling the electrical conductivity through chemical decomposition or particle segregation in the material, no additional step is needed *e.g.* for creating conducting bridges in electronics boards, simplifying the overall production processes.
- **Tribology and catalysis.** In dry lubrication applications where no lubricant is desired, the localized and periodic heat treatment induced by LIP allows a precise relocation of the microstructure. Particle segregation

(*e.g.* Au nanoparticles) and further crystal growth at the sample surface improve the wear behaviour. Despite the solid phase, such enhanced films are able to reduce friction between the two contacting surfaces without the need for a liquid medium.



## References

- [1] E. Arzt. Size effects in materials due to microstructural and dimensional constraints: a comparative review. *Acta Materialia*, 46(16):5611–5626, 1998.
- [2] D. Pirzada, P. Trivedi, D. Field, and G.J. Cheng. Effect of film thickness and laser energy density on the microstructure of a-GaAs films after excimer laser crystallization. *Journal of Applied Physics*, 102:013519–1–9, 2007.
- [3] J.E. Kline and J.P. Leonard. Rapid lateral solidification of pure Cu and Au thin films encapsulated in  $SiO_2$ . *Applied Physics Letters*, 86(201902):1–3, 2005.
- [4] M. Hatano, S. Moon, M. Lee, K. Suzuki, and C.P. Grigoropoulos. Excimer laser-induced temperature field in melting and resolidification of silicon thin films. *Journal of Applied Physics*, 87(1):36–43, 2000.
- [5] M. Lee, S. Moon, M. Hatano, and C.P. Grigoropoulos. Ultra-large lateral grain growth by double laser recrystallization of a-Si films. *Applied Physics Letters A.*, 73:317–322, 2001.
- [6] J. S. Im, M. A. Crowder, R. S. Sposili, J. P. Leonard, H. J. Kim, J. H. Yoon, V. V. Gupta, H. Jin Song, and H. S. Cho. Controlled super-lateral growth of Si films for microstructural manipulation and optimization. *Physica status solidi (a)*, 166(2):603–617, 1998.

- [7] H.J. Kim and J.S. Im. Optimization and transformation analysis of grain-boundary-location-controlled Si films. volume 397, pages 401–406, 1996.
- [8] G. Aichmayr, D. Toet, M. Mulato, P.V. Santos, A. Spangenberg, S. Christiansen, M. Albrecht, and H.P. Strunk. Lateral grain growth during the laser interference crystallization of a-Si. *Physica status solidi (a)*, 166(2):659–666, 1998.
- [9] R. Ishihara and M. Matsumura. Excimer-laser-produced single-crystal silicon thin-film transistors. *Japanese Journal of Applied Physics*, 36(10):6167–6170, 1997.
- [10] R.F. Wood, C.W. White, and R.T. Young. Semiconductors and semimetals. In *Pulsed laser processing of semiconductors*, volume 23. Academic press, New York, 1984.
- [11] J.S. Im, H.J. Kim, and M.O. Thompson. Phase transformation mechanisms involved in excimer laser crystallization of amorphous silicon films. *Applied Physics Letters*, 63(14):1969–1971, 1993.
- [12] N. Yamauchi and R. Reif. Polycrystalline silicon thin films processed with silicon ion implantation and subsequent solid-phase crystallization: Theory, experiments, and thin-film transistor applications. *Journal of Applied Physics*, 75(7):3235–3257, 1994.
- [13] R.S. Sposili and J.S. Im. Sequential lateral solidification of thin silicon films on  $SiO_2$ . *Applied Physics Letters*, 69(19):2864–2866, 1996.
- [14] H.J. Kim and J. S. Im. New excimer-laser-crystallization method for producing large-grained and grain boundary-location-controlled Si films for thin film transistors. *Applied Physics Letters*, 68(11):1513–1515, 1996.
- [15] G. Aichmayr, D. Toet, M. Mulato, P.V. Santos, A. Spangenberg, and R.B Bergmann. Growth mechanisms in laser crystallization and laser interference crystallization. *Journal of Non-Crystalline Solids*, 227-230:921–924, 1998.



- 
- [16] C.E. Nebel, S. Christiansen, H.P. Strunk, B. Dahlheimer, U. Karrer, and M. Stutzmann. Laser-interference crystallization of amorphous silicon: applications and properties. *Physica status solidi (a)*, 166:667–674, 1998.
- [17] M. K. Kelly, J. Rogg, C. E. Nebel, M. Stutzmann, and Sz. Kátai. High-resolution thermal processing of semiconductors using pulsed-laser interference patterning. *Physica Status Solidi (a)*, 166(2):651–657, 1998.
- [18] M. Heintze, P.V. Santos, C.E. Nebel, and M. Stutzmann. Lateral structuring of silicon thin films by interference crystallization. *Applied Physics Letters*, 64(23):3148–3150, 1994.
- [19] K.K. Dezfulian, J.P. Krusius, M.O. Thompson, and S. Talwar. Laser-induced lateral epitaxy in fully depleted silicon-on-insulator junctions. *Applied Physics Letters*, 81(12):2238–2240, 2002.
- [20] C. Eisele, M. Berger, M. Nerding, H.P. Strunk, C.E. Nebel, and M. Stutzmann. Laser-crystallized microcrystalline silicon alloys for thin film solar cells. *Thin Solid Films*, 427(1-2):176–180, 2003.
- [21] R. Catrin, A. Lasagni, C. Gachot, U. Schmid, and F. Mücklich. Microstructural design of advanced architectures in titanium/platinum thin films by laser interference metallurgy. *Advanced Engineering Materials*, 10(5):466–470, 2008.
- [22] C. Gachot, R. Catrin, A. Lasagni, U. Schmid, and F. Mücklich. Comparative study of grain sizes and orientation in microstructured Au, Pt and W thin films designed by laser interference metallurgy. *Applied Surface Science*, 255(10):5626–5632, 2009.
- [23] A. Lasagni, M. Nejati, R. Clasen, and F. Mücklich. Periodical surface structuring of metals by laser interference metallurgy as a new fabrication method of textured solar selective absorbers. *Advanced Engineering Materials*, 8(6):580–584, 2006.

- [24] F. Mücklich, A. Lasagni, and C. Daniel. Laser interference metallurgy - Periodic surface patterning and formation of intermetallics. *Intermetallics*, 13(3):437–442, 2005.
- [25] F. Mücklich, A. Lasagni, and C. Daniel. Laser interference metallurgy - Using interference as a tool for micro/nano structuring. *International Journal of Materials Research (formerly Zeitschrift für Metallkunde)*, 97(10):1337–1344, 2006.
- [26] A. Lasagni, D. Acevedo, C. Barbero, and F. Mücklich. Direct patterning of polystyrene-polymethyl methacrylate copolymer by means of laser interference lithography using uv laser irradiation. *Polymer Engineering and Science*, 48(12):2367–2372, 2008.
- [27] A. Lasagni, P. Shao, J. L. Hendricks, C. M. Shaw, D. C. Martin, and S. Das. Direct fabrication of periodic patterns with hierarchical sub-wavelength structures on poly(3,4-ethylene dioxythiophene)-poly(styrene sulfonate) thin films using femtosecond laser interference patterning. *Applied Surface Science*, 256:1708–1713, 2010.
- [28] P.B. Clapham and M.C. Hutley. Reduction of lens reflexion by the moth eye principle. *Nature*, 244:281–282, 1973.
- [29] S. Weiner, W. Traub, and H.D. Wagner. Lamellar bone: structure-function relations. *Journal of structural biology*, 126:241–255, 1999.
- [30] S.J. Wilson and M.C. Hutley. The optical properties of moth eye antireflection surfaces. *Optica acta: International journal of optics*, 29(7):993–1009, 1982.
- [31] M. Antler. Tribology of metal coatings for electrical contacts. *Thin Solid Films*, 84:245–256, 1981.
- [32] E. Detemple, P. Leibenguth, C. Gachot, and F. Mücklich. Large-area patterned formation of intermetallic phases on Ti/Al multilayer systems by laser interference metallurgy. *Thin Solid Films*, 519(2):736–741, 2010.

- 
- [33] M. Duarte, A. Lasagni, R. Giovanelli, J. Narcisco, E. Louis, and F. Mücklich. Increasing lubricant lifetime by grooving periodical patterns using laser interference metallurgy. *Advanced Engineering Materials*, 10(6):554–558, 2008.
- [34] R. Catrin, D. Horwat, T. Gries, B. Raillard, J.F. Pierson, S. Migot, and F. Mücklich. Influence of laser interference patterning on microstructure and friction behaviour of gold/yttria-stabilized zirconia nanocomposite thin films. *Journal of Materials Research*, 27(6):879–885, 2012.
- [35] R. Catrin, T. Gries, D. Horwat, S. Migot, and F. Mücklich. Microstructure of sputter-deposited noble metal-incorporated oxide thin films patterned by means of laser interference. In Materials Research Society Symposium Proceedings, editor, *Plasma-Assisted Materials Processing and Synthesis*, volume 1339, pages mrss11–1339–s01–04, San Francisco, 2011. Materials Research Society.
- [36] R. Catrin, D. Horwat, J. F. Pierson, S. Migot, Y. Hu, and F. Mücklich. Nano-scale and surface precipitation of metallic particles in laser interference patterned noble metal-based thin films. *Applied Surface Science*, 257(12):5223–5229, 2011.
- [37] M. Hans, C. Gachot, R. Catrin, B. Raillard, and F. Mücklich. Laser interference structuring for the functionalization of copper materials [laser-interferenzstrukturierung zur funktionalisierung von kupferwerkstoffen]. *Metall*, 63(11):579–581, 2009.
- [38] R. Catrin, C. Gachot, G. Marchand, U. Schmid, and F. Mücklich. Selective wet chemical etching of metallic thin films designed by laser interference metallurgy (LIMET). In *Proceedings of SPIE*, volume 7362, pages 736217–1–6, 2009.
- [39] Mücklich F., Gachot C., Catrin R., Schmid U., and Lasagni A. Macroscopic 2D design of micro/nano grain architectures by laser interference metallurgy. volume 1059, pages 78–83, 2008.

- [40] J. Kovacik and F. Simancik. Aluminium foam modulus of elasticity and electrical conductivity according to percolation theory. *Scripta Materialia*, 39:239–246, 1998.
- [41] J.J. Hu, A.A Voevodin, and J.S. Zabinski. Application of in situ transmission electron microscopy for tribological investigations of magnetron sputter assisted pulsed laser deposition of yttria-stabilized zirconia - gold composite coatings. *Journal of Materials Research*, 20(07):1860–1868, 2005.
- [42] A.A Voevodin, J.J. Hu, J.G. Jones, T.A. Fitz, and J.S. Zabinski. Growth and structural characterization of yttria-stabilized zirconia-gold nanocomposite films with improved toughness. *Thin Solid Films*, 401(1-2):187–195, 2001.
- [43] A.A Voevodin, J.J. Hu, T.A. Fitz, and J.S. Zabinski. Tribological properties of adaptive nanocomposite coatings made of yttria stabilized zirconia and gold. *Surface and Coatings Technology*, 146-147(0):351–356, 2001.
- [44] W.T. Silfvast. *Fundamentals of photonics*. University of Central Florida, Orlando, Florida, 5-19-03 edition.
- [45] A. L. Schawlow and C. H. Townes. Infrared and optical masers. *Physical Review*, 112:1940–1949, 1958.
- [46] T. H. Maiman. Stimulated optical radiation in ruby. *Nature*, 187(4736):493–494, 1960.
- [47] A. Einstein. Zur Quantentheorie der Strahlung. *Physikalische Zeitschrift*, 18:121–128, 1917.
- [48] M. von Allmen and R. Blatter. *Laser beam interactions with materials: physical principles and applications*. Springer Series in Materials Science 2. Springer Verlag, Berlin, 2. edition, 1998.
- [49] W. M. Haynes. *CRC Handbook of chemistry and physics*. CRC press Taylor and Francis, 91. edition, 2011.

- 
- [50] R. B. Bergmann, J. Köhler, R. Dassow, C. Zaczek, and J. H. Werner. Nucleation and growth of crystalline silicon films on glass for solar cells. *Physica Status Solidi (a)*, 166(2):587–602, 1998.
- [51] S. Preston and G. W. Johnson. Effect of grain size and orientation on the initial permeability of 36 wt% Ni-Fe alloys. *Journal of Materials Science*, 19:4099–4105, 1984. 10.1007/BF00980777.
- [52] M. K. Kelly and B. Dahlheimer. Extended resolution for lateral structuring with laser interference gratings using high-index input coupling. *Physica Status Solidi (a)*, 156(2):k13–k16, 1996.
- [53] C. Eisele, C.E. Nebel, and M. Stutzmann. Laser crystallisation of silicon-germanium alloys. In *Polycrystalline and Semiconductors VI*, volume 80-81, pages 205–210, 2001.
- [54] A. Lasagni. *Advanced designs of periodical structures by laser interference metallurgy in the micro/nano scale on macroscopic areas*. PhD thesis, Saarland University, Saarbrücken, 2006.
- [55] A. Lasagni, C. Holzapfel, T. Weirich, and F. Mücklich. Laser interference metallurgy: a new method for periodic surface microstructure design on multilayered metallic thin films. *Applied Surface Science*, 253(19):8070–8074, 2007.
- [56] R. Jakubiak, T.J. Bunning, and R.A. Vaia. Multi-component active photonic structures via holographic photopolymerization. *SPIE Nanotechnology e-bulletin*, 1.1:3–4, 2004.
- [57] A. Lasagni, C. Holzapfel, and F. Mücklich. Periodic pattern formation of intermetallic phases with long range order by laser interference metallurgy. *Advanced Engineering Materials*, 7(6):487–492, 2005.
- [58] U. Schmid and H. Seidel. Effect of high temperature annealing on the electrical performance of titanium/platinum thin films. *Thin Solid Films*, 516(6):898–906, 2008.

- [59] U. Schmid and H. Seidel. Influence of thermal annealing on the resistivity of titanium/platinum thin films. *Journal of Vacuum Science and Technology A: Vacuum, Surfaces and Films*, 24(6):2139–2146, 2006.
- [60] P. Walker and W.H. Tarn. *Handbook of metal etchants*. CRC Press, New York, 1991.
- [61] K.R. Williams, K. Gupta, and M. Wasilik. Etch rates for micromachining processing - part ii. *Journal of microelectromechanical systems*, 12(6):761–778, 2003.
- [62] L.A. Giannuzzi, editor. *Introduction to focused ion beams: instrumentation, theory, techniques and practice*. Springer, New York, 2005.
- [63] W.C. Oliver and G.M. Pharr. Measurement of hardness and elastic modulus by instrumented indentation: advances in understanding and refinements to methodology. *Journal of Materials Research*, 19(1):3–20, 2004.
- [64] D. K. Schroder. *Semiconductor material and device characterization*. Wiley-Interscience, New York, 2. edition, 1998.
- [65] M. Dao, L. Lu, R.J. Asaro, J.T.M. De Hosson, and E. Ma. Toward a quantitative understanding of mechanical behavior of nanocrystalline metals. *Acta Materialia*, 55(12):4041–4065, 2007.
- [66] D. Son, J.H. Jeong, and D. Kwon. Film-thickness considerations in microcantilever-beam test in measuring mechanical properties of metal thin film. *Thin Solid Films*, 437(1-2):182–187, 2003.
- [67] T. Hanlon, A.H. Chokshi, M. Manoharan, and S. Suresh. Effects of grain refinement and strength on friction and damage evolution under repeated sliding contact in nanostructured metals. *International Journal of Fatigue*, 27(10-12):1159–1163, 2005.
- [68] R. Mishra, B. Basu, and R. Balasubramaniam. Effect of grain size on the tribological behavior of nanocrystalline nickel. *Materials Science and Engineering: A*, 373(1-2):370–373, 2004.

- 
- [69] S. Tao and D.Y. Li. Tribological, mechanical and electrochemical properties of nanocrystalline copper deposits produced by pulse electrodeposition. *Nanotechnology*, 17(1):65, 2006.
- [70] Z.B. Wang, N.R. Tao, S. Li, W. Wang, G. Liu, J. Lu, and K. Lu. Effect of surface nanocrystallization on friction and wear properties in low carbon steel. *Materials Science and Engineering: A*, 352:144–149, 2003.
- [71] M. Lee, S. Moon, M. Hatano, K. Suzuki, and C.P. Grigoropoulos. Relationship between fluence gradient and lateral grain growth in spatially controlled excimer laser crystallization of amorphous silicon films. *Journal of applied physics*, 88:4994–4999, 2000.
- [72] A. Lasagni and F. Mücklich. Fem simulation of periodical local heating caused by laser interference metallurgy. *Journal of Materials Processing Technology*, 209(1):202–209, 2009.
- [73] E. Saiz and A.P. Tomsia. Atomic dynamics and marangoni films during liquid-metal spreading. *Nature Materials*, 3:903–909, 2004.
- [74] P. Colinet, J.C. Legros, and M.G. Velarde. *Non-linear dynamics of surface-tension-driven instabilities*. WILEY-VCH, 1. edition, 2001.
- [75] S.J. Vanhook, M.F. Schatz, J.B. Swift, W.D. McCormick, and H.L. Swinney. Long-wavelength surface-tension-driven Bénard convection: Experiment and theory. *Journal of Fluid Mechanics*, 345:45–78, 1997.
- [76] M.G. Velarde and R.Kh. Zeytounian. *Interfacial phenomena and the Marangoni effect*. Springer, New York, 2002.
- [77] K. Petersen. Silicon as a mechanical material. In *Proceedings of the IEEE*, volume 70, pages 420–457, 1982.
- [78] S. Majoo, J.L. Gland, K.D. Wise, and J.W. Schwank. A silicon micromachined conductometric gas sensor with a maskless Pt sensing film deposited by selected-area CVD. *Sensors and actuators B*, 35-36:312–319, 1996.

- [79] J. F. Pierson, M. Baija, and D. Horwat. Silver islands formed after air annealing of amorphous AgCuMnO sputtered films. *Journal of Crystal Growth*, 311:349–354, 2009.
- [80] D. Horwat, J. L. Endrino, A. Boreave, R. Karoum, J. F. Pierson, S. Weber, A. Anders, and Ph. Vernoux. Deep oxidation of methane on particles derived from YSZ-supported Pd-Pt-(O) coatings synthesized by pulsed filtered cathodic arc. *Catalysis Communications*, 10:1410–1413, 2009.
- [81] M. Asano, K. Umeda, and A. Tasaki. Cu<sub>3</sub>N thin film for a new light recording media. *Japanese Journal of Applied Physics*, 29:1985–1986, 1990.
- [82] T. Maruyama and T. Morishita. Copper nitride and tin nitride thin films for write-once optical recording media. *Applied Physics Letters*, 69:890–891, 1996.
- [83] L. Maya. Covalent nitrides for maskless laser writing of microscopic metal lines. *Materials Research Society Symposium Proceedings*, 282:203–208, 1993.
- [84] T. Nosaka, Yoshitake M., Okamoto A., S. Ogawa, and Y. Nakayama. Thermal decomposition of copper nitride thin films and dots formation by electron beam writing. *Applied Surface Science*, 169-170:358–361, 2001.
- [85] J. F. Pierson. Structure and properties of copper nitride films formed by reactive magnetron sputtering. *Vacuum*, 66:59–64, 2002.
- [86] R. J. Farrauto, M. C. Hobson, T. Kennelly, and E. M. Waterman. Catalytic chemistry of supported palladium for combustion of methane. *Applied Catalysis A*, 81:227–237, 1992.
- [87] K. L. Saenger, C. Cabral, C. Lavoie, and Rossnagel S. M. Thermal stability and oxygen loss characteristics of Pt(o) films prepared by reactive sputtering. *Journal of Applied Physics*, 86:6084–6088, 1999.



- 
- [88] D. Horwat, D. I. Zakharov, J. L. Endrino, F. Soldera, A. Anders, S. Migot, R. Karoum, Ph. Vernoux, and J. F. Pierson. Chemistry, phase formation and catalytic activity of thin palladium-containing oxide films synthesized by plasma-assisted physical vapor deposition. *Surface and Coatings Technology*, 205:171–177, 2011.
- [89] G. Sirinakis, R. Siddique, I. Manning, P.H. Rogers, and M.A. Carpenter. Development and characterization of Au-YSZ surface plasmon resonance based sensing materials: high temperature detection of CO. *The Journal of Physical Chemistry B*, 110(27):13508–13511, 2006.
- [90] G.C. Bond. Gold: a relatively new catalyst. *Catalysis Today*, 72(1-2):5–9, 2002.
- [91] O. Knacke, O. Kubaschewski, and K. Heselmann. *Thermo-chemical properties of inorganic substances*. Springer-Verlag, Berlin, Germany, 2. edition, 1991.
- [92] S. Yuan, W. Huang, and X. Wang. Orientation effects of micro-grooves on sliding surfaces. *Tribology International*, 44(9):1047–1054, 2011.



# List of figures

1.1	Illustration of the composite effect in a single layer . . . . .	4
2.1	Description of the emission of a laser beam . . . . .	11
2.2	Stimulated emission, three and four levels pumping . . . . .	12
2.3	Absorption spectrum of some elements . . . . .	16
2.4	TEM views (bright-field) of single-pulse-irradiated Si films . .	18
2.5	Orientation-induced crystallized Si film . . . . .	19
2.6	Laser interference crystallization in a-Si . . . . .	20
2.7	Schematic representation of $\alpha_i$ and $\beta_i$ . . . . .	22
2.8	Two-beam laser interference assembly . . . . .	23
2.9	Three-beam laser interference assembly . . . . .	24
2.10	3D representation of three interfering sub-beams . . . . .	24
3.1	Laser path for two-beam interference patterning . . . . .	29
3.2	Laser path for three-beam interference patterning . . . . .	29
4.1	Laser-induced crystallisation in Ti/Pt thin films . . . . .	38
4.2	Low and high laser fluences in Ti/Au, Ti/Pt and Ti/W . . . .	40
4.3	Thermal simulation of irradiated Ti/Au, Ti/Pt and Ti/W . .	42
4.4	Grain-size distribution in Ti/Pt . . . . .	44
4.5	Texture analysis in Ti/Pt . . . . .	46
4.6	Nanoindentation tests on Ti/Pt and Ti/Cu . . . . .	47
5.1	Morphologies of laser-irradiated Ti/Pt and Ti/Au . . . . .	54
5.2	Effect of the wet chemical etching . . . . .	56
5.3	FIB cross section in Ti/Pt . . . . .	57

5.4	Morphology of Ti/Au after annealing in vacuum furnace . . . . .	58
6.1	Thermal evolution of Gibbs energy in Pd-Pt-O . . . . .	63
6.2	Morphological evolution of patterned $Cu_3N$ and $Pd_{0.25}Pt_{0.75}O_x$ . . . . .	64
6.3	Surface profiles of patterned $Cu_3N$ and $Pd_{0.25}Pt_{0.75}O_x$ . . . . .	66
6.4	X-Ray diffractograms of $Cu_3N$ and $Pd_{0.25}Pt_{0.75}O_x$ . . . . .	68
6.5	Microstructural investigations of $Pd_{0.25}Pt_{0.75}O_x$ . . . . .	70
7.1	Thermal evolution of Gibbs energy in Au-YSZ . . . . .	79
7.2	Morphology and microstructure of Au-YSZ . . . . .	81
7.3	Friction coefficient of Au-YSZ before and after patterning . . . . .	83
7.4	Wear track for 5 $\mu\text{m}$ and 15 $\mu\text{m}$ structure periods . . . . .	84
7.5	Abbott-Firestone curves . . . . .	85
7.6	In-depth profiles . . . . .	85

# List of tables

3.1	Samples and laser parameters used . . . . .	30
6.1	Chemical composition of patterned $Cu_3N$ . . . . .	71
6.2	Chemical composition of patterned $Pd_{0.25}Pt_{0.75}O_x$ . . . . .	72
6.3	Electrical resistivity in $Cu_3N$ and $Pd_{0.25}Pt_{0.75}O_x$ . . . . .	73



# Curriculum Vitae

# Rodolphe Catrin

Engineer in Materials Science - Laser Surface Engineering



28 years old  
French

[rodolphe.catrin@yahoo.fr](mailto:rodolphe.catrin@yahoo.fr)

## Education

**2008-2012** — PhD in Materials Science and Engineering. Saarland University, Chair of Functional Materials, Saarbrücken (Germany)

**2005-2008** — French-German double-degree in Materials Science and Engineering. Saarland University, Saarbrücken (Germany)

**2001-2007** — Bachelor and Master's degree in Materials Science and Engineering. École Européenne d'Ingénieurs en Génie des Matériaux (EEIGM), Nancy (France)

**1998-2001** — Baccalauréat Scientifique. Lycée Saint-Victor, Valence (France)

## Professional experience

**2012-2014** — Postdoc (**Eurotalents/Marie-Curie scholarship**), CEA CESTA, Le Barp (France)

**2008-2011** — Research engineer and PhD student in the field of laser surface engineering, specialized in laser surface functionalization of metallic films — Fully involved in the development of Erasmus Mundus Master and Doctorate Courses (AMASE and DocMASE) — Mentor for student of Master's Course (see [www.amase-master.net](http://www.amase-master.net)) and local coordinator of the EEIGM international study programme (see [www.eeigm.inpl-nancy.fr](http://www.eeigm.inpl-nancy.fr)). Saarland University, Saarbrücken (Germany)

**2005** — Internship at Astic Injection Industrielle. Crest (France)

**2004** — Internship at Schüco International. Bielefeld (Germany)

**2003** — Internship at Alpha Scientific Ltd. St-Albans (United-Kingdom)

## Teaching experience

Instructor in German language on **3D analysis by nanotomography** at the École Européenne d'Ingénieurs en Génie des Matériaux (Nancy, France)

## Languages

French / German / Italian: **trilingual**

English: fluent

Spanish: basic knowledge

## List of publications

[1] **R. Catrin**, D. Horwat, T. Gries, B. Raillard, J.F. Pierson, S. Migot, F. Mücklich, *Influence of laser interference patterning on microstructure and friction behavior of gold/yttria-stabilized zirconia nanocomposite thin films*. Journal of Materials Research 27 (2012) 879-885 - **Invited Feature Paper**

[2] **R. Catrin**, T. Gries, D. Horwat, S. Migot, F. Mücklich, *Microstructure of sputter-deposited noble metal- incorporated oxide thin films patterned by means of laser interference*. Mater. Res. Soc. Symp. Proc. Vol. 1339 (2011)  
doi: 10.1557/opl.2011.861

[3] **R. Catrin**, D. Horwat, J-F. Pierson, S. Migot, Y. Hun, F. Mücklich, *Nano-scale and surface precipitation of metallic particles in laser interference patterned noble metal oxide thin films*. Applied Surface Science 257 (2011) 5223-5229

[4] M. Hans, C. Gachot, **R. Catrin**, B. Raillard and F. Mücklich, *Laser interference structuring for the functionalization of copper materials*. Metall 63 (2009) 11 579-581

[5] **R. Catrin**, C. Gachot, G. Marchand, U. Schmid, F. Mücklich, *Selective Wet Chemical Etching of Metallic Thin Films Designed by Laser Interference Metallurgy (LIMET)*.



28 years old  
French  
[rodolphe.catrin@yahoo.fr](mailto:rodolphe.catrin@yahoo.fr)

Proc. of SPIE 7362 (2009) 736217

[6] C. Gachot, **R. Catrin**, A. Lasagni, U. Schmid, F. Mücklich, *Comparative Study of Grain Sizes and Orientation in Microstructured Au, Pt and W Thin Films designed by Laser Interference Metallurgy*. Applied Surface Science, 255 (2009) 5626-5632

[7] **R. Catrin**, A. Lasagni, C. Gachot, U. Schmid, F. Mücklich, *Microstructural Design of Advanced Architectures in Titanium/Platinum Thin Films by Laser Interference Metallurgy*. Advanced Engineering Materials 10 (2008) 5 466-470.

[8] F. Mücklich, C. Gachot, **R. Catrin**, U. Schmid, A. Lasagni, *Macroscopic 2D Design of Micro/Nano Grain Architectures by Laser Interference Metallurgy*. Mater. Res. Soc. Symp. Proc. Vol. 1059 (2008) KK04-06

### International conferences attended

- MRS Spring Meeting, 2011, San Francisco (USA): Oral presentation and poster
- e-MRS Spring Meeting, 2010, Strasbourg (France): **Invited speak**
- International Conference on Advanced Materials Research, 2009, Nancy (France): Poster
- SPIE Europe Microtechnologies for the New Millenium, 2009, Dresden (Germany): Poster
- MSE - Materials Science and Engineering, 2008, Nuremberg (Germany): Oral presentation
- e-MRS Spring Meeting, 2008, Strasbourg (France): Oral presentation

### Referee service

- Thin Solid Films
- Applied Surface Science
- Acta Biomaterialia
- Praktische Metallographie

### Scientific instruments operated

Nd:YAG pulsed laser, X-ray Diffraction, Scanning and Transmission Electron Microscopes, Focused Ion Beam (nanotomography), EBSD, EDX, SIMS, White Light Interferometer

### References available to contact

- **Prof. Frank Mücklich**, Saarland University, Chair of Functional Materials, Campus D3.3, D-66123 Saarbrücken (Germany). Email: [muecke@matsci.uni-sb.de](mailto:muecke@matsci.uni-sb.de), Tel.: +49 681 302 70500
- **Dr. David Horwat**, Institut Jean Lamour, UMR CNRS 71 98, École des Mines de Nancy, Parc de Saurupt, F-54042 Nancy (France). Email: [david.horwat@ijl.nancy-universite.fr](mailto:david.horwat@ijl.nancy-universite.fr), Tel.: +33 383 584 252
- **Dr. Andrés Lasagni**, Fraunhofer Institute for Material and Beam Technology (IWS), Dresden (Germany). Email: [andres-fabian.lasagni@iws.fraunhofer.de](mailto:andres-fabian.lasagni@iws.fraunhofer.de), Tel.: +49 351 833 913 0072